NASA TECHNICAL NOTE

NASA TN D-6062

NASA TN D-6062

FLIGHT RESULTS OF A 25 000-FOOT-PER-SECOND REENTRY EXPERIMENT USING MICROWAVE REFLECTOMETERS TO MEASURE PLASMA ELECTRON DENSITY AND STANDOFF DISTANCE

by William L. Grantham

Langley Research Center
Hampton, Va. 23365

NATIONAL AERONAUTICS AND SPACE ADMINISTRATION • WASHINGTON, D. C. • DECEMBER 1970

1. Report No. NASA TN D-6062	2. Government Accession No.	3

4. Title and Subtitle
FLIGHT RESULTS OF A 25 000-FOOT-PER-SECOND REENTRY EXPERIMENT USING MICROWAVE REFLECTOMETERS TO MEASURE PLASMA ELECTRON DENSITY AND STANDOFF DISTANCE

5. Report Date
December 1970

6. Performing Organization Code

7. Author(s)
William L. Grantham

8. Performing Organization Report No.
L-7107

9. Performing Organization Name and Address
NASA Langley Research Center
Hampton, Va. 23365

10. Work Unit No.
730-00-01-01

11. Contract or Grant No.

12. Sponsoring Agency Name and Address
National Aeronautics and Space Administration
Washington, D.C. 20546

13. Type of Report and Period Covered
Technical Note

14. Sponsoring Agency Code

15. Supplementary Notes

16. Abstract

Results of a reentry plasma diagnostic experiment made at a velocity of 25 000 ft/sec (7.62 km/sec) are compared with theoretical flow-field values at four locations on the spacecraft. Flow-field plasma properties were inferred from measurements obtained with a four-frequency microwave reflectometer having an electron density measurement range from approximately 10^{10} to 10^{13} electrons/cm^3. Good correlation exists between the reflectometer-determined plasma values and those obtained from electrostatic probes and other flight data taken during this experiment. Measured and computed plasma electron densities in the nose region generally agree except at low altitudes. In the aft flow-field region, a substantial electron density level difference is indicated at the higher altitudes, which is attributed to ambipolar diffusion mechanisms not included in the theoretical flow-field model. Plasma standoff distance measurements indicate strong electron density gradients near the vehicle surface, as expected from sheath calculations. At altitudes below about 100 000 ft (30.48 km), the interpretation of reflectometer data becomes more difficult because of the high electron-neutral collision frequency and the changes in antenna length caused by heat-shield ablation. Measurement errors in the aft flow field greater than a factor of 3 or 4, however, are unreasonable and in some instances there remains an unexplained factor-of-10 difference between measured and computed electron densities. Signal-strength data (VHF and X-band) and VSWR data from this flight (RAM C-II) and a previous flight (RAM C-I) are used to compare the effects of ablation products in the flow field. Unlike RAM C-II which had a relatively clean flow field because of its beryllium nose cap and high-purity teflon afterbody heat shield, RAM C-I had a nose cap with a high alkali-metal content which severely influenced the plasma electron density.

17. Key Words (Suggested by Author(s))
Reentry communications
Plasma diagnostics
Electrostatic (Langmuir) probes
Microwave reflectometer

18. Distribution Statement
Unclassified – Unlimited

19. Security Classif. (of this report)	20. Security Classif. (of this page)	21. No. of Pages	22. Price*
Unclassified	Unclassified	82	$3.00

*For sale by the Clearinghouse for Federal Scientific and Technical Information
Springfield, Virginia 22151

FLIGHT RESULTS OF A 25 000-FOOT-PER-SECOND REENTRY EXPERIMENT USING MICROWAVE REFLECTOMETERS TO MEASURE PLASMA ELECTRON DENSITY AND STANDOFF DISTANCE

By William L. Grantham
Langley Research Center

SUMMARY

Results of a reentry plasma diagnostic experiment made at a velocity of 25 000 ft/sec (7.62 km/sec) are compared with theoretical flow-field values at four locations on the spacecraft. Flow-field plasma properties were inferred from measurements obtained with a four-frequency microwave reflectometer having an electron density measurement range from approximately 10^{10} to 10^{13} electrons/cm^3. The reflectometer technique uses the sharp rise of reflection coefficient to indicate when the plasma approaches critical density. Good correlation exists between the reflectometer-determined plasma values and those obtained from electrostatic probes and other flight data taken during this experiment.

A simple spacecraft shape (hemisphere-cone) was used to minimize the difficulty of flow-field calculations. Also, to render the flow field free of influencing ablation products, a heat-sink beryllium nose cap was employed. The cap was pyrotechnically ejected at an altitude of 185 000 ft (56.39 km) as its temperature approached the melting point of beryllium; this ejection ended the primary data period (clean-flow-field period). For the remainder of the flight a teflon nose cap was used. Measured and computed plasma electron densities in the nose region generally agree in the primary data period; however, some deviation is noted above an altitude of 230 000 ft (70.10 km). In the aft region, a substantial electron density level difference is indicated at higher altitudes, which is attributed to ambipolar diffusion mechanisms not included in the theoretical flow-field model. Plasma standoff distance measurements indicate strong electron density gradients near the vehicle surface, as expected from sheath calculations.

At altitudes below about 100 000 ft (30.48 km), the interpretation of reflectometer data becomes more difficult because of the high electron-neutral collision frequency and the changes in antenna length caused by heat-shield ablation. The interpretation problems in the low-altitude region make the comparison of measured and computed electron density less meaningful. It is believed, however, that measurement errors in the aft flow

field greater than a factor of 3 or 4 are unreasonable and in some instances there remains an unexplained factor-of-10 difference between measured and computed electron densities.

Signal-strength data (VHF and X-band) and VSWR data from this flight (RAM C-II) and a previous flight (RAM C-I) are used to compare the effects of ablation products in the flow field. Unlike RAM C-II, which had a relatively clean flow field because of its beryllium nose cap and high-purity teflon heat shield, RAM C-I had a nose cap with a high alkali-metal content which severely influenced the plasma electron density.

INTRODUCTION

During hypervelocity entry into the earth's atmosphere, a spacecraft is enveloped by a plasma sheath which can cause RF signal blackout. Accurate definition of the plasma-sheath properties is therefore important for determining radio signal blackout boundaries and for designing efficient alleviation techniques.

Several in-flight plasma-sheath measurements have been made in order to upgrade the theoretical plasma model where necessary and improve the confidence level in the model. References 1 and 2 describe electron density measurements made at a velocity of 18 000 ft/sec (5.49 km/sec) which were compared with calculations. A favorable comparison was obtained for that entry velocity except at the higher altitudes (above 200 000 ft (60.96 km)) where theoretical values were a factor of 2 greater than measured electron densities.

Reference 3 describes ion density measurements[1] made with electrostatic probes at 25 000 ft/sec (7.62 km/sec), which indicated that at high altitudes the aft plasma layer was much thicker and had a lower ion density than was expected.

Calculation of aft plasma profiles requires not only a knowledge of the local chemical kinetics but of the entire gas history from the shock entry point of each streamline to the aft point of interest. This experiment was designed to improve knowledge of the flow field in both the nose and aft regions. Data are presented for the 25 000 ft/sec (7.62 km/sec) reentry experiment which had plasma sensors (microwave antennas) at four different locations along the spacecraft. These data are compared with calculations in an effort to assess the accuracy of the flow-field theoretical model.

The microwave reflectometer technique employed to diagnose the plasma uses the reflectivity of the plasma as an indication of the electron density level. The phase of the reflected wave was measured to infer the plasma critical density location in the nonhomogeneous plasma, and, thus, the general nature of the profile shape was indicated.

[1]Unpublished data were also obtained from the RAM C-II experiment by Linwood W. Jones, Jr., and Aubrey E. Cross of the Langley Research Center.

The use of a simple blunt-body shape (hemisphere-cone) and a nonablative nose cap for the spacecraft minimized the difficulty of theoretical calculations and provided a favorable environment for comparing measured and "clean air" computed values. Ejection of the nonablating beryllium nose cap at 185 000 ft (56.39 km) ended the primary data period (clean-flow-field period) and, for the remainder of the flight, an ablating teflon nose cap was used.

The data obtained below 185 000 ft (56.39 km) are of interest even though clean air assumptions are no longer valid. Also, at some point below this altitude, laminar-to-turbulent boundary-layer transition occurred which is likely to influence the plasma. Interpretation of the reflectometer data becomes less accurate at low altitudes due to high collision frequencies and recession of the microwave antennas.

This flight experiment is the second in the C series of project RAM and is designated RAM C-II. The primary experiment for the RAM C-I flight was injection of water into the flow field from the spacecraft as a means of alleviating communications blackout during reentry. Signal strength and VSWR data from the RAM C-I (ref. 3) and RAM C-II flights are used to show the effect of ablation products on electron density. The RAM C-I had a phenolic-carbon nose cone with a high alkali-metal content in contrast to the nonablating beryllium nose and high-purity teflon afterbody heat shield used in the present experiment.

SYMBOLS

D	nose diameter of payload
d	distance between antenna aperture and reflecting boundary, cm
Δd	incremental change in d between windward and leeward plasmas, cm
ΔdB	probe level relative to value when $\Gamma_p = 0$, dB
f	electromagnetic frequency, Hz
N_e	electron density, electrons/cm^3
t	teflon thickness change, cm
x	distance along spacecraft axis
y	normal distance from spacecraft, cm

Γ	reflection coefficient at aperture
$\Delta\theta$	incremental phase shift experienced between windward and leeward plasmas, deg
ϵ	dielectric constant
θ	phase shift of reflected wave, deg
λ	wavelength, cm
ν	electron-neutral collision frequency, collisions/sec
ρ	voltage reflection coefficient at probe unit
ϕ	angular coordinate for payload, deg
ω	electromagnetic frequency, rad/sec

Subscripts:

c	cut-off
cr	critical
d	distance
m	measured
n	probe number, n = 1 to 4
o	free space
p	power
pk	peak
r	reflecting boundary
sc	short circuit

DESCRIPTION OF VEHICLE AND PAYLOAD

Vehicle

A four-stage solid-propellant Scout vehicle (fig. 1) was used to place the payload on the desired reentry trajectory. The launch was made from the NASA Wallops Station with reentry occurring near Bermuda (fig. 2) where tracking and telemetry stations were located.

During the ascending phase of the flight, a heat shield (fig. 1) protected the payload from aerodynamic heating. This heat shield was jettisoned at 724 000 ft (220.68 km). The first two stages of the Scout were used to achieve an apogee of about 747 000 ft (227.69 km). Just before apogee the vehicle was oriented to -15° entry angle and the third stage was ignited; thus, the payload was driven back into the earth's atmosphere at a velocity of 24 900 ft/sec (7.59 km/sec) at fourth-stage burnout. Further acceleration of the payload due to gravity raised the velocity to a maximum of 25 190 ft/sec (7.68 km/sec).

Payload spin-up was initiated just prior to fourth-stage ignition to maintain small angles of attack during fourth-stage thrusting and the reentry period. This spin also allowed the electron density sensors to alternately monitor windward and leeward plasma conditions about every 166 msec. Retromotors separated the fourth stage from the payload at an altitude of about 350 000 ft (106.68 km).

Payload

The payload had a 6-in-radius (15.24 cm) hemispherical nose with a 9° half-angle conical afterbody (fig. 3). A heat-sink beryllium nose cap was used during the early portion of the reentry period to maintain the flow field free of ablation products. Since the nose-cap temperature was expected to approach the melting point of beryllium at low altitudes, the cap was ejected pyrotechnically at 185 000 ft (56.39 km), which exposed a teflon hemispherical nose $\left(1\frac{1}{2}\right.$ in. (3.81 cm) thick and 6.325-in. (16.065 cm) radius$\left.\right)$. A photograph of the flight backup payload in this configuration is shown in figure 4. The payload conical section had a 0.3-in-thick (0.762 cm) teflon heat shield.

Special attention was given to minimizing the alkali-metal content in the teflon ablator material. Raw-material selection and heat-shield fabrication were controlled to keep the easily ionizable material out of the teflon and thus out of the flow field during reentry. A neutron activation technique was used to measure the quantities of Na, K, Rb, and Cs in the teflon, and the heat shield was found to have less than 5 parts per million (ppm) total alkali-metal content.

Two major instrumentation systems were used in the payload: one system included the reflectometer and electrostatic probe experimental apparatus; the other, the telemetry system and associated body motion and heat sensors. The general layout of the spacecraft equipment is shown in figure 5. A description of the reflectometer and other instrumentation pertinent to the plasma definition is given in the discussion that follows.

Reflectometer system.- Four frequencies were used in the reflectometer system in the L-, S-, X-, and K_a-bands. The exact frequency used in each band is given in table I. Details concerning the RF components and antenna design are given in the following sections.

Components: Components of each of the reflectometer systems used in the flight experiment consisted of a microwave signal source, an isolator, a four-way power divider (three way for L-band) to split the signal so that several antennas could be employed for the same frequency, bidirectional couplers on each of the four lines to measure transmitted and reflected power levels, four electric field probe units spaced at about $\frac{1}{8}$-wavelength intervals on each line to measure the phase and magnitude of the wave reflected (ref. 4, pp. 303-307) by the plasma, and antennas to launch the electromagnetic wave into the plasma. The K_a-band had only two probes each at stations 2, 3, and 4. A dc-to-dc converter was used to drive the microwave tubes from a 28-volt battery supply.

A typical block diagram of a reflectometer (S-band) is given in figure 6. The individual components for the four frequencies used are shown in figure 7. Only one antenna (station 3 type) and probe unit is shown for each frequency.

All RF components were interconnected by 0.141-in. (0.358 cm) semirigid coaxial cable for L-, S-, and X-bands. Flexible waveguide was used for K_a-band. Strip transmission line components were used for the three lower frequencies, and rigid waveguide was used for K_a-band. Typical electrical properties of the components are shown in table II. The VSWR of the individual and combined components was kept low to minimize measurement errors in phase and reflection coefficients, and insertion losses were kept to a minimum to give maximum diode outputs.

Antenna design: Reflectometer antennas were located at four stations along the spacecraft (fig. 5 and table III) so that a detailed study of the fore and aft plasma regions could be made. At station 1 ($x/D = 0.15$), circular waveguides (TE_{11} mode) were extended through the teflon nose by using thin (1 to 10 μm thick) metallic sleeves as waveguide walls to feed the quartz-filled circular antennas in the beryllium cap. All four stations had an antenna for each of the four frequencies except station 1, which did not have an L-band antenna due to lack of space. This gave a total of 15 reflectometer antennas on the C-II payload. Stub tuners were used to eliminate VSWR's introduced by the dielectric plugs and aperture mismatch.

The antenna design was controlled primarily by the anticipated plasma environment, namely, the distance between the antenna and the critical density boundary. In the nose region, the plasma was expected to be very close to the spacecraft and open-end waveguides were used. In the aft flow-field region, however, it was expected that the plasma reflecting layer would be farther from the spacecraft. Since small (low gain) open-end waveguides generally have low return signals when a reflector is more than 1 wavelength away, high-gain horn antennas were used at the aft stations for the two upper frequencies (X- and K_a-bands). Open-end waveguides were satisfactory for the L- and S-bands due to their long wavelengths.

Table IV gives the characteristics of the various types of reflectometer antennas used and figure 8 shows the reflection signatures of the station 3 antennas. The signatures were obtained by measuring reflected signal level as a function of distance to a metal plate having curled edges which simulates an overdense plasma with an air gap. The edges were curled to minimize diffraction effects (ref. 5). These reflection signatures were used in a preflight evaluation of the antenna's ability to detect a distant reflecting boundary. References 6 and 7 discuss the general characteristics of this type of signature, and ways of making the signal decrease monotonically with distance are discussed in reference 8. The conical-horn flight antenna design (X- and K_a-bands) used small flare angles and long axial lengths to minimize the reflected signal oscillations. Phase path differences were designed to be $\lambda_o/16$ across the aperture for both conical horns (ref. 9). Drawings of the station 3 antennas are shown in figure 9.

To further improve plasma-reflected signal levels, the S-, X-, and K_a-band aft antennas were brought closer to the plasma by extending their conducting surfaces through the teflon heat shield with 1- to 10-μm vapor-deposited metallic sleeves. This design is shown in figures 9(b) to (d). The thin wall was designed to recede with the teflon as it ablated. The metallic sleeves also reduced microwave energy loss in the teflon layer caused by surface wave excitation. Presence of surface waves would generally complicate interpretation of the data, as is shown in some of the flight data obtained with the X-band telemetry horn which did not have the metal-sleeve extensions.

Teflon thickness changes due to ablation did not begin to affect the measured reflection coefficients until after the primary data period which ended at an altitude of 185 000 ft (56.39 km). Below that altitude, teflon recession affects reflectometer measurements in two ways: First, by changing the short-circuit-phase reference value due to the shortened antenna length and, second, by introducing a small VSWR caused by the change in antenna plug thickness.

The amount of ablation at different antenna locations (fig. 10) was computed for the flight trajectory. Corresponding phase errors for each frequency are also shown except for L-band which was less than 10^o. Note that phase errors are small (less than 5^o) at

altitudes above 185 000 ft (56.39 km). The phase-error calculations were made for teflon plugged waveguide antennas at station 1.

Other instrumentation used in plasma definition.- A number of other data obtained during the flight have been correlated with the reflectometer measurements. They include electrostatic probe data, X-band telemetry-antenna VSWR, and VHF and X-band signal-strength levels received at several ground stations during reentry. All these data are used to infer aft body flow-field conditions. Ablation effects are also noted by comparing some of these data with measurements made on the earlier C-I flight. The related instrumentation is described briefly herein and in detail in reference 3.

Electrostatic probes: Positive ion density profiles have been determined by using data from a rake of eight negatively biased electrostatic probes at $x/D = 4.05$ (figs. 3, 5, and table III). A finlike sting supported the ion-collecting probes (fig. 11) and, on the opposite side of the payload, a similar fin with thermocouples was used. The thermocouples gave aerodynamic heating data needed for computing the insulation properties of the beryllium oxide. Knowledge of probe insulation properties was needed in the interpretation of the probe data.

Instrumentation used to make the probe measurements and the theory used to interpret the data are given in reference 3. In the present report, probe data are compared with reflectometer data taken at station 4.

Signal-strength measurements and X-band telemetry-antenna VSWR: Signal-strength data were obtained at several receiving stations (table V and fig. 2) during the data period at VHF, C-, and X-band frequencies. The C-band beacon and radar cross-section measurements are given in reference 10. These data permit an assessment of plasma effects on antenna patterns as well as give the blackout times.

This report is concerned with two aspects of the signal-strength data: First, how plasma data inferred from the X-band blackout times compare with X-band telemetry VSWR and reflectometer data and, second, how the blackout times of this flight experiment compare with those of RAM C-I which had an ablating nose cone with a high alkali-metal content. Location of the various antennas are shown in table VI for RAM C-I and tables I and III for RAM C-II.

The X-band telemetry horn VSWR also provides comparative diagnostic data for the two flight experiments to show the effect of ablation products on electron density. For RAM C-II, it gives some rectangular horn data for direct comparison with the reflectometer conical horn VSWR data (station 3). The 8.5-dB-gain rectangular horn is covered by the teflon heat shield without metallic sleeves extending through the dielectric. As a result, it has a reflection signature which is significantly different from that of the conical horn.

The preflight measured properties of the two horns are compared in figure 12. Reflection levels are shown relative to a short-circuited aperture. The reflectometer conical horn was designed to avoid strong oscillations in the signature so that it could detect the reflecting plasma layer several wavelengths from the spacecraft. However, the primary design consideration for the rectangular telemetry horn was its transmission characteristics (ref. 3). The presence of a good conducting surface in front of the rectangular horn might be undetected if it is located at any one of the nulls in the signature. The plasma-reflecting boundary is believed to have been positioned at one of the nulls, as will be shown in the flight results section.

Telemetry system.- Flight data were transmitted on three down links. Two of these (259.7 MHz and 9210.0 MHz) telemetered real-time data and the third (225.7 MHz) transmitted the same data 45.16 sec later by using a continuous-loop tape-recorder playback system. Payload data taken during the 30-sec blackout period were thus transmitted on the delayed playback down link after emergence from blackout and before splash down.

Two commutators were used to process the reflectometer data and provided a fast sampling rate to show spin effects on the data. Formats used for the data processing are shown in figure 13. Forward power and reverse power were sampled once every 50 msec, which gave about seven reflection-coefficient data points per payload revolution. This sampling was done by using a 45×20 commutator (45 switch positions each sampled 20 times per sec). All reflection-coefficient data presented were taken from this commutator except the K_a-band data (decommutation problems).

The 90×10 encoder was used to sample all the reflectometer data outputs at 100-msec intervals to give about three data points per payload revolution from each diode output. Phase coefficients presented were reduced from the probe data on the 90×10 commutator.

REFLECTOMETER TECHNIQUE

Reflection and Phase-Coefficient Measurements

Reflection coefficients were obtained by using the bidirectional coupler diode outputs (fig. 6) and phase coefficients were derived from diode outputs from the electric-field probes. Diodes in these components were calibrated as shown in figure 14 and voltage divide networks were used in the flight payload to adjust the diode outputs to about 40 mV for telemetry purposes. Temperatures were monitored on each component having diodes in it so that calibration adjustments could be made if necessary. No adjustments were needed however since the temperature changes during flight were less than 3° F (257° K).

Preflight reference levels were obtained by shorting the antennas with a reflecting foil. The level of coupler output compared with the preflight levels (fig. 14) expressed in decibels ΔdB is used to compute the power reflection coefficient Γ_p from $\Gamma_p = 10^{-\Delta dB/10}$. Corrections were made for any changes in forward power between the preflight level and the level at the time of interest. These corrections were generally less than 0.1 dB.

Measurement errors in reflection-coefficient magnitude for the bidirectional coupler are shown in figure 15 as applied to the S-band reflected power output. Typical individual error sources are identified and summed. The incremental error in Γ_p is shown (fig. 15(b)) since this error controls electron-density-measurement accuracy, as is discussed subsequently in this report.

The four electric-field probes (fig. 6) measure signal level along the standing wave envelope in the transmission line. The detected probe outputs are related to both reflection and phase coefficients according to the following equation derivable from the standing wave equation given in reference 11:

$$p_n = 10 \log\left[(1 - \rho)^2 + 4\rho \cos^2(\theta_n)\right] \tag{1}$$

where

p_n level of probe n relative to value when $\rho = 0$, dB

ρ voltage reflection coefficient at probe unit

θ_n phase at probe n

The probe data were reduced two ways. The first method used a line-loss-adjusted reflection-coefficient value from the bicouplers to compute the phase from equation (1) for each individual probe. The second and more accurate method employed the four-probe data collectively in a curve-fitting program which gave a best fit of the data to equation (1) by using a least-squares technique. The four-probe method not only gives a more accurate phase value but it gives a redundant measurement of the reflection magnitude. In some cases, identified on the data figures, less than four probes were available for computing phase.

Phase measurement errors for the four-probe technique have been determined by using the error sources identified in figure 16. These probe level errors were applied to the four probes in the worst possible combination to give the maximum error from the least-squares curve-fit program (fig. 16(b)).

Electron Density Determination

Microwave reflection coefficient has been used for some time to indicate plasma electron density (refs. 12 and 13). Lin, Neal, and Fyfe (ref. 14) used the coefficient to make measurements over a two-decade range. The technique described in the present paper differs in that it uses the sharp rise of reflection coefficient (hereinafter called the slope technique) to indicate when the peak plasma electron density approaches the critical value $\left(N_{e,cr} = 1.287 \times 10^{-8} f^2\right)$ in the dynamically changing reentry plasma. A three-decade measurement range $\left(\approx 10^{10} \text{ to } \approx 10^{13}\right)$ was obtained by using four different microwave frequencies. Figure 17 shows this measurement principle applied to the station 2 reflectometer data. A reflection coefficient of 0.2 is used to indicate an electron density ratio $N_{e,pk}/N_{e,cr}$ of 0.63, as is discussed subsequently in the report. By fairing between the data points, an estimate can be made of the ionization history throughout the reentry period for each station on the payload. Data indicated by the open symbols at the low altitudes are subject to error due to high collision frequencies and antenna-length changes caused by ablation. By using the slope technique, electron density measurement accuracy is less dependent on the absolute magnitude of the reflection coefficient. A low value of the normalized collision frequency ($\nu/\omega < 1$) is required to have a sharp increase of reflection near critical density. This requirement is satisfied during the primary data period (down to 185 000 ft (56.39 km)). At lower altitudes, collision frequency effects tend to decrease the sharpness with a resulting decrease in the accuracy of the measurement.

The reflectometer technique is clearly dependent on the sharp rise of reflection near critical density, which is predicted by plane wave theory (ref. 15) and by recent theoretical formulations that more correctly determine impedance values for plasma-clad antennas (refs. 16 and 17). Experimentally, this sharp rise has been observed under a variety of aperture-plasma conditions (refs. 17 and 18) including two of the three flight antenna designs used in this experiment (ref. 19), namely, an open-end circular guide and a conical horn. The L-band rectangular aperture design was not tested. Before reviewing these ground test results and comparing them with theoretical values for the circular aperture, similarities of the theoretical and flight antennas are examined. Attention is directed primarily toward the circular aperture antennas since 12 out of the 15 reflectometer antennas have that geometry.

There are three main differences between the circular aperture flight antennas and the circular aperture theoretical model (refs. 16 and 20). They are as follows:

(1) The experimental ground planes were finite and curved instead of infinite and flat. Reference 20 shows that apertures on finite ground planes 2 wavelengths square give essentially infinite ground plane impedance values. The ground planes used included both metallic types such as station 1 before the beryllium cap was ejected and

teflon-coated metal ground planes. For all teflon-covered antennas except L-band, the waveguides and horns were brought through the teflon by using thin metallic sleeves (fig. 9).

(2) The flight circular apertures were, in some instances, fed with conical horns (table IV) instead of TE_{11} mode circular waveguides. Finite-length circular waveguides fed the apertures rather than infinite-length waveguides as assumed in the model; this placed the coaxial-to-waveguide transition near the aperture with a possibility of generating higher order modes at the aperture. References 20 and 21 show that the presence of higher order modes in a large aperture contributes very little to the aperture impedance.

(3) The free-space reflection coefficient of each flight antenna was reduced to about 0.004 (typical) by using tuning screws in the waveguide section adjacent to the antenna. For the L-band, coaxial stubs were used. The mismatch effects of the dielectric plugs in the antennas were also removed by this tuning. Due to their large size, the X- and K_a-band conical-horn-fed apertures had small free-space reflection levels which coincided with levels from the theoretical model, but the open-end-waveguide antennas were designed near cut-off and their free-space reflection level was about 0.1.

Although the flight antennas are different in some respects from those having theoretical solution, the shock-tube experimental results in reference 19 show that the differences do not alter the sharp rise of the reflection level near critical density (figs. 18 and 19). A comparison is shown in figure 18 between the X-band conical-horn data and theoretical values for a plasma-covered circular aperture. It is seen that electron densities derived from the mean reflection-coefficient curve fall within about 50 percent of those derived from the theoretical curve for reflection levels below 0.5. Possible reasons for the deviations above $\Gamma_p = 0.5$ are discussed in reference 19. Also, the slopes of the individual curves coincide with the theoretical slope except for a systematic lateral displacement along the electron density axis. The lateral displacement between individual runs is attributed to errors in shock-tube electron density values derived from the Langmuir probes. Comparable plane-wave theoretical values (ref. 22) are also shown for the same nonhomogeneous profile for reference purposes. The close agreement between the theoretical and experimental reflection-coefficient values shows the applicability of the circular aperture theoretical model to that particular antenna design. The effect of high collision frequencies for the X-band aperture is shown in figure 20. The two lower collision frequencies $\left(2.51 \times 10^9 \text{ sec}^{-1} \text{ and } 2.51 \times 10^{10} \text{ sec}^{-1}\right)$ are typical for altitudes of 150 000 and 100 000 ft (45.72 and 30.48 km), respectively, for stations 2, 3, and 4. The third collision frequency shown $\left(2.51 \times 10^{11} \text{ sec}^{-1}\right)$ is typical for station 1 at 100 000 ft (30.48 km).

A similar comparison between the S-band shock-tube data and circular aperture theoretical values is not made since the free-space reflection of this antenna was tuned out. The theoretical model does not account for tuning. Some insight relevant to the reflectometer antennas can be derived by using geometrical theory of diffraction (refs. 23 and 5) where the total reflection coefficient of an aperture is treated as the vector sum of the free-space reflection and the external (plasma) reflection. When the free-space reflection is tuned to a low value, as the flight antennas were, the measured reflection level approaches the reflection value of the external medium. Higher order reflections between the tuner and external medium are assumed to be small compared with the first-order terms which should be valid for the RAM antennas. Reference 23 shows that this external reflection can be approximated by using plane waves and for the general case is accurately described from cylindrical wave theory with appropriate restrictions. For example, the external medium must be more than a half wavelength from the aperture.

In figure 19, plane-wave theoretical values are seen to agree well with the S-band shock-tube reflection data near critical density. The behavior of the phase coefficient discussed in the next section is also shown to coincide with plane wave concepts for small tuned apertures even when the spacing between the aperture and external medium is less than a half wavelength. A thorough discussion of the quasi-optical approach to aperture antennas is given in reference 24.

Interpretation of the flight data is made by using a reflection-coefficient value of 0.2 to indicate when the density ratio $N_{e,pk}/N_{e,cr}$ is 0.63 (from the mean of the experimental curves in fig. 18). A factor-of-2 error bar is applied to the ratio due to variations in shock-tube electron densities (ref. 19). The choice of the 0.2 reflection value was made by projecting reflection-coefficient measurement errors (fig. 15(b)) onto the mean curve of figure 18(a) and selecting the value giving minimum electron density error. A similar analysis made on the S-band open-end-waveguide data gives essentially the same electron density value (within 10 percent).

The reflectometer antennas were studied in a particular plasma environment (ref. 19), one with an essentially homogeneous profile. However, the effect of having other profile shapes in the flight should not appreciably influence the initial response of the reflectometer as the peak density goes through critical density; the absolute level at higher densities may be affected. This absence of sensitivity to profile shape is shown both experimentally and theoretically in references 17 and 25 for a rectangular aperture. Reference 16 presents similar theoretical arguments for circular aperture antennas.

Included in reference 16 are calculations for thick homogeneous, hyperbolic, and parabolic profiles as well as thin parabolic shapes. Collision-frequency effects are also examined up to ν/ω values of 0.4. Any errors introduced by profile or collision-frequency effects in relating reflection-coefficient magnitude to electron density are

expected to be within the factor-of-2 error bar already applied to the data for the primary data period. A more definitive error analysis must await tests on the flight antenna designs with a better laboratory plasma or a theoretical model that more exactly matches the flight antenna geometry.

Plasma-Standoff-Distance Determination

In addition to determining electron density from reflectometer data, the phase measurements can be used to infer the nature of the plasma profile shape. Specifically, normal distance from the vehicle surface to the critical density boundary can be determined if the plasma is overdense $\left(\frac{N_{e,pk}}{N_{e,cr}} \geqq 10\right)$ and if the reflection coefficient is large enough to permit an accurate phase measurement. Plane wave concepts are used to develop a simple approximate model for interpreting the phase in terms of this plasma parameter which provides physical insight for interpreting the flight data. This simple model is shown to be a reasonable approximation to the more sophisticated circular aperture theoretical model.

The behavior of an electromagnetic wave transmitted from the spacecraft into the reentry plasma is somewhat analogous to that which occurs in ionospheric sounding experiment – namely, the wave propagates into the plasma until it encounters an impedance change in the region of the critical density layer whereupon it reflects. In the reentry experiment, standing waves are set up in the microwave transmission line by the reflection and electric-field magnitudes are sampled along the standing wave envelope by the electric-field probes for use in computing phase coefficient of the reflected wave θ_n.

From a plane wave approach, the phase coefficient can be considered to be the sum of two phases $(\theta_n = \theta_d + \theta_r)$: θ_d, the phase shift experienced by the wave in propagating from the antenna to the reflecting boundary and back $\left(\theta_d = \frac{360(2d)}{\lambda_o} \text{ deg}\right)$, and θ_r, the phase shift at the reflecting boundary. Solving for the reflector distance gives

$$d = (\theta_n - \theta_r)\frac{\lambda_o}{720}$$

It can be seen that d and θ_n are linearly related. Phase measurements made on the X-band flight-type conical horn and S-band open-end-waveguide antenna verify this linear dependence for a metal-sheet reflector which simulates an overdense plasma. Teflon slab reflectors $(\Gamma_p < 1.0)$ also show that the linear dependence is not controlled by the reflection-coefficient value (fig. 21). Another important feature shown by figure 21 is that the measured phase deviates from the normal pattern when the external reflection level is near or below the system residual reflection level (region A).

Computations for a parallel-plate waveguide illuminating a conducting sheet (ref. 26) and a plasma-covered circular aperture antenna (fig. 22(a)) also show a linear relationship between phase and standoff distance. It should be noted from reference 26 that when the reflection due to the external medium is comparable to the antenna free-space reflection, this linearity is destroyed. Figure 22(a) gives the circular aperture phase coefficients for three profiles (fig. 22(b)) typical of those encountered during flight and indicates the sensitivity of phase to critical density standoff distance. For zero air gap, the phase values for the homogeneous plasma, profile 1, and profile 2 are 154°, 102°, and -5°, respectively. Converting these phases to standoff distance (relative to the homogeneous value) by using the plane wave model gives 0.22 cm and 0.66 cm which compares well with the values of 0.2 and 0.8 cm taken directly from the profile plots. Although the standoff distance error is small, it should be pointed out that the 0.14-cm error for profile 2 amounts to about a 33° error in phase.

For the plasma, θ_r is primarily a function of N_e and asymptotically approaches 180° for $\frac{N_{e,pk}}{N_{e,cr}} \geqq 10$ (ref. 27) and, for that overdense condition, can be set at 180°. The overdense condition exists for a given frequency during the flight if the next higher frequency is being reflected, since any two adjacent critical densities are different by about a factor of 10.

Interpretation of the flight phase measurements is made in terms of normal critical density standoff distances by using

$$d = \theta_m \frac{\lambda_o}{720}$$

where the measured phases θ_m are relative to the preflight phase values determined for the short-circuited antenna $\left(\theta_{r,sc} = 180^{\circ}\right)$. Calculations based on an overall error of 20° in the measured phase (fig. 16, $\Gamma_p \geqq 0.10$) or in θ_r indicate that the following distance errors are incurred:

Frequency band	Error in d, cm
L	0.68
S	.24
X	.08
K_a	.02

The requirement that $N_{e,pk} \geqq 10N_{e,cr}$ may be removed if one wishes to examine incremental changes in distance experienced as the antennas measure the windward and leeward plasma properties. For this condition, the movement of critical density boundary is given by

$$\Delta d = \frac{\Delta\theta_m \lambda_o}{720}$$

and θ_r need not be known. It is important, however, that the windward-to-leeward electron density ratio not be large enough to change the θ_r value. Analysis of the data from this point of view is not presented in the present report.

THEORETICAL DESCRIPTION OF REENTRY PLASMA

Plasma calculations have been made for the hemisphere-cone spacecraft geometry with and without the beryllium cap. The flow field was assumed to be free of contaminants. This clean air assumption should be valid down to 185 000 ft (56.39 km) where the cap was ejected. The beryllium cap kept ablation products out of the nose region where most of the electron production occurs; the teflon afterbody did ablate some, even at high altitudes. To minimize the effect of the teflon ablation products, easily ionizable metals were kept below 5 ppm in the teflon heat shield. It is shown that although teflon ablation products may have been present at high altitudes, they did not affect electron density in a measurable way.

Plasma electron densities have been computed for three different flow-field models. Given below are the salient features of each model and references where details may be found. Models I and II use finite rate chemistry; model III gives equilibrium (infinite rate) values for comparison.

In model I (ref. 28), a streamline method is applied by using a reasonably complete reaction system with finite rate chemistry. Also, special attention was given to merging the boundary layer and inviscid layer at the high altitudes and, as a result, these calculations are believed to be the most accurate. Trajectory conditions used for the computations are given in table VII. The 1962 standard atmosphere midlatitude mean (ref. 29) was assumed for ambient gas conditions. Meteorological rocket measurements (ref. 30) given in figure 23 were made on the day of launch (Aug. 22, 1968) at Bermuda and agree closely with values given in reference 31 for latitude 30° N., July. The differences between the 1962 and 1966 standard atmospheric conditions (refs. 29 and 31) are not large enough to warrant recalculation of the plasma conditions.

In model II (ref. 32), finite rate chemistry was also used, but several charge exchange reactions were not included which do influence computed N_e values in the 150 000-ft (45.72 km) altitude region (ref. 28). The calculations include values of electron density, neutral and ionic species concentration, temperature, pressure, and velocity, and are given in reference 32. The computations made at 12 body normals were repeated at two low-altitude points on the trajectory for the payload geometry with the beryllium cap off. The conditions used for the computations are given in table VIII.

The equilibrium flow-field (model III) properties were determined in an intermediate step of the model II calculations for the first four body normals and are given in reference 32. These calculations were to serve as a reference point for determining the degree of nonequilibrium in the flow. A comparison of equilibrium and nonequilibrium values (model II) is given in reference 32.

FLIGHT DATA AND DISCUSSION

All payload systems operated satisfactorily during the reentry experiment. Telemetry signals were reacquired as the payload emerged from radio blackout and the reentry heat pulse. The X-band telemetry reacquisition was delayed due to tracking difficulties caused by its narrow beam receiving antenna. The flight trajectory determined from Bermuda radar and payload instrumentation is presented in figures 24 and 25 and in table IX. Continuous tracking of the payload was achieved from radar horizon through apogee down to 185 000 ft (56.39 km). Apparently, the radar tracked the ejected beryllium cap below that altitude. Computation of the trajectory below that altitude was determined from payload instrumentation data.

Payload accelerometer data indicated that angle of attack was less than 6° during the reentry period (fig. 26). Because of low accelerometer levels at the high altitudes, absolute values for angle of attack are less accurate. Relative change, however, should be correct.

Microwave reflection- and phase-coefficient data taken from the commutated telemetry channels are shown in figures 27 and 28, respectively, for the reentry data period. All reflection coefficients were obtained from the 45×20 commutated bidirectional coupler data except where noted otherwise; similar data were obtained from the four electric-field probes. In addition to reflection-coefficient plots, oscillographic records of the diode outputs for each reflected power channel are given in figure 29. Enlarged working copies of this figure are included in a folder at the back of the report. These enlarged records show better details of the signal modulation caused by windward and leeward plasma changes. Only station 1 has K_a-band data because of decommutation problems. The forward power levels were essentially constant during the entire flight.

Phase coefficients were obtained from the commutated (90×10) probe-unit voltages by using the curve-fit program discussed previously. All phase and magnitude values presented are relative to preflight levels measured when aluminum foil (to produce a short circuit) was placed over each antenna except as noted in figure 27(a). The foil was assumed to have a reflection coefficient of 1.0 and a phase coefficient of 180°.

Reflection Coefficients

The reflection-coefficient data for the most forward body location (x/D = 0.15) have several features that are important to note. Ejection of the beryllium cap is clearly indicated by the K_a-band reflection change at 185 000 ft (56.39 km). (See fig. 27(a).) This was the only antenna badly mismatched when the cap was removed. Because of the mismatch and antenna losses, the reference level at K_a-band was used as noted. Before lift-off, each antenna at station 1 was matched to free space with the beryllium cap on. No mismatch effects due to cap removal are noticeable for the S-band and X-band which have already experienced plasma reflection at about 277 000 ft and 264 000 ft (84.43 km and 80.47 km), respectively. A sharp change was observed for the phase coefficients (fig. 28(a)) as a result of the change in electrical length of the antenna when the cap was ejected.

The K_a-band sensor at station 1 did detect critical density at about 236 000 ft (71.93 km) but, because the plasma was offset from the vehicle surface, the reflection coefficient was low and the coupler was unable to detect the weak signal. Therefore, the more sensitive probe levels were used to indicate the presence of critical density. Very slight variations of reflecting boundary distance in the windward and leeward plasmas caused the phase to change and, thus, the standing wave was shifted back and forth across the stationary probe. The resulting probe level modulation (approx. 1 dB) was used to indicate when the plasma became reflecting.

At very low altitudes (below about 100 000 ft (30.48 km)) the reflection coefficients dropped off. Thickness changes in the teflon ablation cover caused the reflection level to oscillate from a maximum to minimum for every quarter wavelength change in teflon thickness. More oscillations are seen on the K_a-band record since it has the shortest wavelength. The heavy ablation period is identified on the abscissa. Teflon recession estimates (0.6 in. (1.52 cm)) made from the K_a-band post plasma-reflected signal oscillations agree closely with the 0.48-in. (1.22 cm) value derived from a capacitative-type ablation sensor used at station 1.

At station 2, just aft of the tangency point, the reflection data (fig. 27(b)) indicate similar characteristics to those at station 1. L-band data are included for station 2. It is of interest that, after onset of plasma reflection, the S- and X-band data show rapid oscillations in the 125 000-ft (38.10 km) altitude region where angle of attack was large. This type of modulation has been observed on other spinning reentry payloads (ref. 33) and is due to the impedance change experienced by the antenna when it is exposed to the windward and leeward plasmas. Further study is required before a detailed analysis can be made of these rapid oscillations and the very slow L- and S-band level changes during their overdense periods. It is evident, however, that the aft plasma is undergoing major changes in the 125 000-ft altitude region. The VHF signal-strength data recorded at

USNS Range Recoverer (fig. 30) show increases above noise level during the blackout period, particularly at the time of beryllium cap ejection and around an altitude of 125 000 ft where angle of attack increased. All other receiving stations showed similar effects at VHF but to a lesser degree. These signal-strength modulations generally confirm reflectometer indications that the aft flow field is affected by the relatively small spacecraft body motions.

Reflectometer residual reflection levels after the heat pulse are generally less at station 2 than at station 1 since the change in teflon thickness due to ablation is less. As a matter of fact, no mismatch effects due to the teflon recession are noticeable for the L-band, which is the least sensitive due to its long wavelength.

Reflection data at station 3 (fig. 27(c)) again show a very sharp rise for the L-band and S-band as the plasma exceeds their respective critical density, but no such rise occurs for the X-band. This absence of sharp rise at X-band can be explained by assuming that the electron density increases steadily through the L-band and S-band critical density and then begins to plateau near the X-band critical density. The most aft (station 4) X-band data show the same type of gradual rise and are examined more closely subsequently in the report.

Station 4 data (fig. 27(d)) have strong reflection-coefficient oscillations again where angle of attack is large and show no residual reflection after plasma decay, except for the K_a-band, since there is very little change in teflon thickness (approx. 0.1 in. (0.254 cm)).

Phase Coefficients

The phase data (fig. 28) do not change as dramatically near critical density as do the reflection-coefficient data, but the afterbody phase values do indicate the same type of oscillations due to angle of attack.

The reader is left to examine his own points of interest concerning the phase data with one word of caution; the phase measurement is accurate only when the plasma reflection coefficient is above 0.1 as previously noted. Altitude and time regions where this condition exists are shown.

Electron Density Determination

Plasma electron densities have been determined from the reflection-coefficient data. A reflection coefficient of 0.2 was chosen to indicate when $N_{e,pk}/N_{e,cr} = 0.63$ for each of the frequencies used. This choice of reflection coefficient gives a minimum inferred error in electron density for the primary data period. Electron densities derived in this manner are presented in figure 31 and table X. Also presented for comparison with the flight data are nonequilibrium calculations made with flow-field models I (ref. 28) and II

(ref. 32). The first part of this discussion of the flight data applies to the altitude regime down to cap ejection where the nose region should be free from ablation products as assumed in the theoretical model.

In the nose region (stations 1 and 2, fig. 31(a)), reasonably good agreement exists between the faired measurements and computed electron concentrations, except for altitudes above 230 000 ft (70.10 km) where the slopes are somewhat different. Also, the computed densities are consistently higher than measured values. It is important to mention, at this point, that any overprediction of electron density in the nose region means that the computed aft flow-field levels are also excessively high. In the plasma surrounding RAM C-II, most free electrons originate from ionization occurring in the nose region.

A comparison of the aft flow-field measurements with computed values is shown in figure 31(b). The two theoretical curves (inviscid layer only and merged inviscid boundary layer, model I) show a marked deviation from the measured values at altitudes above 230 000 ft (70.10 km). The deviation is attributed to ambipolar diffusion effects not included in the calculations. This conclusion is based on the good agreement between the measured and diffusion-corrected values (derived in ref. 34) shown.

Additional confidence is given to the aft reflectometer-measured values by their good agreement with ion densities (fig. 31(b)) determined from the electrostatic probe data. Data are shown for the innermost and outermost probes. Although the body locations for station 4 and the probes were not quite the same (x/D = 3.48 and 4.05, respectively), a difference in N_e of less than 20 percent would be expected at these two stations since the axial N_e gradients are small. For example, see figure 31(b) for electron density gradients between x/D = 2.30 and 3.48.

Reflectometer-determined electron density at low altitudes (below 100 000 ft (30.48 km)) is subject to errors above those experienced at high altitudes. These errors are primarily due to collision-frequency effects which decrease the sharpness of reflection-coefficient change at critical density. Figure 20 shows this slope change for a factor-of-100 increase in collision frequency. This decrease in slope thus allows a larger electron density error for a given incremental error in the measured reflection coefficient.

Because of this and other error sources at low altitudes (e.g., change in the antenna length due to ablation) which have not been analyzed in detail and because of ablation contamination effects present which were not included in the flow-field model, the comparison of low-altitude measured and computed electron densities at this time is less meaningful. It is believed, however, that errors in the aft flow field greater than a factor of 3 or 4 due to collision-frequency and antenna-length effects are unreasonable. At the present time,

there is no explanation as to why the experimental and theoretical electron densities in the low-altitude region differ by as much as a factor of 10 in some instances.

At high altitudes the boundary layer can be quite thick and ablation products in it could, as a result, influence an appreciable portion of the plasma. To minimize this effect, special attention was given to the fabrication and raw-material selection of the teflon jacket so that the amount of easily ionizable alkali metal was kept below 5 ppm (measured with neutron-activation techniques).

Evidence that there were no high-altitude ablation effects can be obtained from a comparison of RAM C-I and C-II flight data. In contrast to the nonablative nose cap on C-II, C-I had an ablating phenolic-carbon nose cone with a high sodium content (approx. 1000 ppm). The ablation of this nose did feed easily ionizable products into the flow field at low altitudes.

The two flights had almost the same trajectories, body motions, look angles from ground stations, antenna locations, and antenna patterns at the VHF and X-band telemetry frequencies. Signal-strength records were taken at several ground stations during both flights. The VHF-band signal strength measured at Bermuda shows in figure 32 that onset of attenuation is at very nearly the same altitude (276 000 ft (84.12 km)) for both RAM flights. Thus, the high-altitude aft plasmas were similar and, if there were any ablation-product effects, they were essentially the same for both flights. Also given in figure 32 is the RAM C-II signal-strength data measured from lift-off to splash at the Bermuda receiving station.

Electrostatic probe data taken on both RAM flights also show the plasma densities to be within a factor of 2 down to an altitude of 240 000 ft (73.15 km). Since it is unlikely that the aft flow-field ablation effects on RAM C-II would indentically match the combined ablation effects of the RAM C-I phenolic-carbon nose and teflon afterbody, it is believed that there were little or no ablation effects on either flight above 240 000 ft. This conclusion is also derived from chemical kinetic considerations in reference 34.

At lower altitudes, the X-band signal strengths on RAM C-I and C-II were attenuated differently; this indicated a more dense plasma for C-I (fig. 33) which experienced attenuation first. This difference in density could be due to ionizing ablation products which originate from the C-I nose cap. Electron attachment by the fluorine ablated from the C-II teflon nose cap is also a possibility since the beryllium cap is off at this time. In either case the ablation products are confined to the boundary layer. Ablation products originating from the afterbody should be the same for both flight experiments.

The X-band telemetry horn VSWR data on RAM C-II indicated when the plasma approached critical density. If one applies the same interpretation to that VSWR data as is used for the reflectometer data, the density ratio of 0.63 occurs at 167 000 ft (50.90 km)

(very near the X-band reflectometer station 3 data point). It is of interest to note that although the X-band telemetry and reflectometer horns are quite different in design, the rise of reflection occurs at essentially the same time on C-II (fig. 34).

Experimenters concerned with antenna mutual coupling may see an interesting and, perhaps, important byproduct of the cross correlation between the X-band telemetry horn VSWR, signal strength, and reflectometer horn data (fig. 34). After indicating critical density, the telemetry horn VSWR returns immediately to a small value, while the reflection level of the reflectometer continues upward (more in keeping with what would be expected since the maximum electron density had not been reached). Even as the X-band signal at Bermuda goes into hard blackout (indicating an overdense plasma), the rectangular horn VSWR is low. It is believed that the VSWR is low during this overdense period because the plasma-reflecting boundary is located in one of the nulls shown in figure 12(a); a highly reflecting layer in front of the antenna is thereby permitted while a low VSWR is still allowed. Under this condition, the microwave energy is being propogated into the teflon heat shield and perhaps to a certain degree into the subcritical plasma boundary layer adjacent to the spacecraft. These flight data show the sensitivity of the antenna design for efficiently coupling energy into boundary layers of overdense plasmas.

Plasma-Standoff-Distance Determination

Measured phase coefficients have been used to determine distance between the spacecraft and the critical density boundary for each of the body stations (fig. 35). For good distance measurements, the phase coefficient must be accurate $\left(\rho^2 \geqq 0.10\right)$ and the plasma should be overdense by a factor of approximately 10 so that θ_r approaches 180^o. These conditions are satisfied for the data shown in figure 35. At all stations the critical density is indicated to be near the spacecraft with larger separations occurring in the aft flow field. This generally agrees with profile shapes computed in references 28 and 32. The critical density layer moves closer to the vehicle surface as electron density increases to its peak value, as would be expected.

Windward and leeward variations of standoff distance are evident in the aft plasma (figs. 35(c) and (d)). As might be expected, the nose region (station 1) measurement shows no sensitivity to the angle-of-attack variations. Plasma calculations have not been made for angles of attack other than zero.

Electrostatic probe measurements on both RAM C-I and C-II flights also indicate strong electron density gradients near the vehicle surface and show the aft plasma thickness to be in excess of 7 cm. The reflectometer measurements do not verify the entire profile shape determined by the probes since the reflectometer is sensitive only to the inner portion of the profile. Attenuation effects due to absorption of the signal by the plasma and low directivity of the antennas tend to mask the outer profile properties from the reflectometer-measured quantities.

CONCLUDING REMARKS

Data from a four-frequency microwave reflectometer have been presented which were obtained during a reentry flight experiment at 25 000 ft/sec (7.62 km/sec). Plasma parameters obtained from the reflection and phase coefficients are generally in agreement with expected values except below about 100 000 ft (30.48 km) and in the aft flow field at high altitudes (above 230 000 ft (70.10 km)). The high-altitude differences are attributed to ambipolar diffusion effects not included in the theoretical flow-field model; the low-altitude deviations are not presently understood.

Data from other instrumentation, including an electrostatic probe rake, show good correlation with the reflectometer data. The relative effect of ablation has been shown by comparing this clean-flow-field data with data from an earlier flight which had easily ionizable ablation products in the flow field.

Langley Research Center,
National Aeronautics and Space Administration,
Hampton, Va., September 23, 1970.

REFERENCES

1. Grantham, William L.: Preliminary Analysis of Plasma-Sheath Electron Density Measurements at Entry Velocities. NASA TM X-1035, 1964.

2. Evans, John S.; and Schexnayder, Charles J., Jr.: Analysis of Theoretical and Experimental Electron Concentrations for RAM B3 Flight. NASA TM X-1412, 1967.

3. Akey, Norman D.; and Cross, Aubrey E. (With appendix A by Thomas G. Campbell; appendix B by Fred B. Beck; and appendix C by W. Linwood Jones, Jr.): Radio Blackout Alleviation and Plasma Diagnostic Results From a 25 000 Foot Per Second Blunt-Body Reentry. NASA TN D-5615, 1970.

4. Ginzton, Edward L.: Microwave Measurements. McGraw-Hill Book Co., Inc., 1957.

5. Jones, J. Earl; Tsai, L. L.; Rudduck, R. C.; Swift, C. T.; and Burnside, W. D.: The Admittance of a Parallel-Plate Waveguide Aperture Illuminating a Metal Sheet. IEEE Trans. Antennas Propagation, vol. AP-16, no. 5, Sept. 1968, pp. 528-535.

6. Tsai, Leonard L.: The Reflection Coefficient of a TEM Mode Parallel-Plate Waveguide Illuminating a Perfectly Reflecting Sheet. 2143-1 (NASA Grant NGR-36-008-048) Dept. Elec. Eng., Ohio State Univ., Aug. 25, 1966.

7. Burnside, W. D.; Tsai, L. L.; and Rudduck, R. C.: The Reflection Coefficient of a TEM Mode Parallel-Plate Waveguide Illuminating a Conducting Sheet: The Large Wedge Angle Case. Tech. Rep. 2143-2 (NASA Grant No. NGR-36-008-048), Electro-Sci. Lab., Ohio State Univ., Feb. 2, 1967.

8. Tsai, L. L.; and Rudduck, R. C.: The Influence of Conducting Flaps on the Reflection Coefficient of a Parallel-Plate Waveguide Illuminating a Conducting Sheet. Tech. Rep. 2143-5 (NASA Grant No. NGR-36-008-048), ElectroSci. Lab., Ohio State Univ., Apr. 1968.

9. Southworth, George C.: Principles and Applications of Waveguide Transmission. D. Van Nostrand Co., Inc., c.1950.

10. Maestre, Neil E.: Radio Attenuation Measurements. NASA CR-66888, 1970.

11. Kraus, John D.: Electromagnetics. McGraw-Hill Book Co., Inc., 1953.

12. Anisimov, A. I.; Vinogradov, N. I.; Golant, V. E.; and Konstantinov, B. P.: Method of Investigating Electron Spatial Distribution in a Plasma. Sov. Phys. – Tech. Phys., vol. 5, no. 9, Mar. 1961, pp. 939-948.

13. Golant, V. E.: Microwave Plasma Diagnostic Techniques. Soviet Phys. – Tech. Phys., vol. 5, no. 11, May 1961, pp. 1197-1310.

14. Lin, Shao-Chi; Neal, Richard A.; and Fyfe, Walter I.: Rate of Ionization Behind Shock Waves in Air. I. Experimental Results. Phys. Fluids, vol. 5, no. 12, Dec. 1962.

15. Heald, M. A.; and Wharton, C. B.: Plasma Diagnostics With Microwaves. John Wiley & Sons, Inc., c.1965.

16. Croswell, W. F.; and Bailey, M. C.: A Study of the Effect of Boundary Layer Plasma Profile Shapes Upon the Admittance of Aperture Antennas. 1968 International Antenna and Propagation Symposium, 68C 29AP, Inst. Elec. Electron. Eng., Inc. c.1968, pp. 39-45.

17. Croswell, William F.; Taylor, William C.; Swift, C. T.; and Cockrell, Capers R.: The Input Admittance of a Rectangular Waveguide-Fed Aperture Under an Inhomogeneous Plasma: Theory and Experiment. IEEE Trans. Antennas Propagation, vol. AP-16, no. 4, July 1968, pp. 475-487.

18. Taylor, W. C.: Study of the Effects of a Plasma in the Near-Zone Field of an Antenna. NASA CR-611, 1966.

19. Taylor, W. C.: An Experimental Investigation of the Interaction of Plasmas With Antennas. NASA CR-1727, 1970.

20. Bailey, Marion C.; and Swift, Calvin T.: Input Admittance of a Circular Waveguide Aperture Covered by a Dielectric Slab. IEEE Trans. Antennas Propagation, vol. AP-16, no. 4, July 1968, pp. 386-391.

21. Cockrell, C. R.: Reflection Coefficients of Pyramidal and H-Plane Horns Radiating Into Dielectric Materials. NASA TN D-5978, 1970.

22. Swift, Calvin T.; and Evans, John S.: Generalized Treatment of Plane Electromagnetic Waves Passing Through an Isotropic Inhomogeneous Plasma Slab at Arbitrary Angles of Incidence. NASA TR R-172, 1963.

23. Burnside, Walter Dennis: The Reflection Coefficient of a TEM Mode Symmetric Parallel-Plate Waveguide Illuminating a Lossless Dielectric Layer. Tech. Rep. 1691-25 (NASA Grant No. NsG-448), ElectroSci. Lab., Ohio State Univ., May 1, 1968.

24. Felsen, L. B.: Quasi-Optical Methods in Microwave Propagation and Diffraction. AFCRL-65-519, U.S. Air Force, June 11, 1965.

25. Cockrell, C. R.: Higher-Order-Mode Effects on the Aperture Admittance of a Rectangular Waveguide Covered With Dielectric and Plasma Slabs. NASA TN D-4774, 1968.

26. Jones, J. Earl; and Swift, C. T.: The Aperture Admittance of a Ground-Plane-Mounted Waveguide Illuminating a Perfectly Conducting Sheet. NASA TN D-4366, 1968.

27. Takeda, Susumu; and Tsukishima, Takashige: Microwave Study of Plasmas Produced by Electromagnetically Driven Shock Waves. J. Phys. Soc. Jap., vol. 18, no. 3, Mar. 1963, pp. 426-437.

28. Evans, John S.; Schexnayder, Charles J.; and Huber, Paul W.: Computation of Ionization in Re-Entry Flowfields. AIAA J., vol. 8, no. 6, June 1970, pp. 1082-1089.

29. Anon.: U.S. Standard Atmosphere, 1962. NASA, U.S. Air Force, and U.S. Weather Bur., Dec. 1962.

30. Craig, Richard A.: The Upper Atmosphere – Meteorology and Physics. Academic Press, Inc., c.1965.

31. Anon.: U.S. Standard Atmosphere Supplements, 1966. Environ. Sci. Serv. Admin., NASA, and U.S. Air Force.

32. Webb, H., Jr.; Dresser, H.; Korkan, K.; and Raparelli, R.: Theoretical Flow Field Calculations for Project RAM. NASA CR-1308, 1969.

33. Mayhan, John W.; Caldecott, Ross; and Bohley, Peter: Antenna Impedance in a Reentry Environment. IEEE Trans. Antennas Propagation, vol. AP-16, no. 5, Sept. 1968, pp. 573-577.

34. Huber, P. W.; Evans, J. S.; and Schexnayder, C. J.: Comparison of Theoretical and Flight-Measured Ionization in a Blunt Body Reentry Flow Field. AIAA Pap. No. 70-756, June-July 1970.

TABLE I.- RAM C-II RADIO-FREQUENCY SYSTEMS

Purpose	Frequency band	Antenna type	Antenna location		Power	Type ground plane
			x/D*	x, in. (cm)		
Real-time telemetry	VHF (259.7 MHz)	Array of circumferential slots	3.20	38.35 (97.41)	6.6 W (average)	Teflon covered
Delayed-time telemetry	VHF (225.7 MHz)	Array of circumferential slots	3.76	45.15 (114.68)	6.9 W (average)	
Real-time telemetry	X (9210 MHz)	Four rectangular horns	2.65	31.74 (80.62)	600 W (peak)	
Radar beacon	C (5800 MHz)	One rectangular horn	3.50	42.04 (106.78)	840 W (peak)	
Reflectometer experiment	†L (1116 MHz)	See table IV	0.15	1.76 (4.47) (Sta. 1)	≈75 mW (average)	See table IV
	S (3348 MHz)		.76	9.12 (23.16) (Sta. 2)		
	X (10 044 MHz)		2.30	27.58 (70.05) (Sta. 3)		
	K_a (35 000 MHz)		3.48	41.75 (106.04) (Sta. 4)		

*D = 12 in. (30.48 cm).

†No L-band antenna at station 1.

TABLE II.- S-BAND REFLECTOMETER COMPONENT SPECIFICATIONS

[Total RF cable, 17.6 ft (5.37 m); typical insertion loss, 1.3 dB/ft (0.39 dB/m)]

Component	Input VSWR	Output VSWR	Insertion loss, dB	Isolation between channels, dB	Coupling, dB	Directivity, dB
Isolator	1.12	1.12	0.2 (Forward) 31 (Reverse)	---	---	- - - - - - - - - - - - - - -
Monitor[a]	1.05	1.15	6.85	32	20	27 39 Forward Reverse
		1.16				27 26
		1.09				30 40
		1.15				34 25
Unit probe[a]	1.02	1.03	0.25	---	20	0
	1.04	1.10	.20			
	1.10	1.09	.25			
	1.14	1.12	.20			
Antenna[a]	<1.06	---	0.30	---	---	≈6
			.70			
			.25			
			.30			

[a]Properties are listed in order for stations 1, 2, 3, 4.

TABLE III.- ANTENNA AND ELECTROSTATIC PROBE LOCATIONS ON RAM C-II PAYLOAD

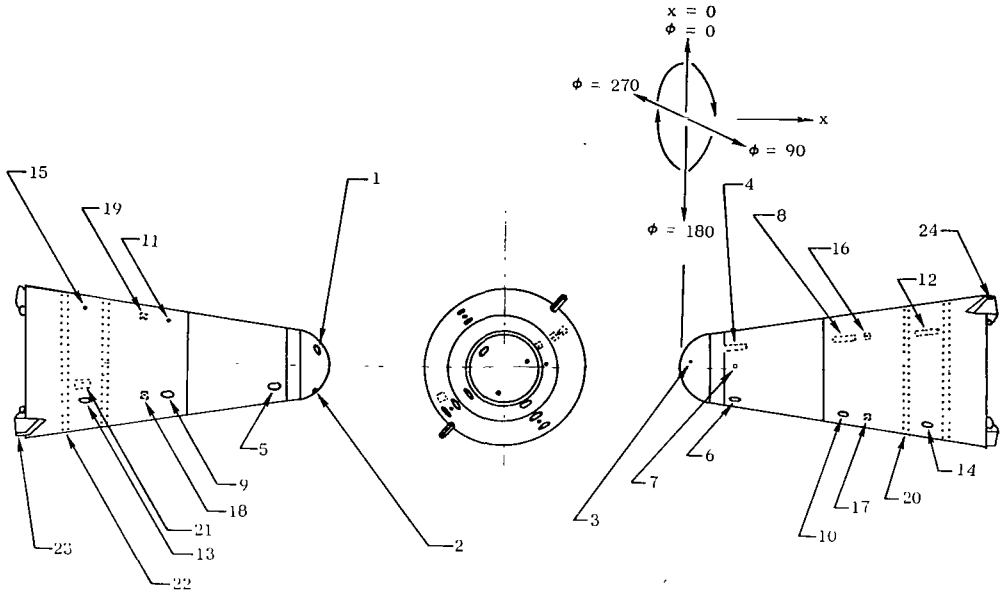

Number	Part Function	x,† in. (cm)	x/D*	Body station	ϕ,† deg
	Reflectometer antenna:				
1	S-band	1.76 (4.47)	0.15	1	310
2	X-band				190
3	K_a-band				70
	Reflectometer antenna:				
4	L-band	9.12 (23.16)	0.76	2	55
5	S-band				235
6	X-band				145
7	K_a-band				87
	Reflectometer antenna:				
8	L-band	27.58 (70.05)	2.30	3	55
9	S-band				235
10	X-band				145
11	K_a-band				325
	Reflectometer antenna:				
12	L-band	41.75 (106.04)	3.48	4	55
13	S-band				235
14	X-band				145
15	K_a-band				325
16	X-band telemetry horn (9210 MHz)	31.74 (80.62)	2.65	---	55
17					145
18					235
19					325
20	VHF ring antenna (259.7 MHz)	38.35 (97.41)	3.20	---	---
21	C-band rectangular horn (5800 MHz)	42.04 (106.78)	3.50		252
22	VHF ring antenna (225.7 MHz)	45.15 (114.68)	3.76		---
	Probe:				
23	Electrostatic	48.59 (123.42)	4.05	---	220
24	Thermocouple				40

†Center-line location of parts.
*D = 12 in. (30.48 cm).

TABLE IV.- REFLECTOMETER ANTENNA CHARACTERISTICS

Antenna location \ Antenna property		Frequency band	Aperture geometry	Dielectric plug	Ground plane
Station 1	Cap on	S X K_a	Open-end circular waveguide	Quartz	Metallic
	Cap off			Teflon	Teflon covered*
Stations 2, 3, 4		S	Open-end circular waveguide	Teflon	Teflon covered*
		X	Conical horn (14 dB gain)		
		K_a	Conical horn (17 dB gain)		
Stations 2, 3, 4		L	Open-end rectangular waveguide	Formica	Teflon covered*

*Thin vapor-deposited metallic sleeves extended through teflon heat shield.

TABLE V.- RAM C-II RECEIVING STATIONS AND TYPE OF DATA RECEIVED

Frequency \ Receiving station	Ground		Ship		Airplane	
	Wallops	Bermuda	Range recoverer	Twin Falls victory[a]	NASA 438	NASA 432
VHF (229.7 and 259.7 MHz)	Signal strength (left- and right-hand polarization) and telemetry				Telemetry	
C-band beacon (5800 MHz)		Radar (sum and difference channel video data) and signal strength		Radar and signal strength		
X-band (9210 MHz)	Telemetry	Signal strength (horizontal and vertical polarization) and telemetry			Telemetry	

[a] This station did not receive left-hand polarization.

TABLE VI.- RAM C-I ANTENNA AND EXPERIMENT CONFIGURATION

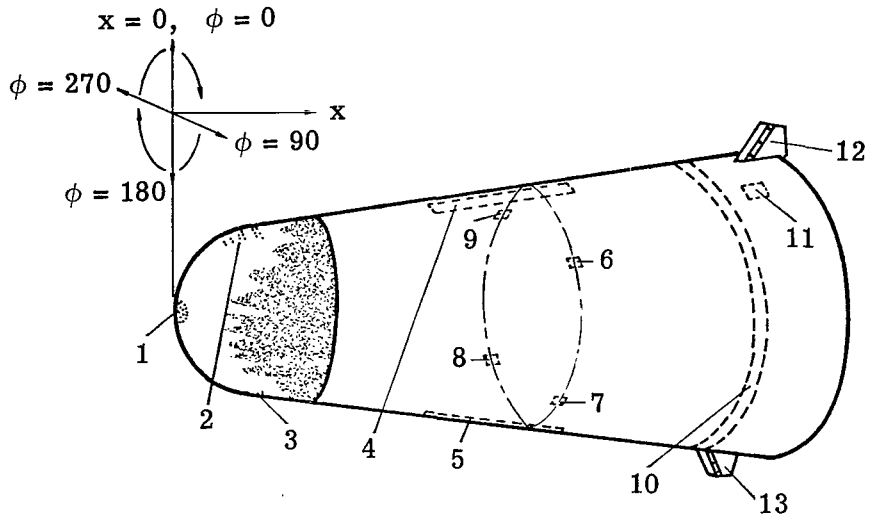

Part		x,		ϕ,	x/D
Number	Function	in.	(cm)	deg (a)	(b)
	Water injection nozzle:				
1	Stagnation	0	(0)	---	0
2	Lateral	6.0	(15.2)	0	.48
3	Lateral	6.0	(15.2)	180	.48
	Antenna:				
4	VHF slot (259.7 MHz)	29.6	(75.2)	0	2.36
5	VHF slot (259.7 MHz)	29.6	(75.2)	180	2.36
6	X-band horn (9210 MHz)	32.6	(82.8)	60	2.60
7	X-band horn (9210 MHz)	32.6	(82.8)	150	2.60
8	X-band horn (9210 MHz)	32.6	(82.8)	240	2.60
9	X-band horn (9210 MHz)	32.6	(82.8)	330	2.60
10	VHF ring (225.7 MHz)	43.0	(109.2)	---	3.42
11	C-band horn (5700 MHz)	46.6	(118.4)	30	3.71
	Probe:				
12	Electrostatic	48.6	(123.4)	0	3.87
13	Thermocouple	48.6	(123.4)	180	3.87

[a] Center-line location of parts.
[b] D = 12.56 in. (31.90 cm).

TABLE VII.- ALTITUDES AND VELOCITIES USED IN FLOW-FIELD MODEL I CALCULATIONS

Altitude		Velocity	
ft	km	ft/sec	km/sec
70.0×10^3	21	12.75×10^3	3.89
78.0	24	16.50	5.03
82.5	25.1	17.80	5.43
100.5	30.6	21.70	6.61
110.6	33.7	22.90	6.98
131.2	40.0	24.25	7.39
156	48	24.82	7.57
175	53	25.00	7.62
202	62	25.12	7.66
233	71	25.12	7.66
263	80	25.12	7.66

TABLE VIII.- ALTITUDES, VELOCITIES, AND BODY NORMALS USED IN FLOW-FIELD MODEL II CALCULATIONS

Case	Altitude		Velocity		Nose radius		Wall, temperature, ^{o}K
	ft	km	ft/sec	km/sec	ft	m	
1	60.0×10^3	18.29	8.02×10^3	2.44	0.5	0.152	700
2	80.3	24.48	16.78	5.12	↓	↓	↓
3	149.8	45.66	24.75	7.54			
4	250.3	76.29	25.13	7.66			
5	269.8	82.24	25.09	7.65			
6	299.9	91.41	25.09	7.65			
7	325.5	99.21	25.03	*7.63			
8	*80.3	*24.48	*16.78	*5.12	.527	.161	
9	†149.8	†45.66	†24.75	†7.54	.527	.161	

* Value same as for case 2.
† Value same as for case 3.

Axial coordinate, x, for –			
Cases 1 to 7 (D = 1 ft (0.3048 m))		Cases 8 and 9 (D = 1.0541 ft (0.3213 m))	
ft	m	ft	m
0	0	0	0
.1475	.0450	.1555	.0474
.4100	.1250	.4322	.1317
.7600	.2316	.8011	.2442
2.3000	.7010	2.4244	.7390
3.4800	1.0607	3.6683	1.1181
3.9800	1.2131	4.1953	1.2787

TABLE IX.- ALTITUDE, VELOCITY, AND TIME OF RAM C-II REENTRY TRAJECTORY

Altitude		Velocity		Time from lift-off, sec
ft	km	ft/sec	km/sec	
450×10^3	137.16	24.9×10^3	7.59	363.9
445	135.64	24.9	7.59	364.6
440	134.11	24.9	7.59	365.4
435	132.59	24.9	7.59	366.2
430	131.06	24.9	7.59	366.9
425	129.54	24.9	7.59	367.7
420	128.02	24.9	7.59	368.4
415	126.49	24.9	7.59	369.3
410	124.97	24.9	7.59	370.0
405	123.44	24.9	7.59	370.8
400	121.92	24.9	7.59	371.6
395	120.40	25.0	7.62	372.3
390	118.87	25.0	7.62	373.1
385	117.35	25.0	7.62	373.8
380	115.82	25.0	7.62	374.7
375	114.30	25.0	7.62	375.4
370	112.78	25.0	7.62	376.2
365	111.25	25.0	7.62	376.9
360	109.73	25.0	7.62	377.7
355	108.20	25.0	7.62	378.5
350	106.68	25.0	7.62	379.3
345	105.16	25.0	7.62	380.1
340	103.63	25.0	7.62	380.5
335	102.11	25.0	7.62	381.6
330	100.58	25.0	7.62	382.3
325	99.06	25.0	7.62	383.1
320	97.54	25.0	7.62	383.8
315	96.01	25.1	7.65	384.7
310	94.49	25.1	7.65	385.4
305	92.96	25.1	7.65	386.2
300	91.44	25.1	7.65	386.9
295	89.92	25.1	7.65	387.7
290	88.39	25.1	7.65	388.5
285	86.87	25.1	7.65	389.3
280	85.34	25.1	7.65	390.0
275	83.82	25.1	7.65	390.8
270	82.30	25.1	7.65	391.6
265	80.77	25.1	7.65	392.3
260	79.25	25.1	7.65	393.1
255	77.72	25.1	7.65	393.8
250	76.20	25.1	7.65	394.7
245	74.68	25.1	7.65	395.4
240	73.15	25.1	7.65	396.2
235	71.63	25.1	7.65	396.9

Altitude		Velocity		Time from lift-off, sec
ft	km	ft/sec	km/sec	
230×10^3	70.10	25.1×10^3	7.65	397.7
225	68.58	25.1	7.65	398.4
220	67.06	25.1	7.65	399.3
215	65.53	25.1	7.65	400.0
210	64.01	25.1	7.65	400.8
205	62.48	25.1	7.65	401.6
200	60.96	25.1	7.65	402.3
195	59.44	25.1	7.65	403.1
190	57.91	25.1	7.65	403.8
185	56.39	25.1	7.65	404.7
180	54.86	25.1	7.65	405.4
175	53.34	25.0	7.62	406.2
170	51.82	25.0	7.62	406.9
165	50.29	25.0	7.62	407.8
160	48.77	24.9	7.59	408.5
155	47.24	24.9	7.59	409.3
150	45.72	24.8	7.56	410.1
145	44.20	24.7	7.53	410.8
140	42.67	24.5	7.47	411.7
135	41.15	24.4	7.44	412.4
130	39.62	24.2	7.38	413.2
125	38.10	24.0	7.32	414.0
120	36.58	23.7	7.22	414.8
115	35.05	23.3	7.10	415.7
110	33.53	22.8	6.95	416.5
105	32.00	22.3	6.80	417.3
100	30.48	21.5	6.55	418.3
95	28.96	20.7	6.31	419.2
90	27.43	19.7	6.00	420.1
85	25.91	18.4	5.61	421.1
80	24.38	16.8	5.12	422.2
75	22.86	15.1	4.60	423.3
70	21.34	12.9	3.93	424.8
65	19.81	10.8	3.29	426.3
60	18.29	8.4	2.56	428.3
55	16.76	6.1	1.86	430.8
50	15.24	4.2	1.28	434.1
45	13.72	2.5	.76	438.9
40	12.19	1.29	.39	446.2

TABLE X.- REFLECTOMETER-DETERMINED ELECTRON DENSITIES

Body station	x/D	Frequency band	Time from lift-off, sec, at –		Altitude, ft (km), at –	
			Onset of 20% reflection level[a]	Decay of 20% reflection level[a]	Onset[a]	Decay[a]
1	0.15	S	390.3	[b]424.3	277×10^3 (84)	[b]72.6×10^3 (22.1)
		X	392.3	420.0	264 (80)	90.3 (27.5)
		K_a	[c]397.3	[d]419.0	[c]236 (72)	[b c]95.0 (29.0)
2	0.76	L	390.3	423.4	277×10^3 (84)	74.7×10^3 (22.8)
		S	393.8	422.3	254.8 (77.7)	79.6 (24.3)
		X	397.8	419.2	229 (70)	[b]93.7 (28.6)
		K_a	414.0	417.8	125 (38)	102 (31)
3	2.30	L	391.6	421.8	269×10^3 (82)	81.8×10^3 (24.9)
		S	395.8	420.8	242 (74)	86.3 (26.3)
		X	[e]406.8	[e]417.8	[e]170 (52)	[e]102 (31)
		K_a	------	------	----------	----------
4	3.48	L	392.8	421.0	262×10^3 (80)	85×10^3 (26)
		S	397.0	419.6	234.8 (72)	92 (28)
		X	[e]407.8	[e]415.3	[e]164 (50)	[e]117 (36)
		K_a	------	------	----------	----------

[a]At these conditions, $N_{e,pk}/N_{e,cr} = 0.63$ for each respective frequency.

[b]At low altitudes, antenna detuning due to length changes prevents reflection coefficient from crossing through 20 percent point where plasma is dropping below critical density. Sharp cessation of reflected signal modulation (due to windward-leeward plasma variations) is interpreted to be plasma decay.

[c]Not derived from 20-percent-reflection-level criterion (see discussion in text).

[d]Effects of gross antenna detuning caused by antenna length changes and removal of beryllium cap make determination of this critical density decay time somewhat ambiguous.

[e]Oscillations in measured reflection coefficients due to windward-leeward plasma changes cause some ambiguity in this data point. A mean of reflection-coefficient curve was used to estimate this data point.

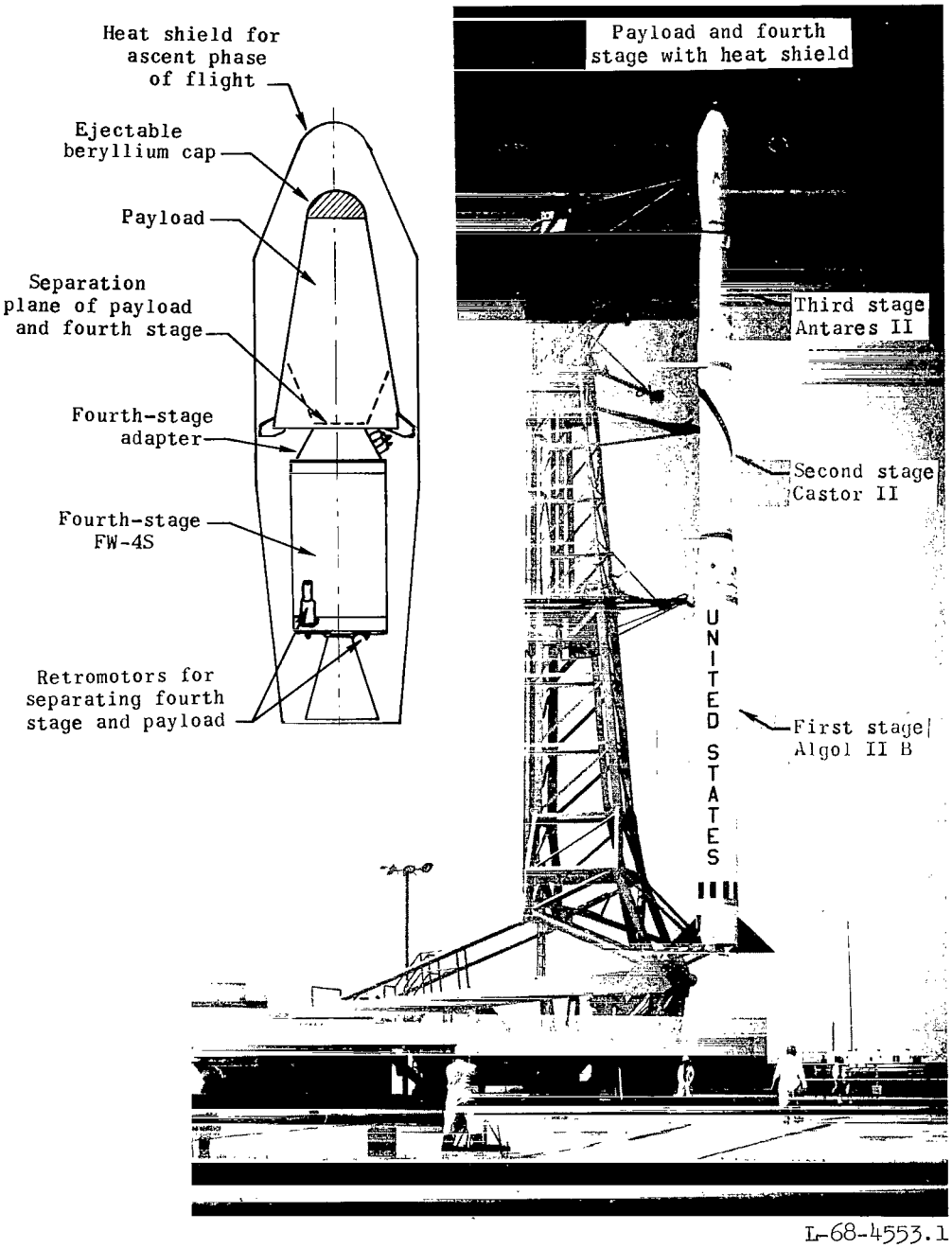

Figure 1.- Scout vehicle and payload.

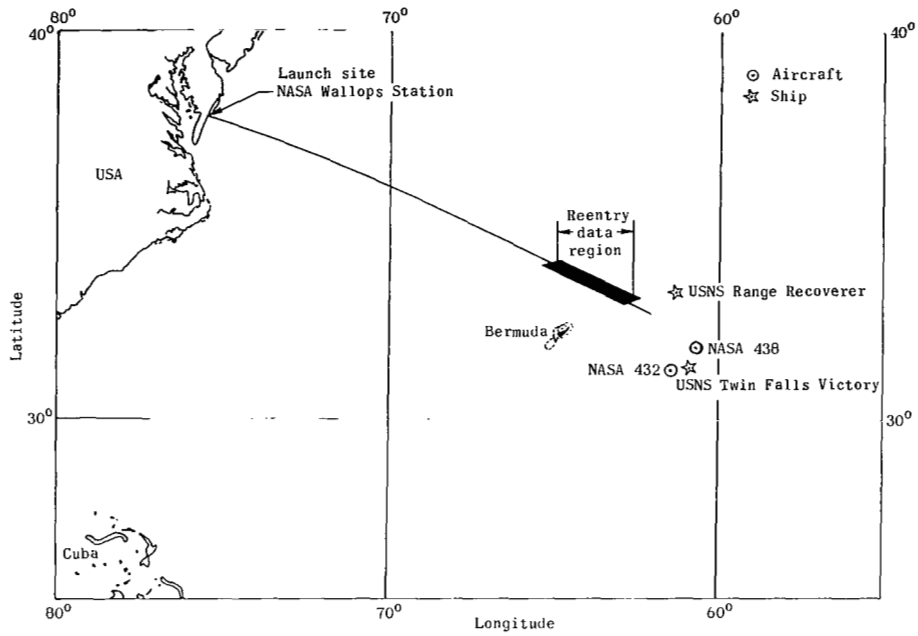

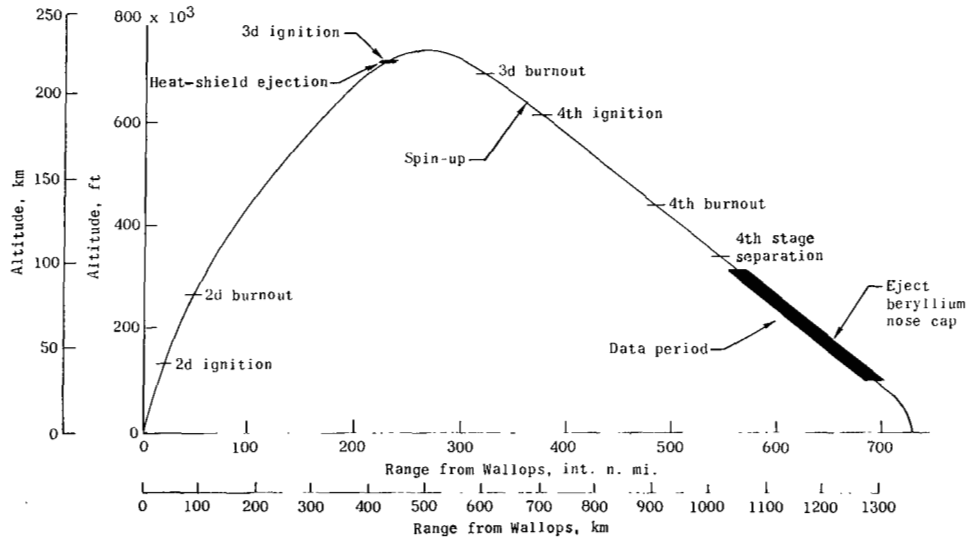

Figure 2.- Trajectory plan view and reentry events.

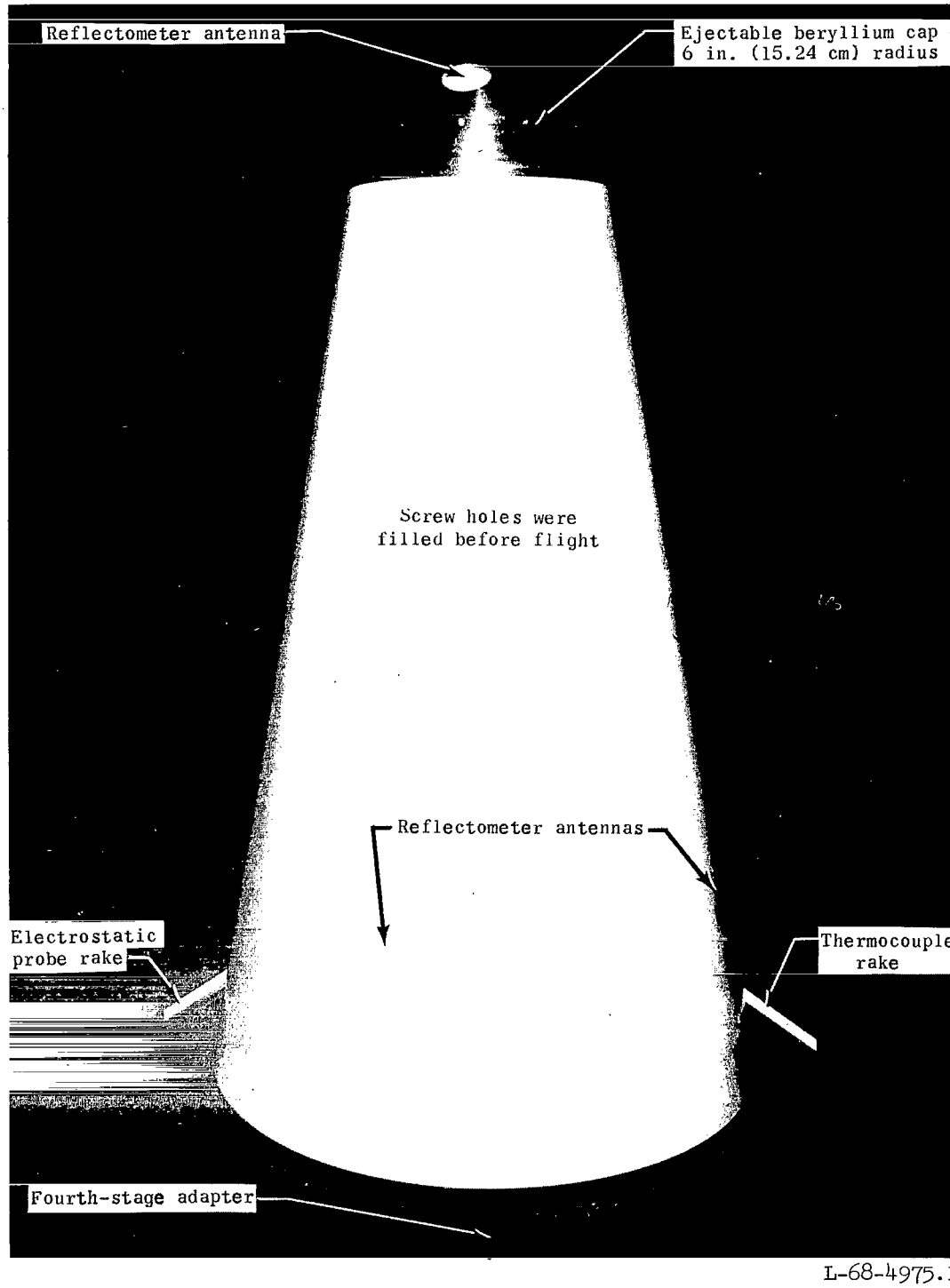

L-68-4975.1

Figure 3.- Flight payload with beryllium nose cap on.

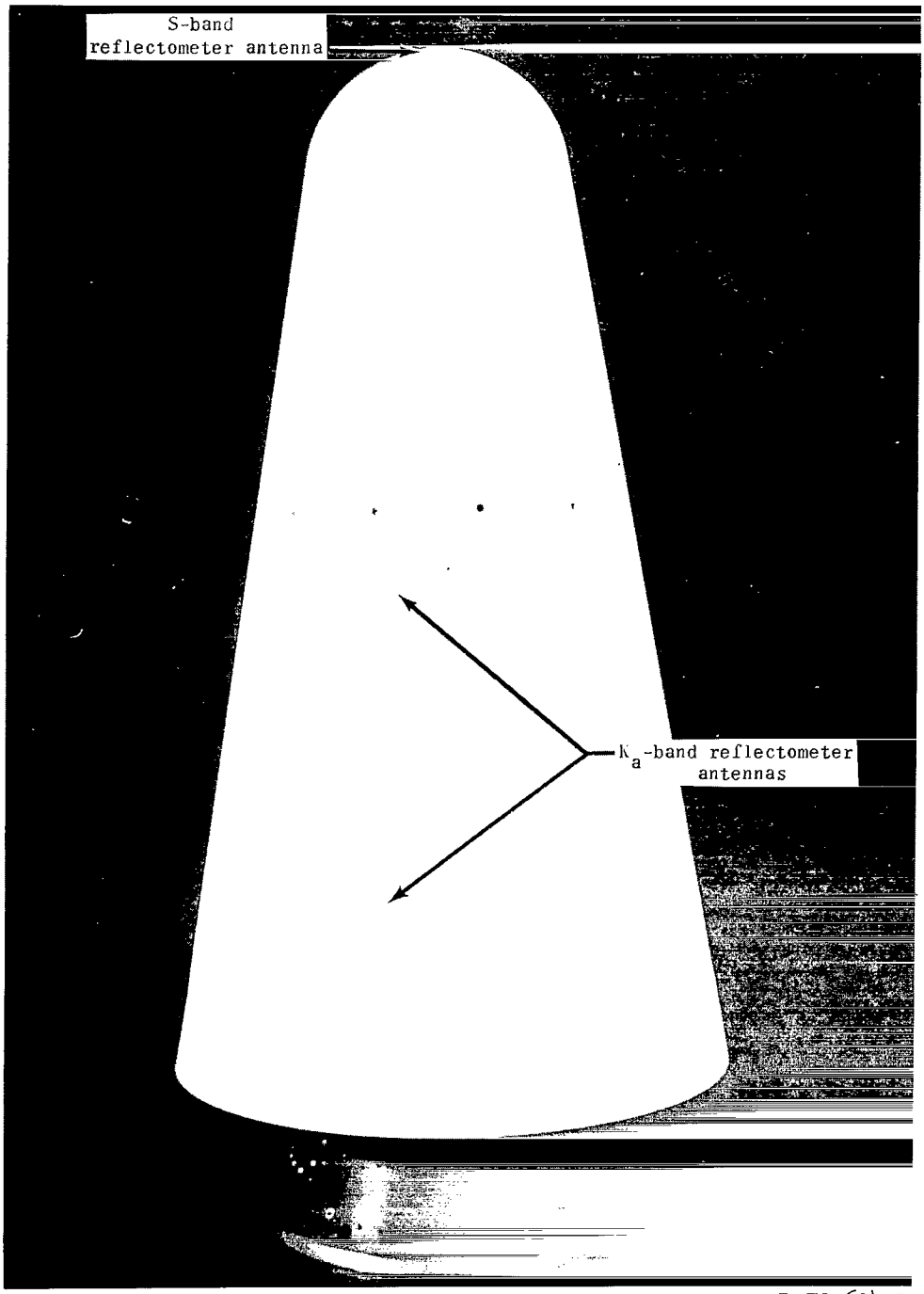

L-70-624.1

Figure 4.- RAM C-II payload with beryllium nose cap off.

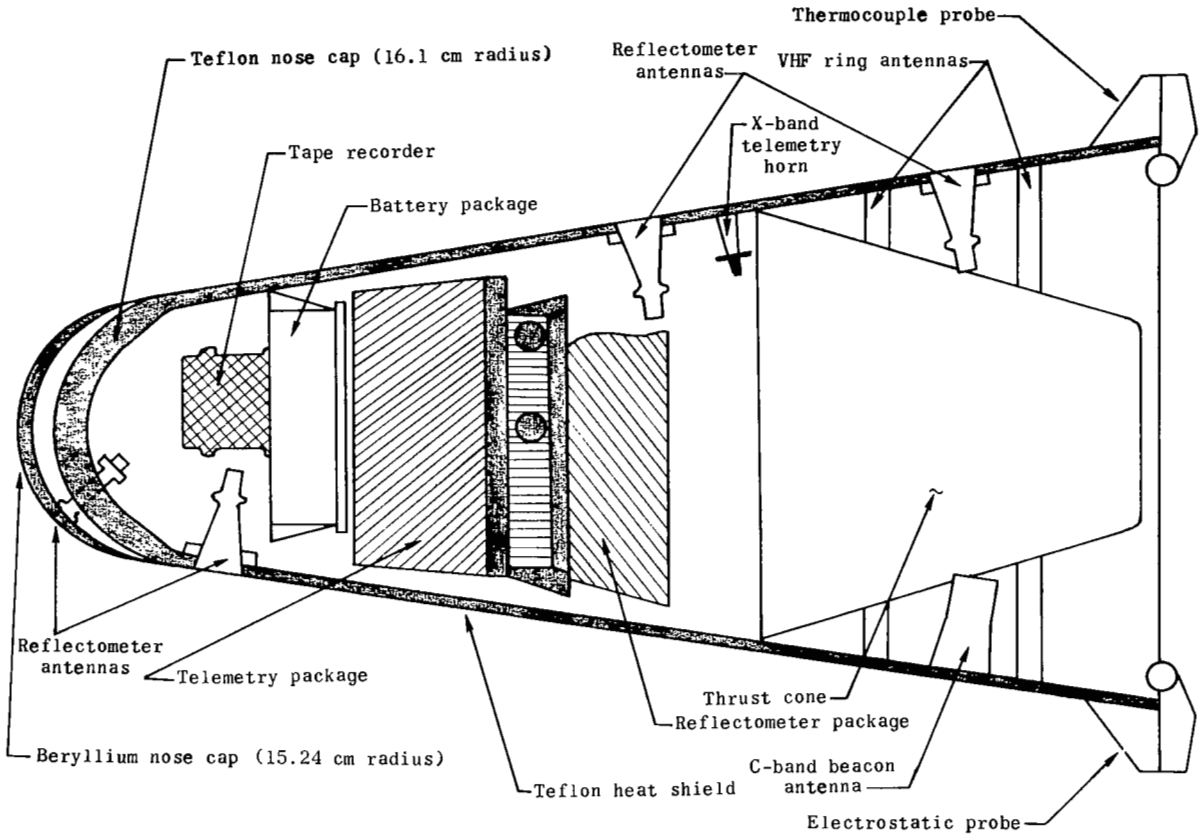

Figure 5.- Payload configuration depicting instrumentation and experiment systems.

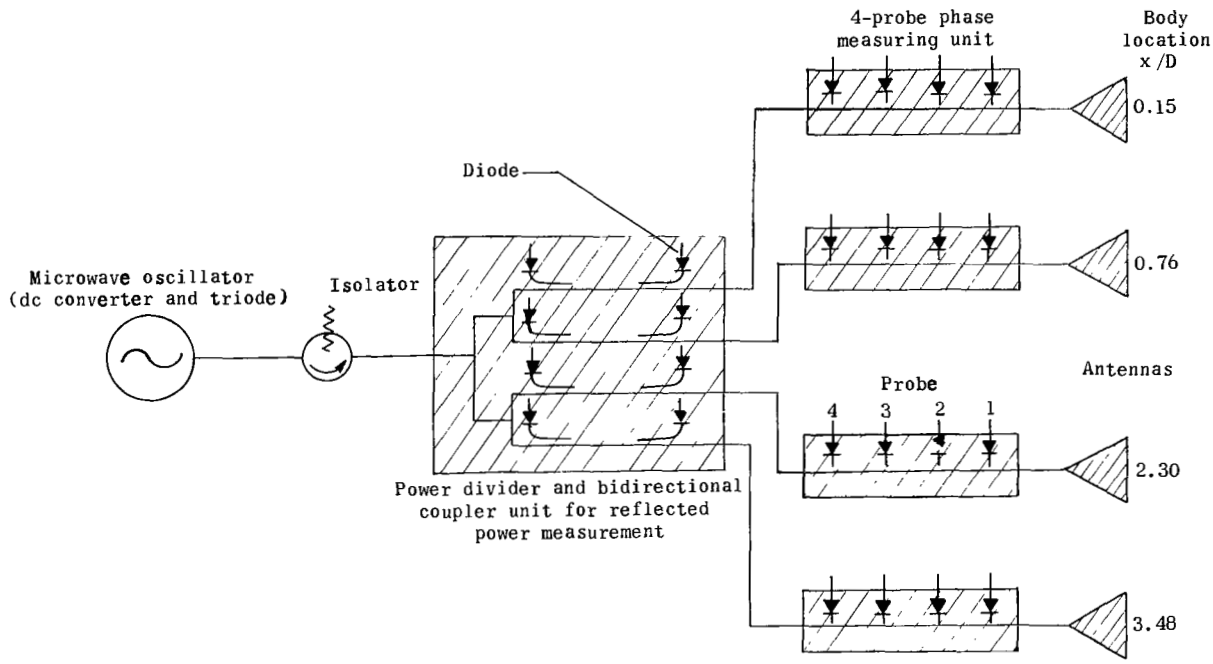

Figure 6.- S-band reflectometer block diagram.

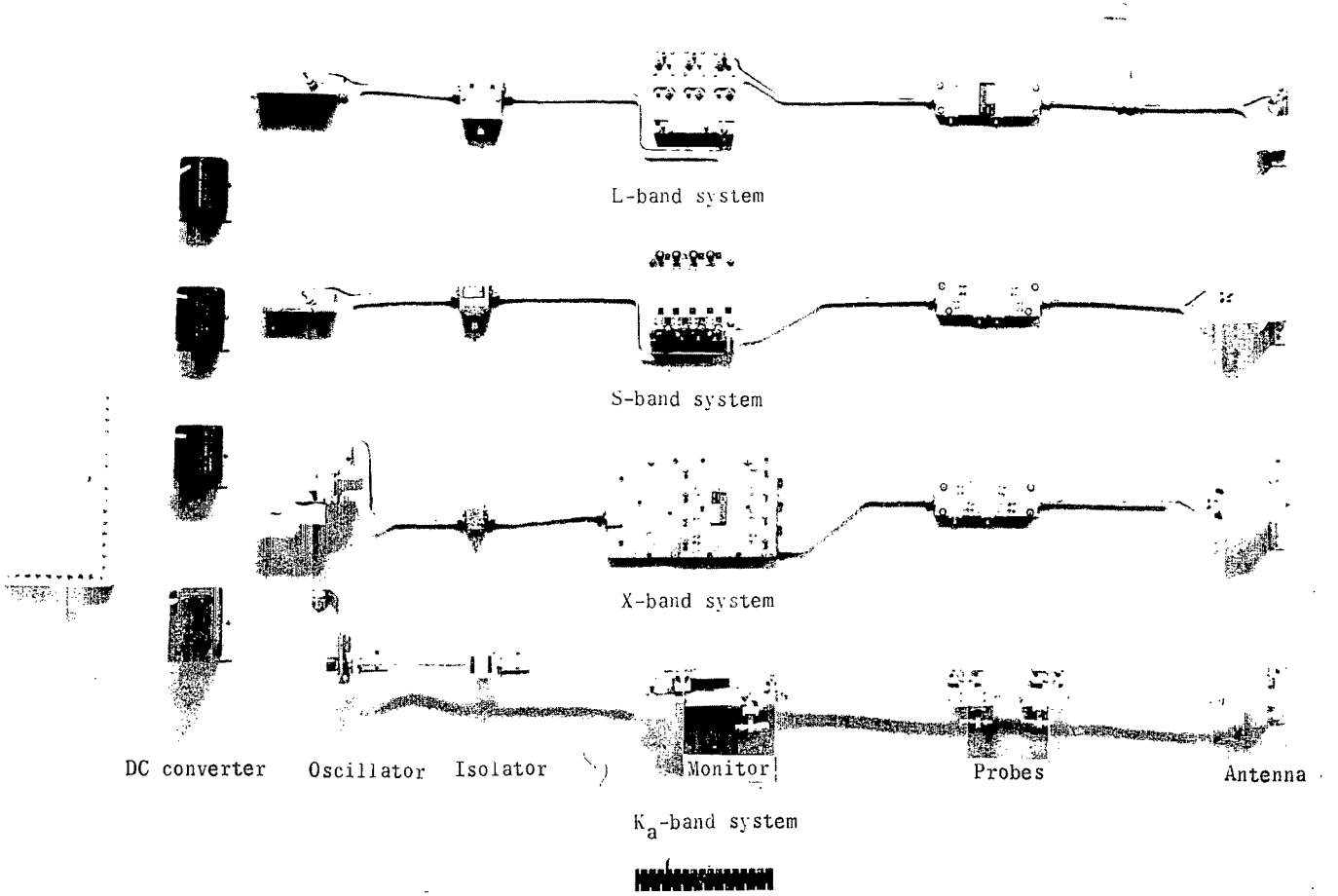

L-70-1389.1

Figure 7.- Reflectometer flight components (only one probe unit and antenna shown for each frequency).

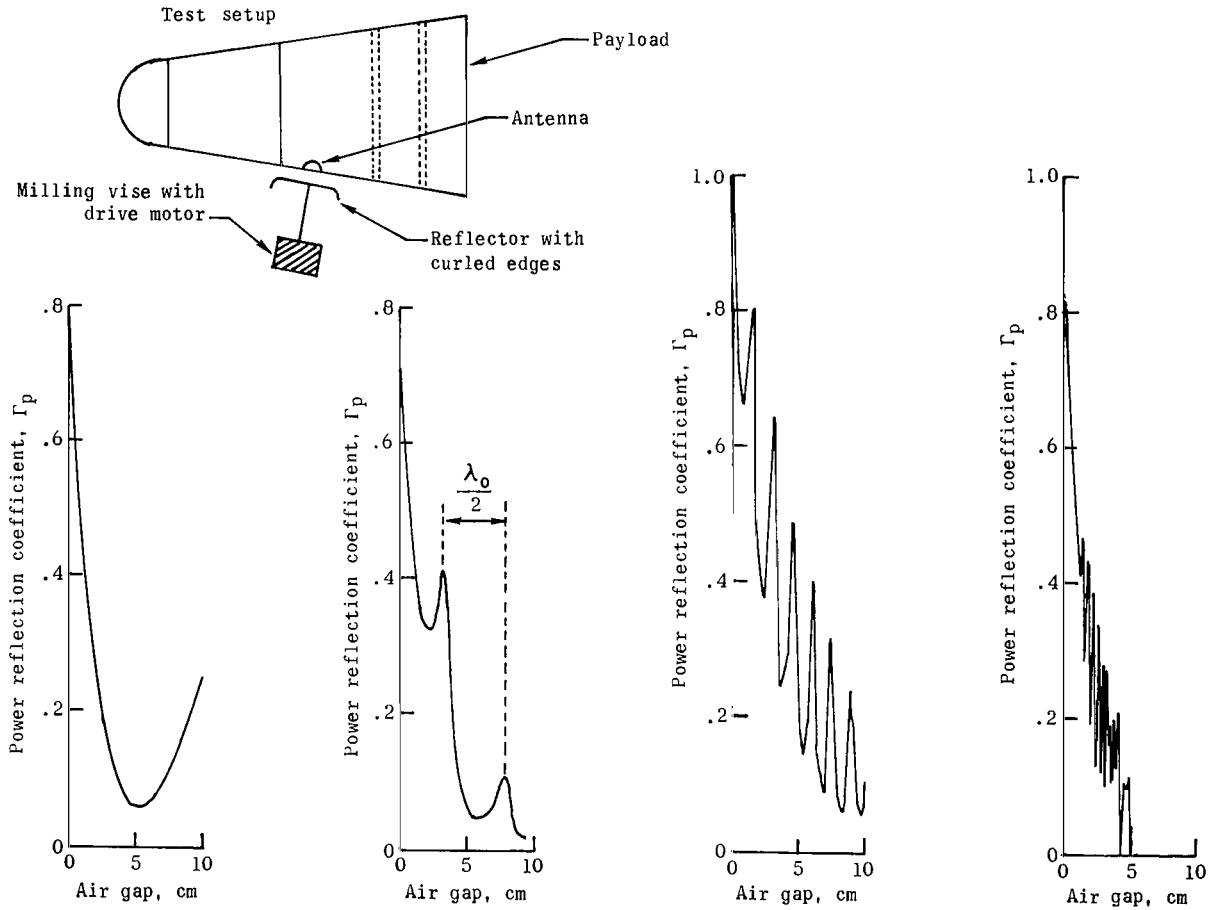

(a) L-band (30.5 cm × 30.5 cm reflector).

(b) S-band (12.7 cm × 12.7 cm reflector).

(c) X-band (12.7 cm × 12.7 cm reflector).

(d) K_a-band (12.7 cm × 12.7 cm reflector).

Figure 8.- Measured antenna signatures for station 3 (x/D = 2.30).

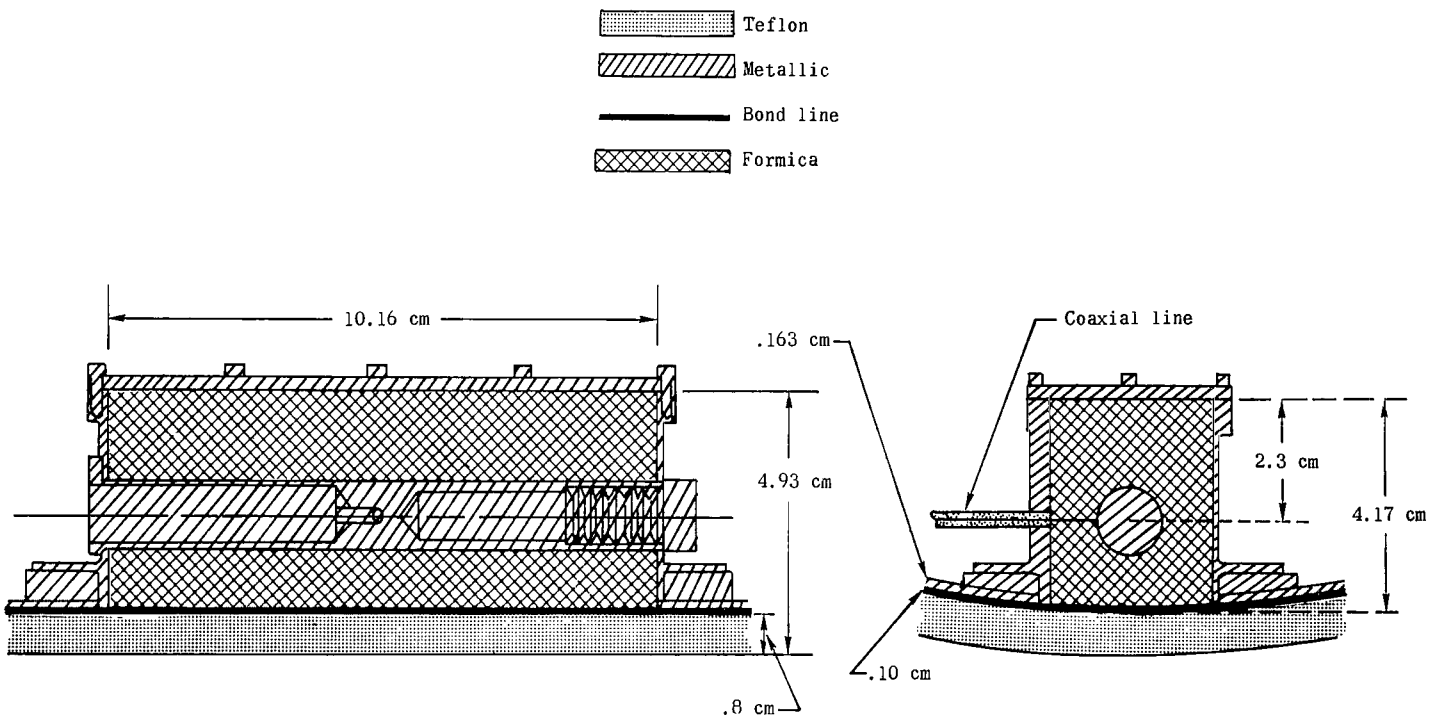

(a) L-band.

Figure 9.- Reflectometer antenna configurations at stations 3 and 4.

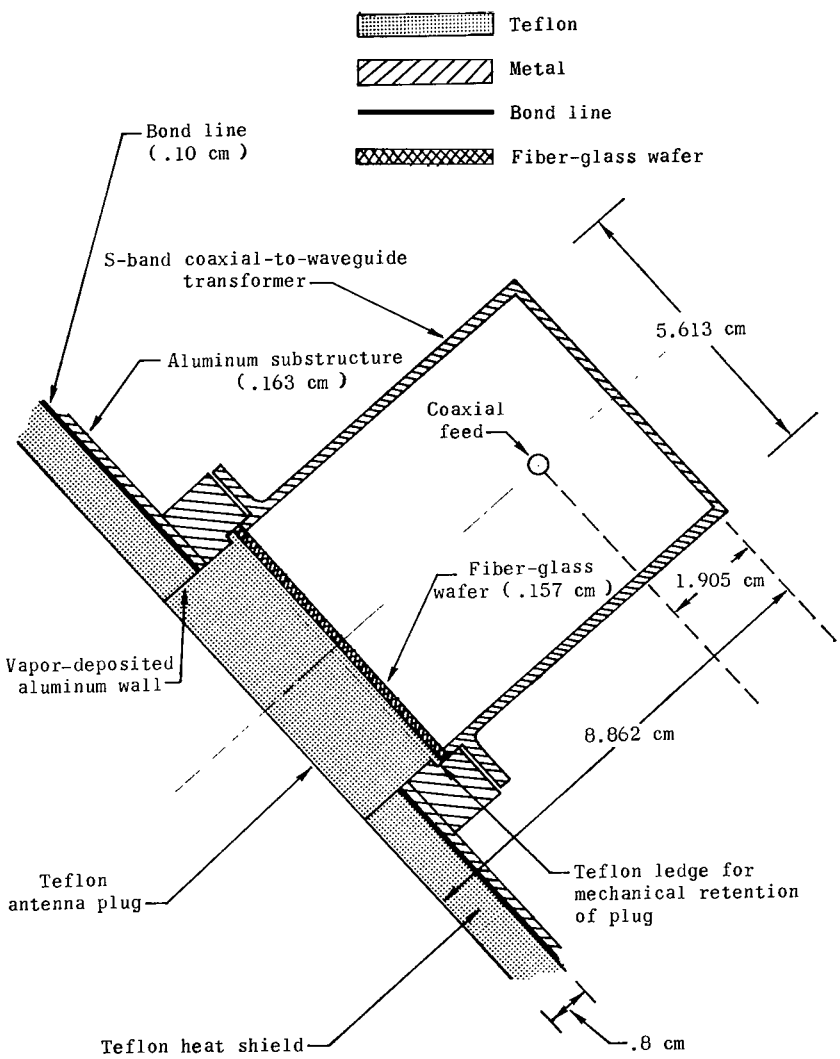

(b) S-band.

Figure 9.- Continued.

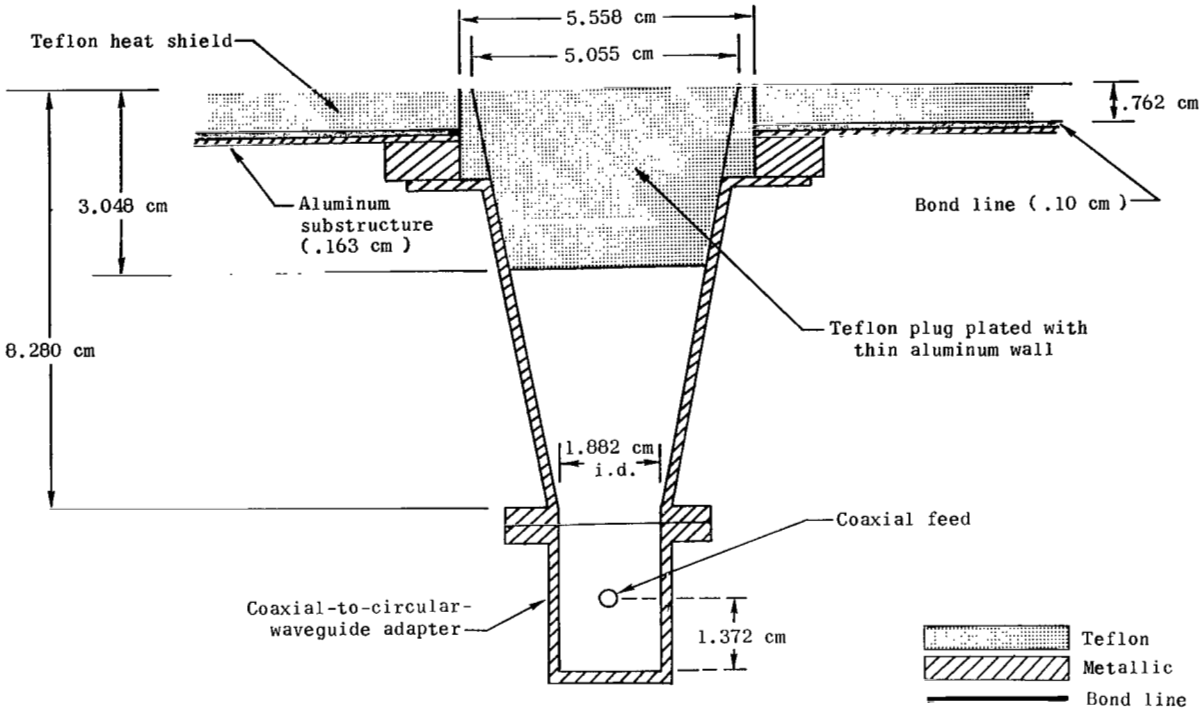

(c) X-band.

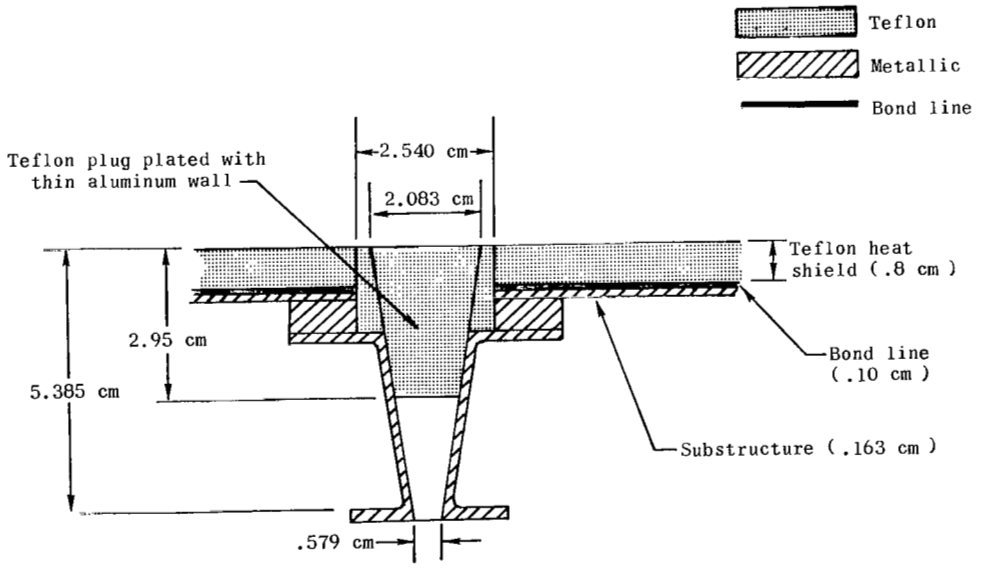

(d) K_a-band.

Figure 9.- Concluded.

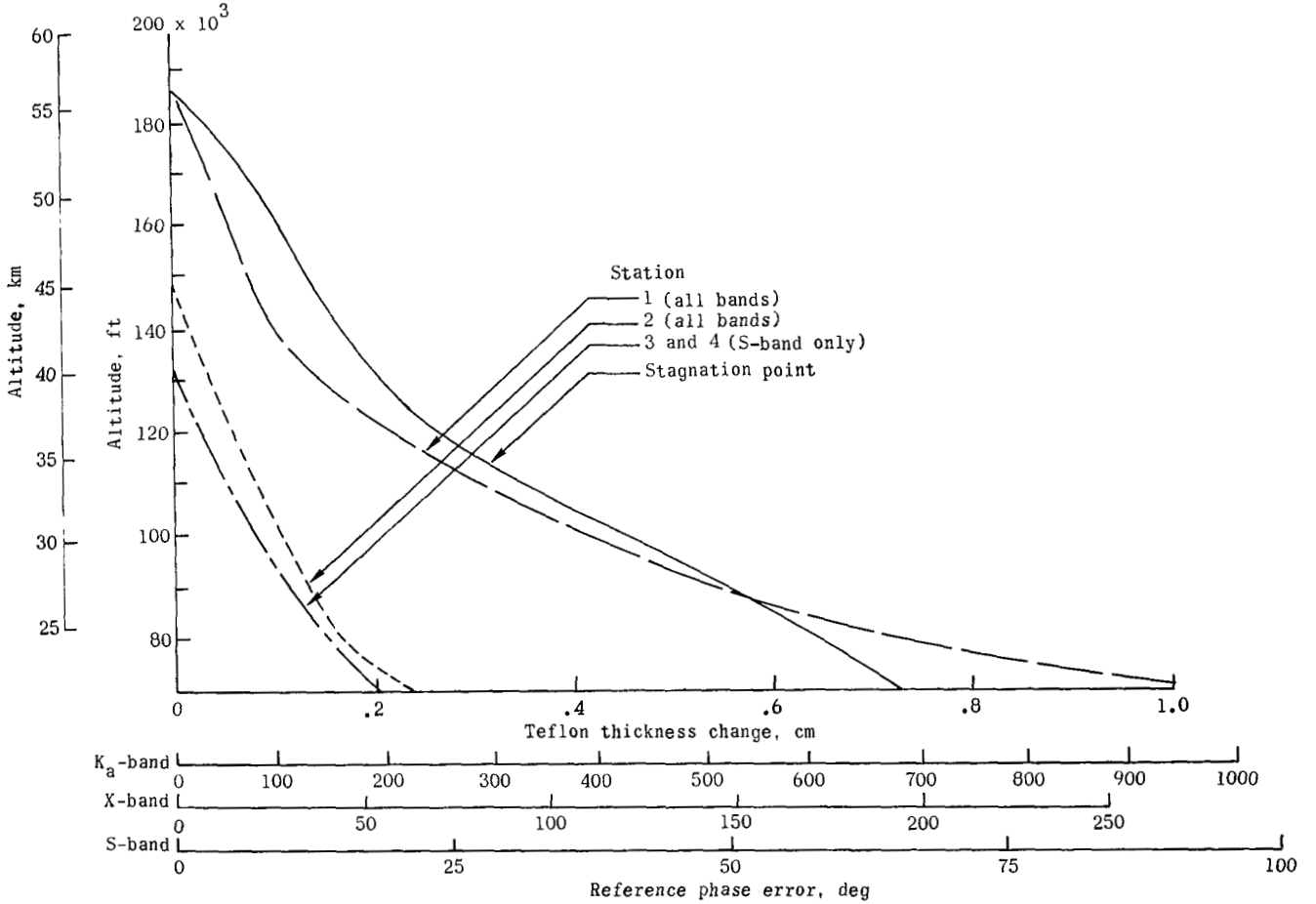

Figure 10.- Antenna length change due to teflon-heat-shield ablation. Reference phase error, $720 \frac{t}{\lambda_o}\sqrt{\epsilon - \left(\frac{\lambda_o}{\lambda_c}\right)^2}$.

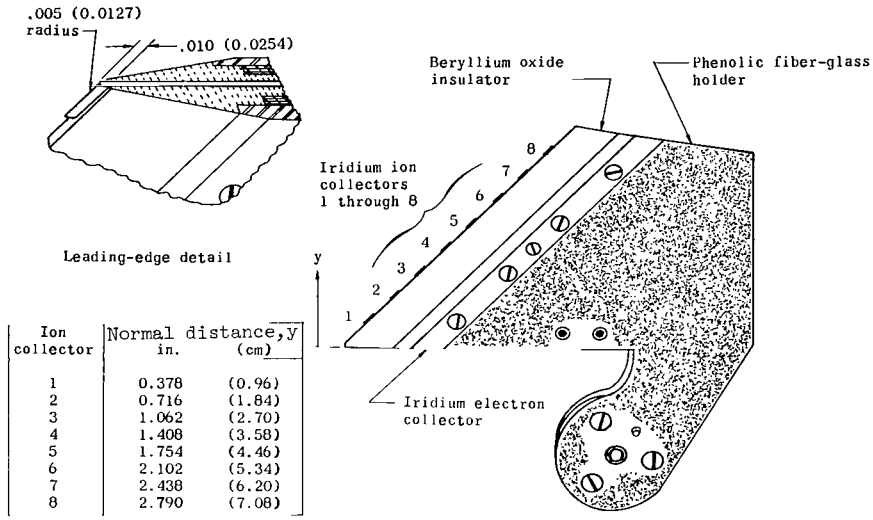

Ion collector	Normal distance, y in.	(cm)
1	0.378	(0.96)
2	0.716	(1.84)
3	1.062	(2.70)
4	1.408	(3.58)
5	1.754	(4.46)
6	2.102	(5.34)
7	2.438	(6.20)
8	2.790	(7.08)

(a) Electrostatic probe.

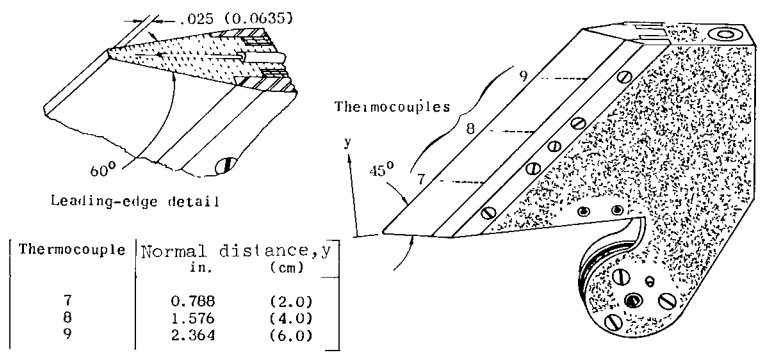

Thermocouple	Normal distance, y in.	(cm)
7	0.788	(2.0)
8	1.576	(4.0)
9	2.364	(6.0)

(b) Thermocouple probe.

Figure 11.- Probe configurations. All linear dimensions are in inches (centimeters).

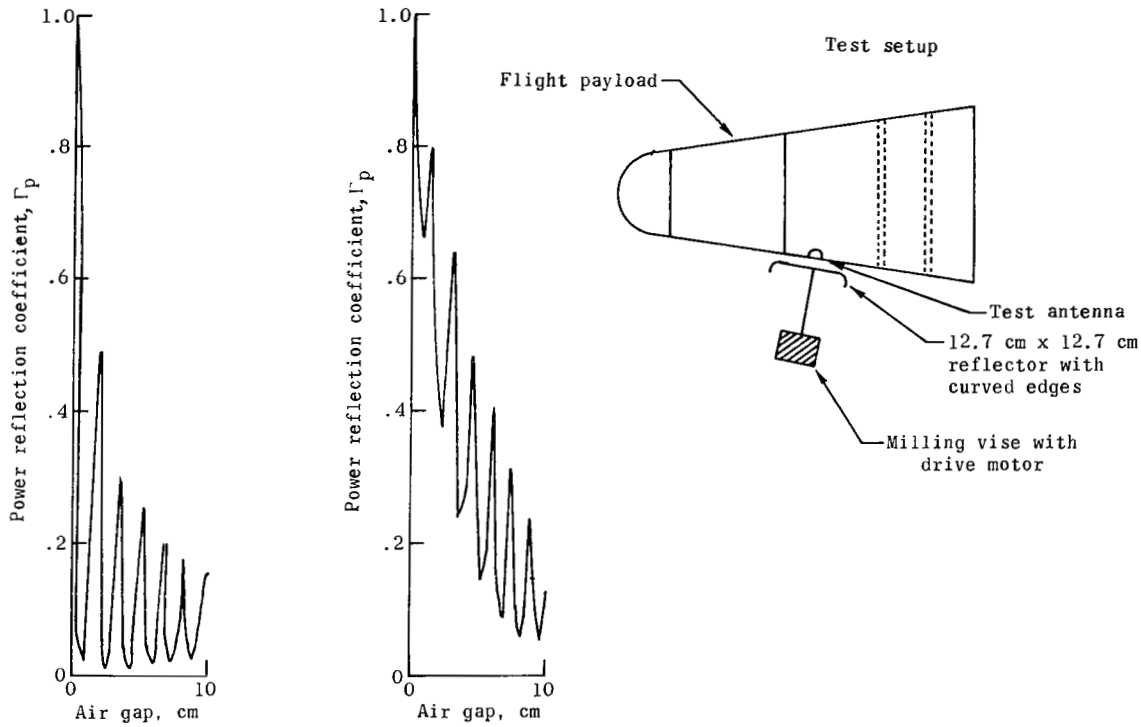

(a) Rectangular telemetry horn.

(b) Conical reflectometer horn at station 3.

Figure 12.- Measured antenna signatures for X-band.

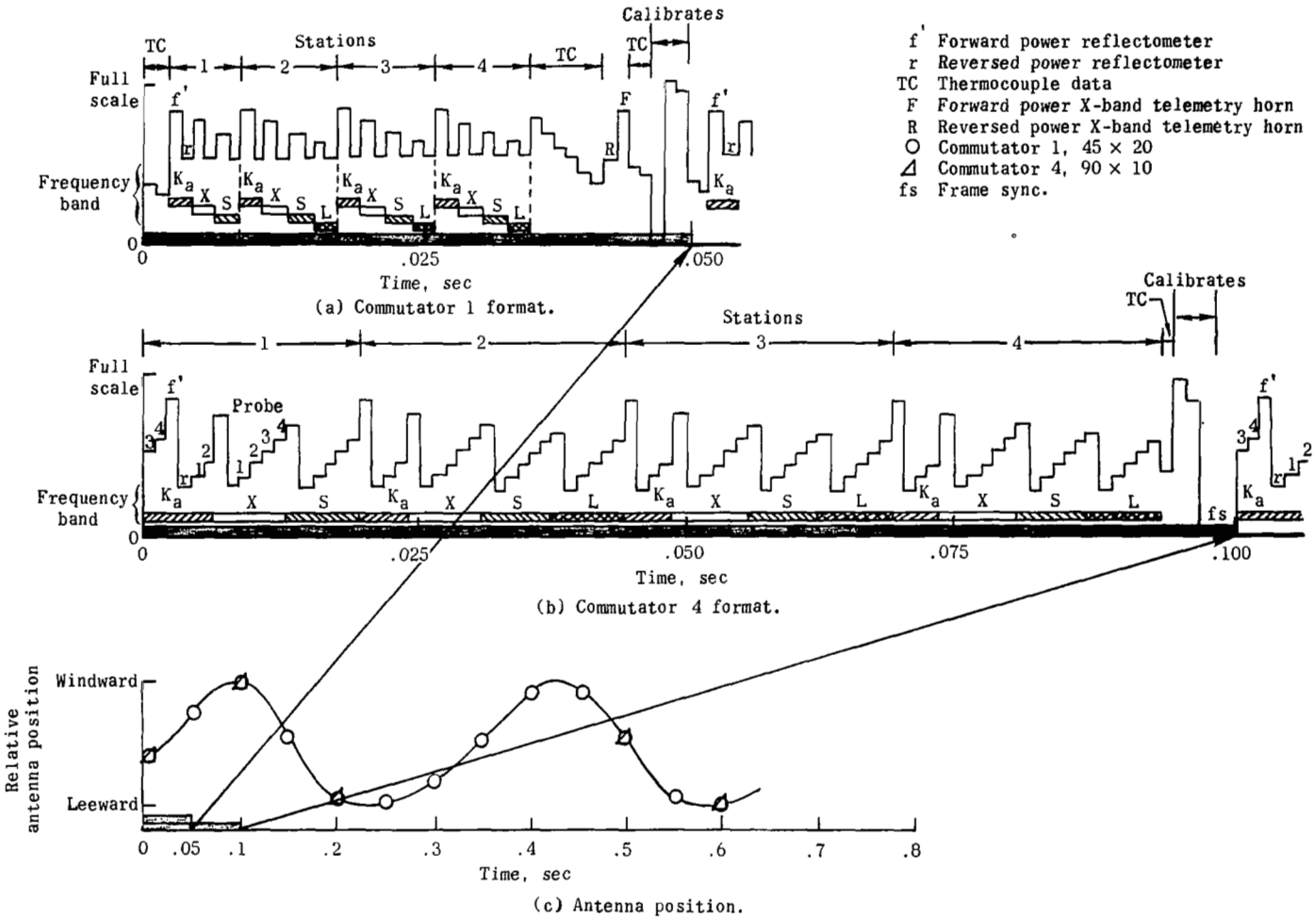

Figure 13.- Reflectometer data sampling rate compared with windward and leeward plasma variations. (One frame shown for each commutator.)

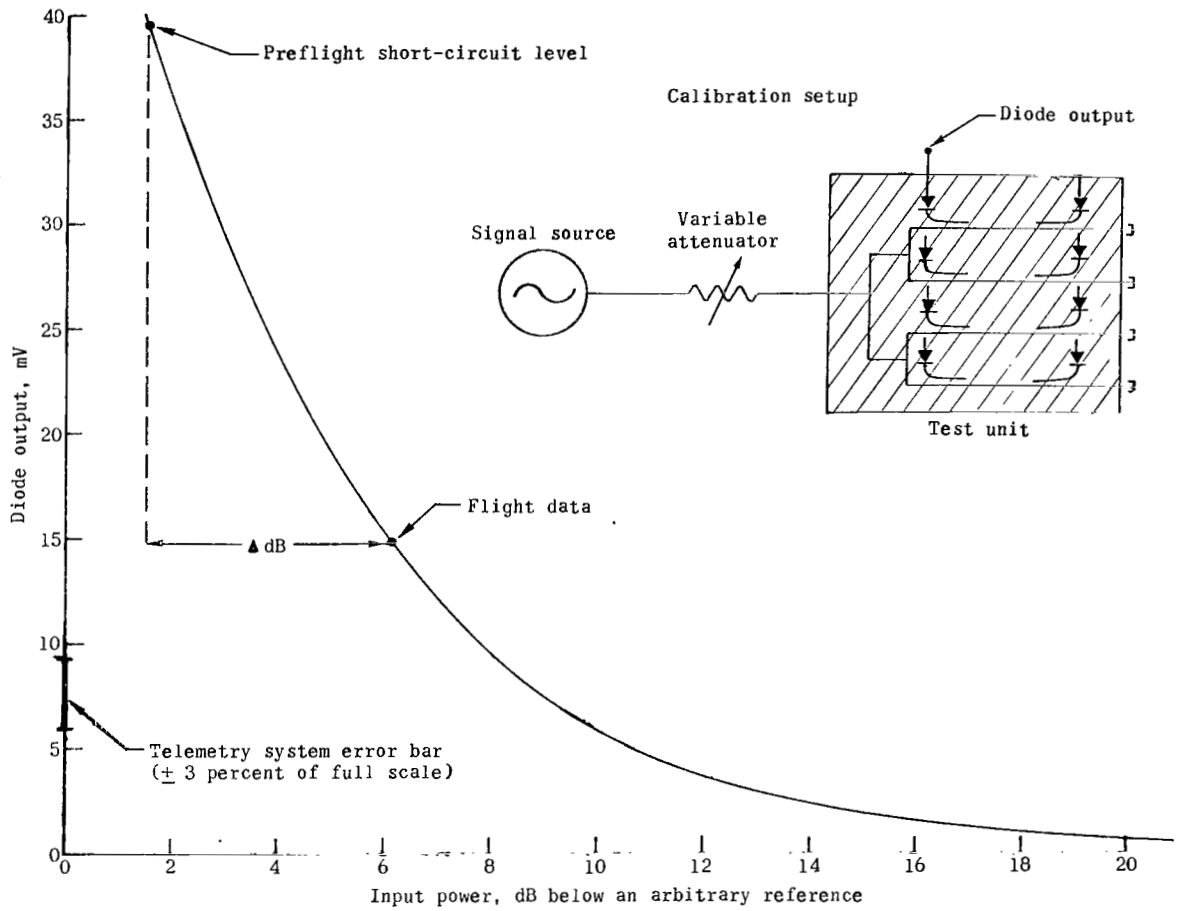

Figure 14.- Diode calibration curve for S-band reflected signal (typical) at station 1. $\Gamma_p = 10^{-\frac{\Delta dB}{10}}$.

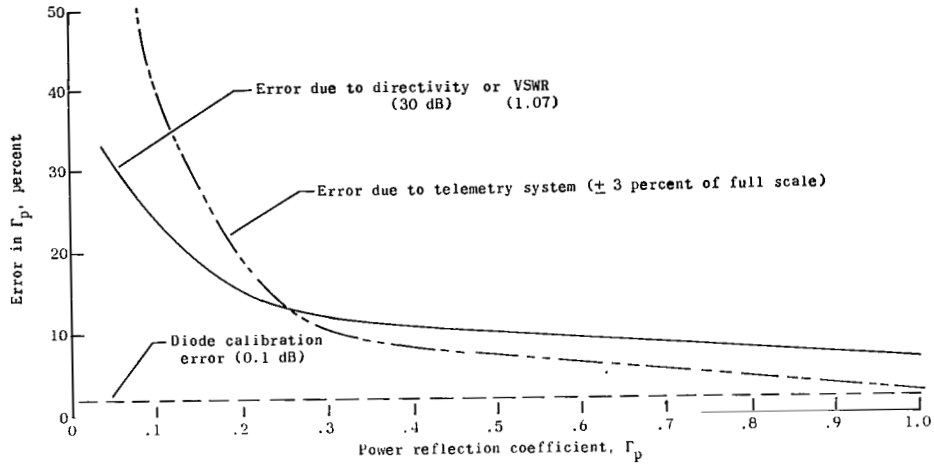

(a) Measured error in reflection coefficient.

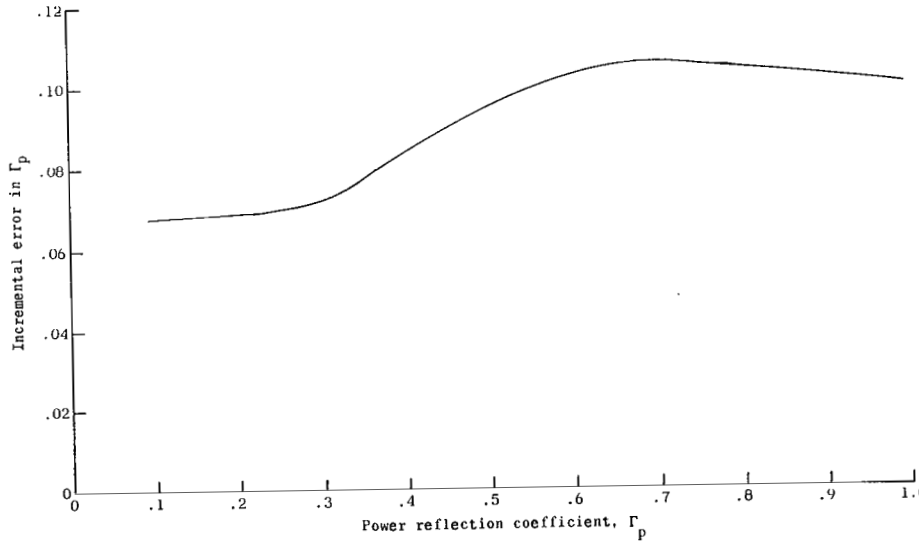

(b) Incremental error in reflection coefficient.

Figure 15.- Reflection-coefficient errors.

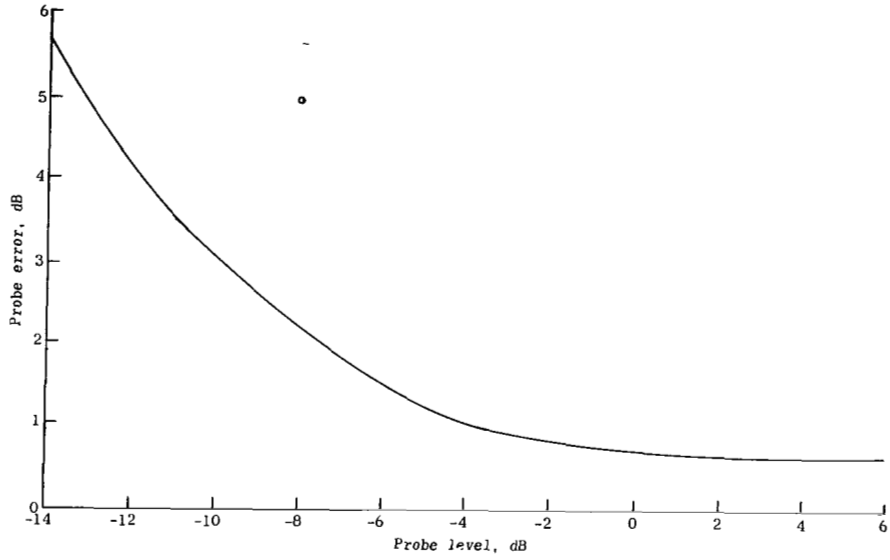

(a) Error in probe level.

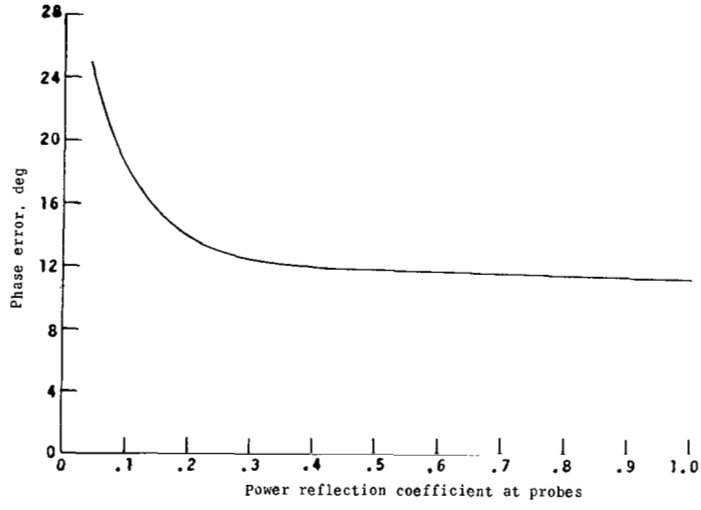

(b) Phase measurement error.

Figure 16.- Four-probe measurement errors for S-band at station 1. Probe 1; reference level error, 0.1 dB; diode calibration error, 0.1 dB; telemetry error, ±3 percent of full scale.

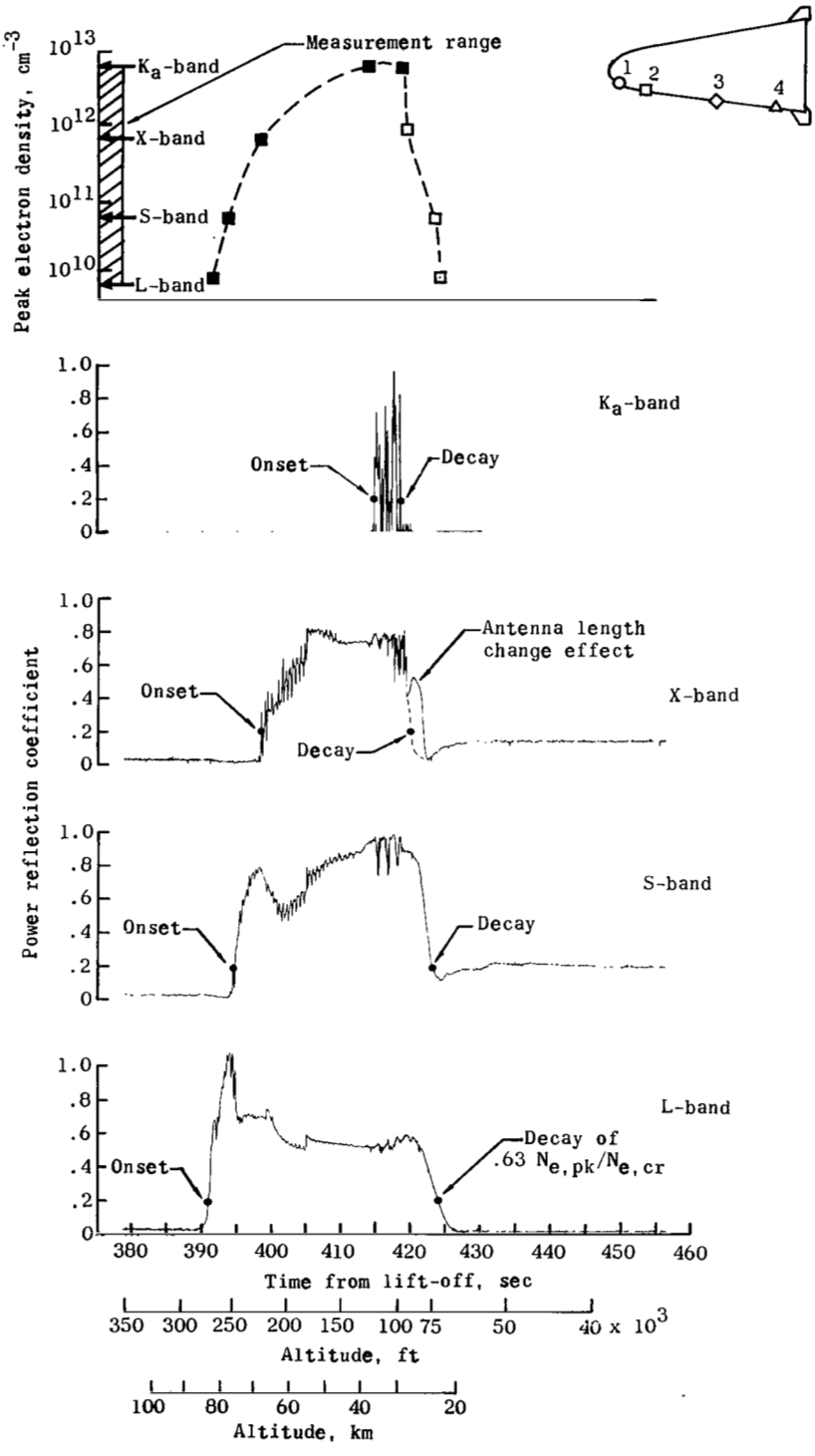

Figure 17.- Electron density determined from reflectometer data at station 2. Data noted by open symbols subject to errors (see p. 11 of text).

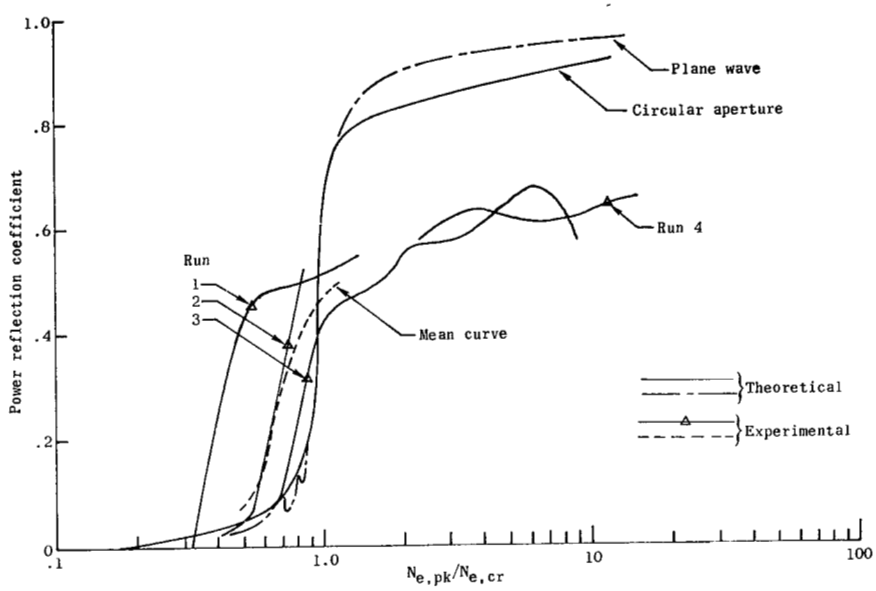

(a) Magnitude.

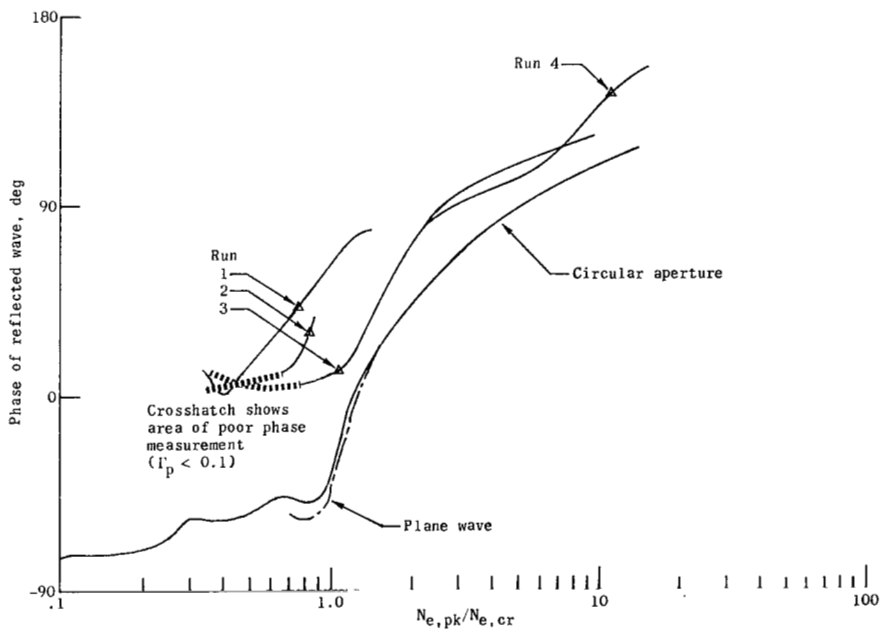

(b) Phase.

Figure 18.- Measured (ref. 19) and computed reflection coefficients for the X-band flight conical horn in a shock tube. Radius, 2.527 cm (X-band conical horn, stations 2, 3, and 4); frequency, 10.044 MHz; total plasma thickness, 15.24 cm; parabolic plasma profile (ref. 16), half density thickness, 0.234 cm; $\nu = 2.51 \times 10^9$.

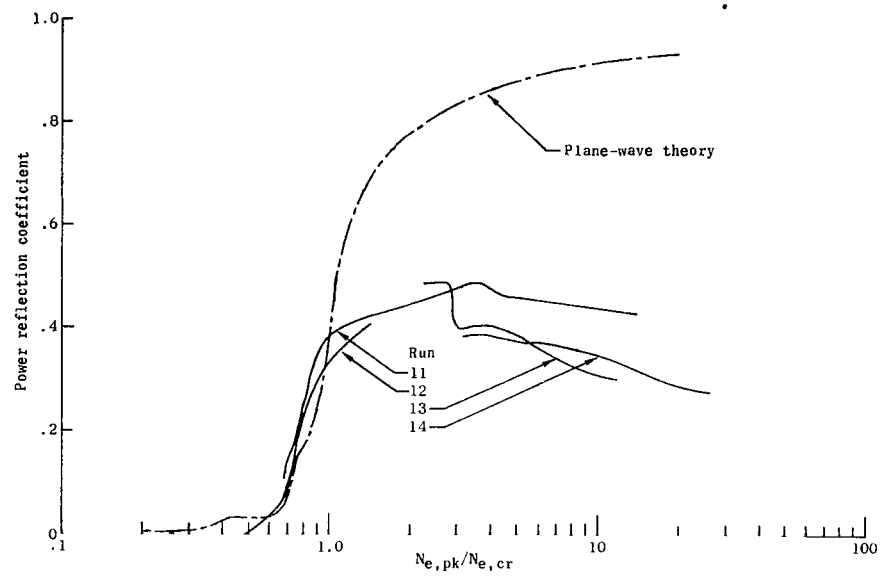

(a) Magnitude.

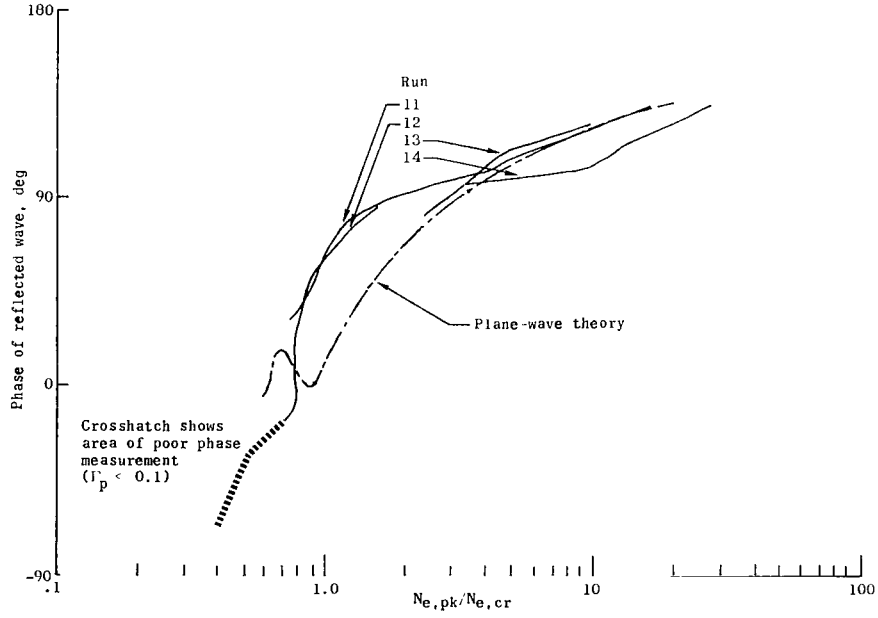

(b) Phase

Figure 19.- Measured (ref. 19) and computed reflection coefficients for the S-band flight open-end waveguide.

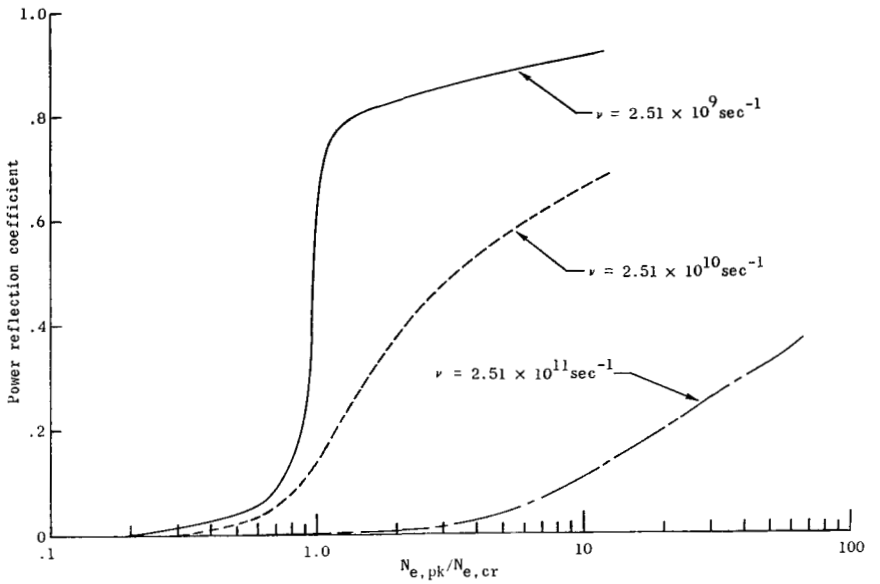

(a) Magnitude.

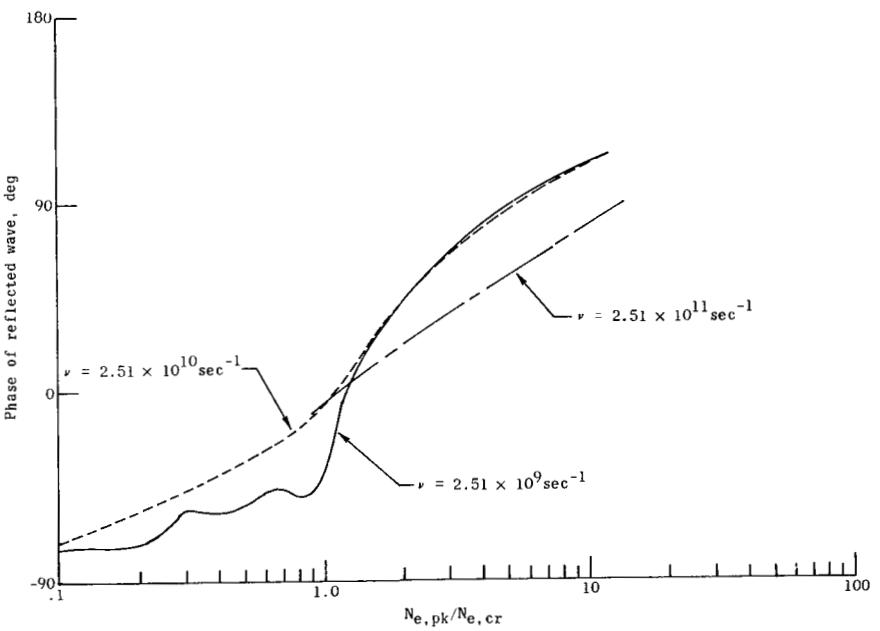

(b) Phase.

Figure 20.- Computed collision-frequency effect on circular-aperture reflection coefficient. Radius, 2.527 cm (X-band conical horn, stations 2, 3, and 4); frequency, 10.044 MHz; total plasma thickness, 15.24 cm; parabolic plasma profile (ref. 16), half density thickness, 0.234 cm.

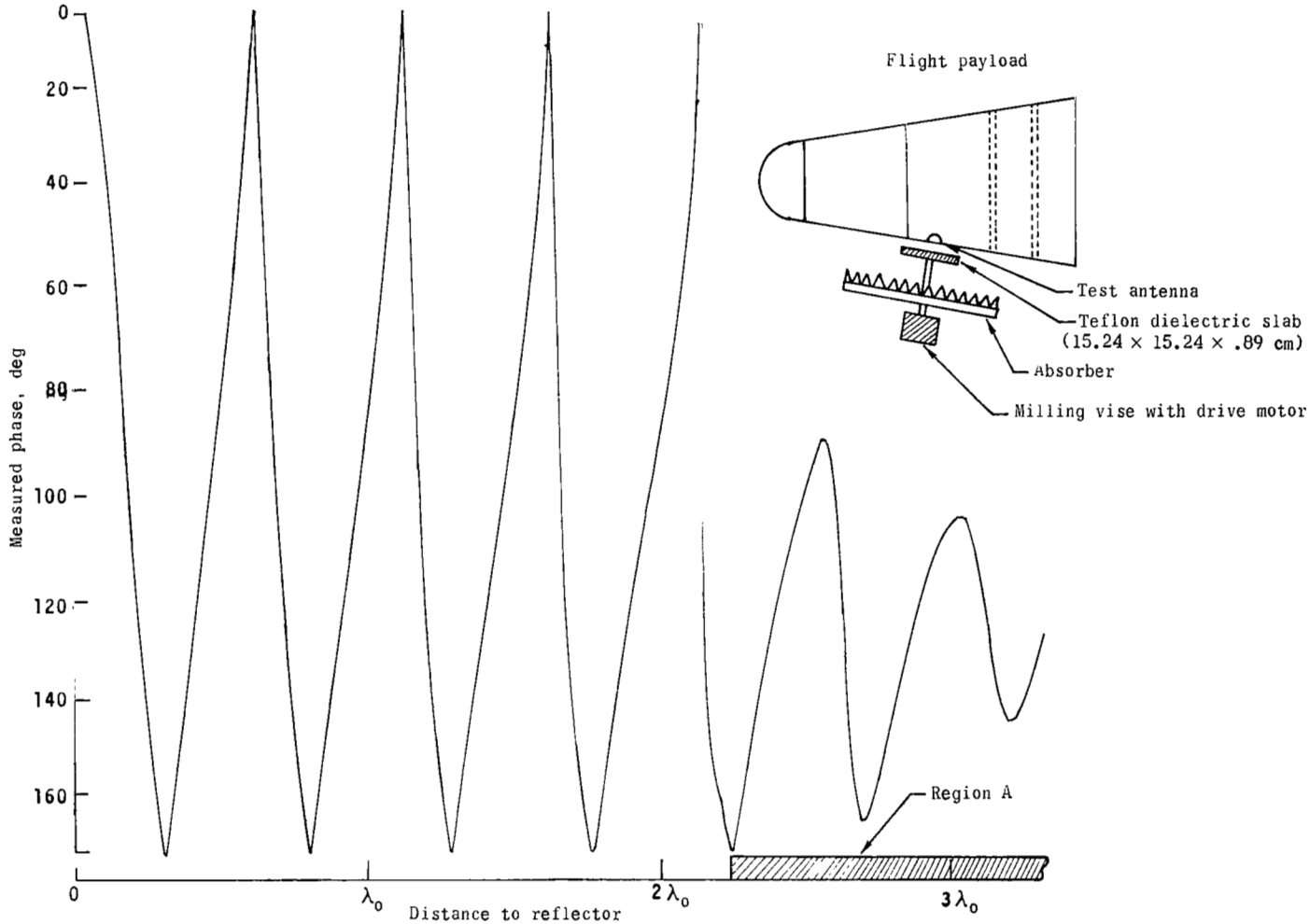

Figure 21.- Variation of phase with reflector distance for X-band station 3 conical horn.

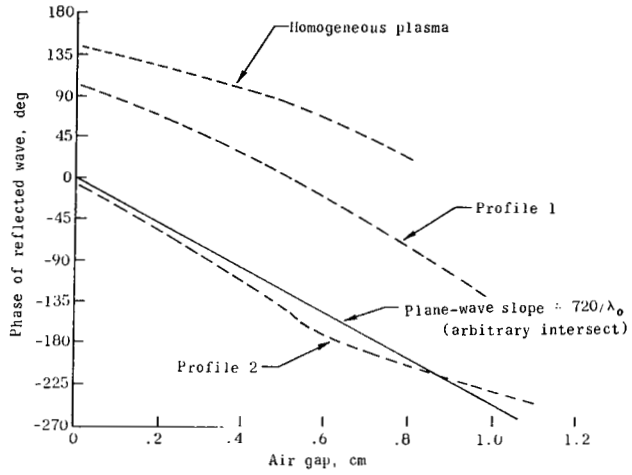

(a) Phase coefficients. $N_{e,pk}/N_{e,cr} = 10$; $\nu = 10^9$ sec^{-1}, aperture radius, 1.2 cm.

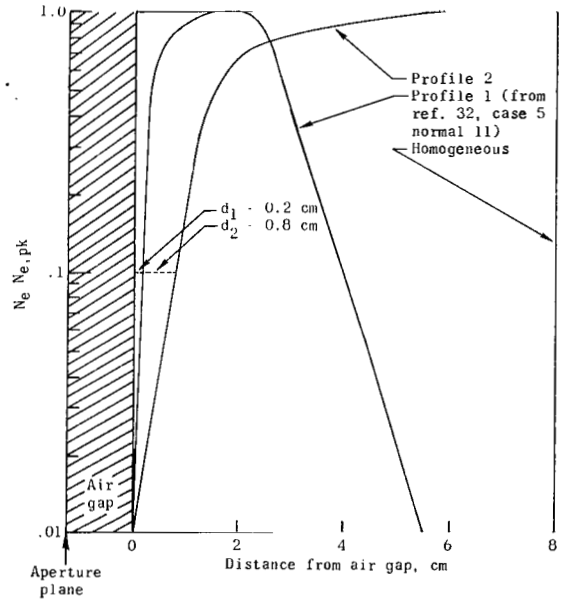

(b) Electron-density profiles.

Figure 22.- Computed aperture phase coefficients for three given plasma profiles.

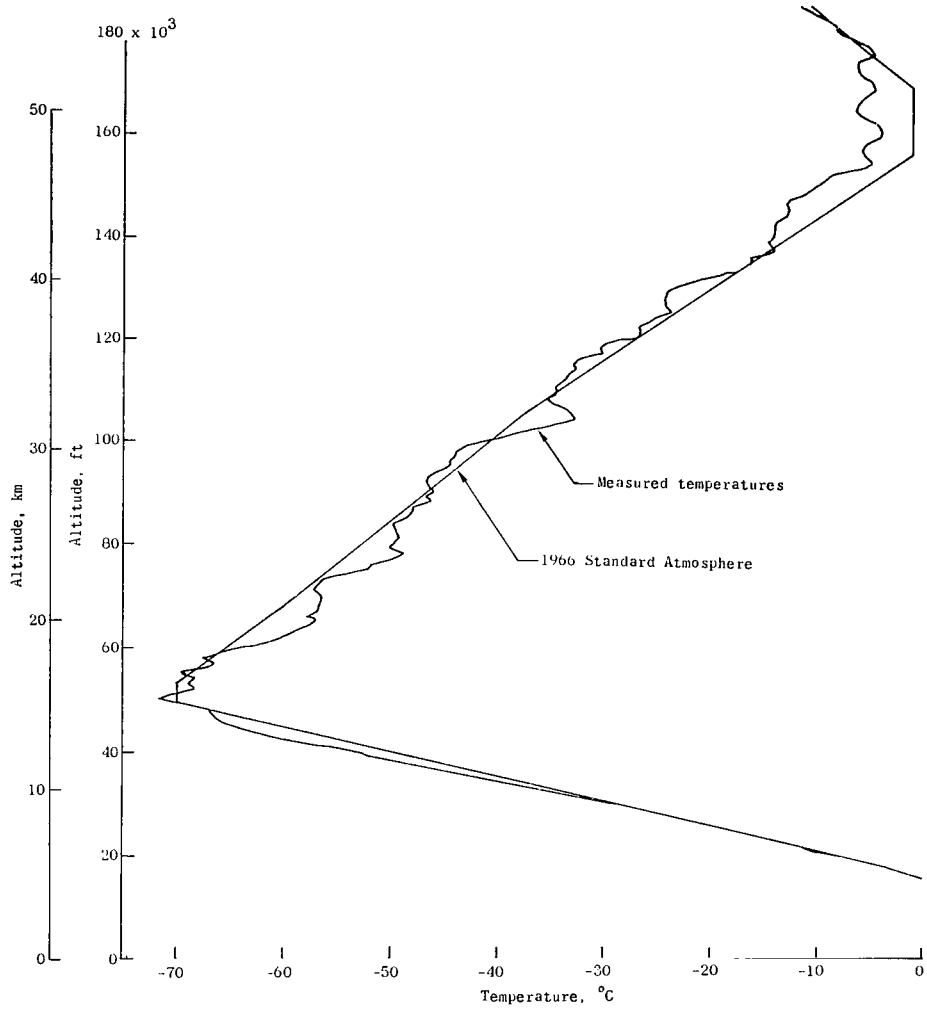

(a) Measured temperature.

Figure 23.- Bermuda radiosonde data compared with 1966 Standard Atmosphere at latitude 30° N. for July.

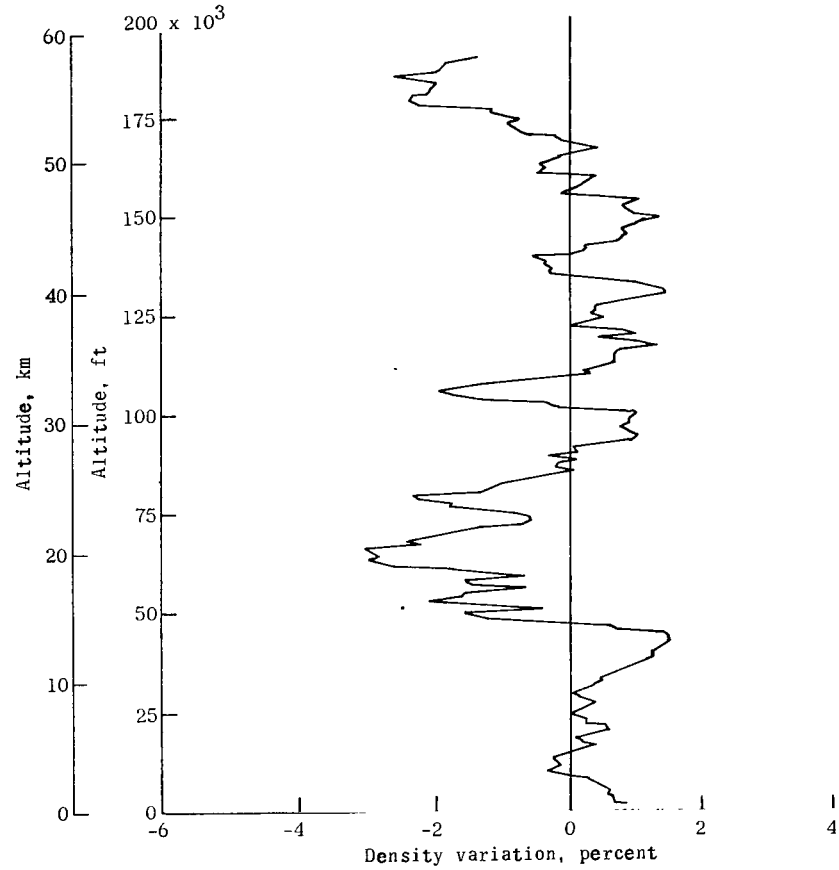

(b) Variations of density computed from temperature data.

Figure 23.- Concluded.

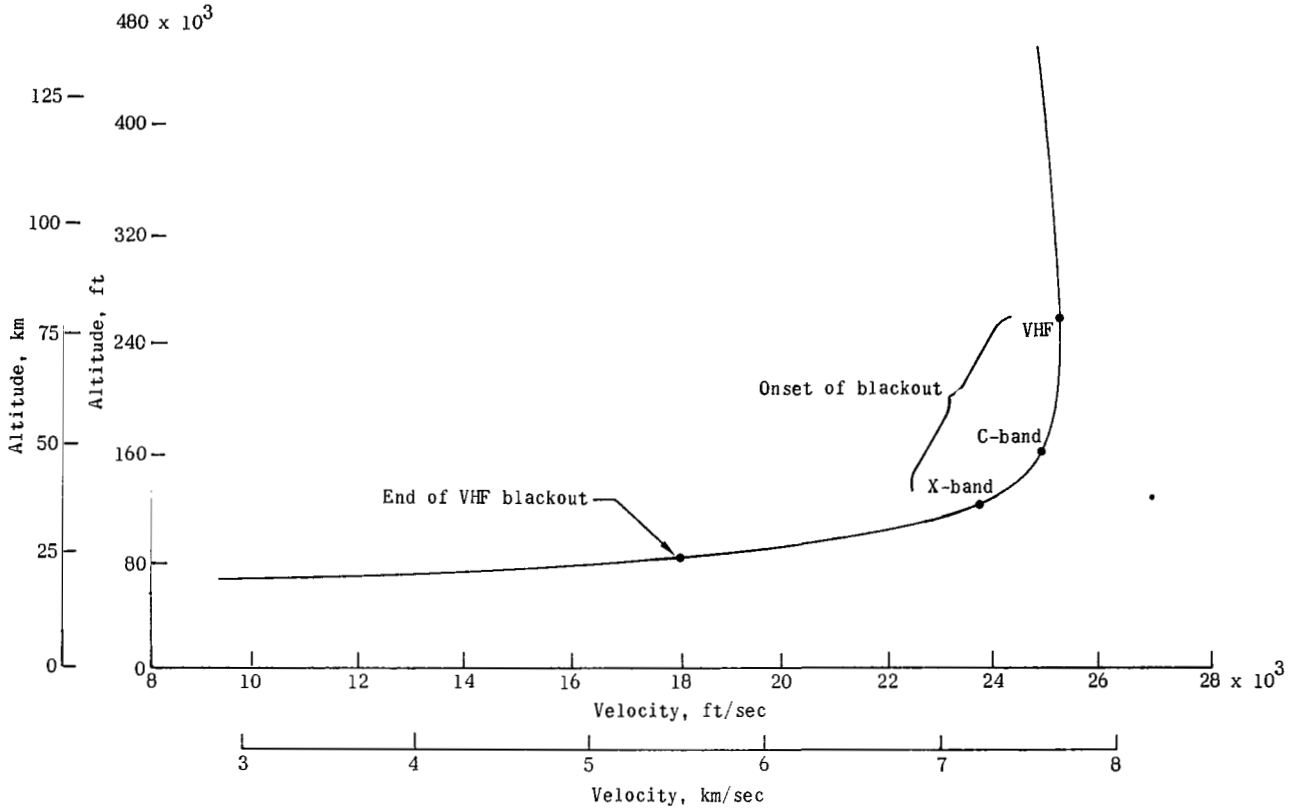

Figure 24.- RAM C-II reentry trajectory showing onset and end of RF signal blackout. X-band and C-band reacquisition was delayed due to tracking difficulties.

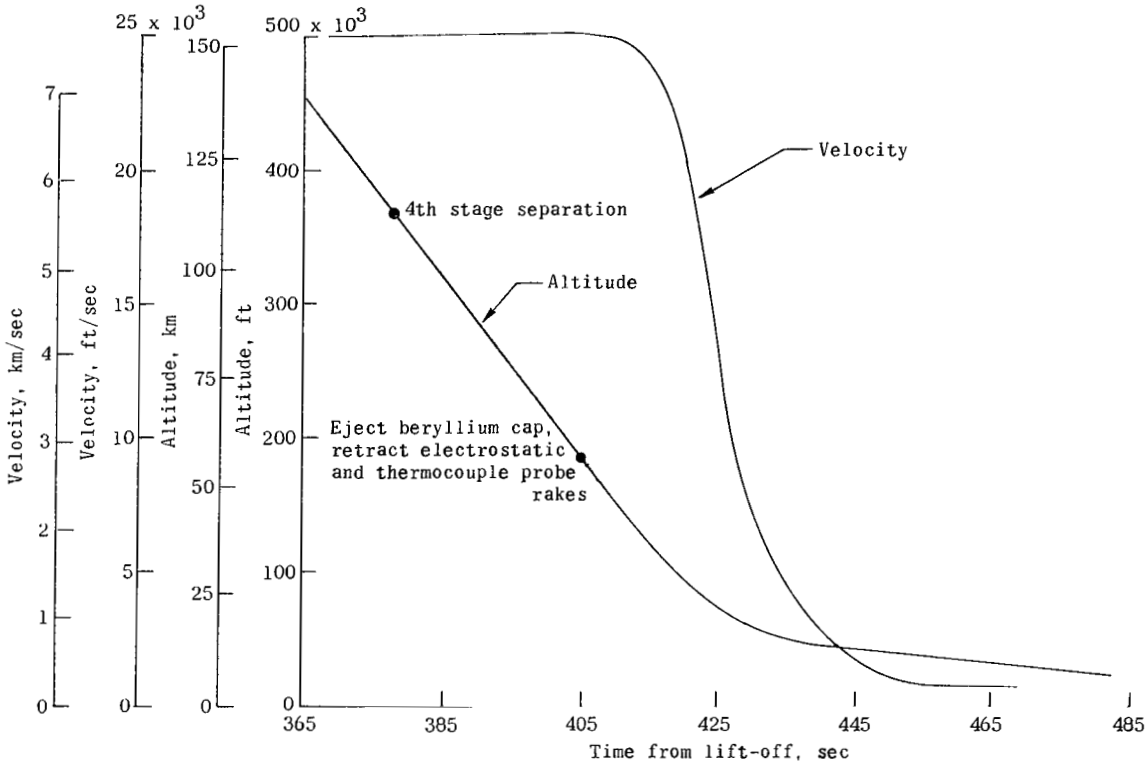

Figure 25.- RAM C-II reentry altitude and velocity time histories.

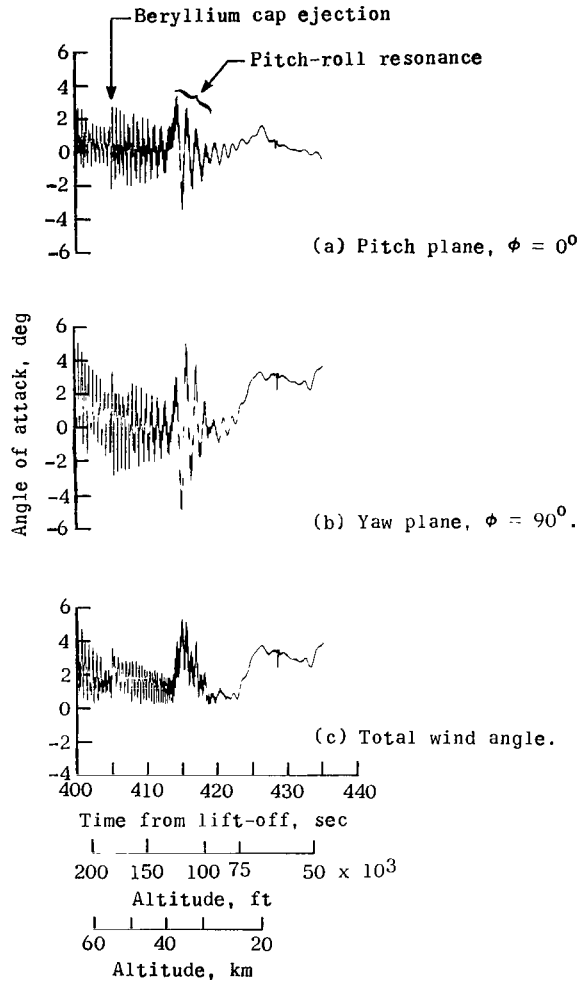

Figure 26.- Payload angle-of-attack time history.

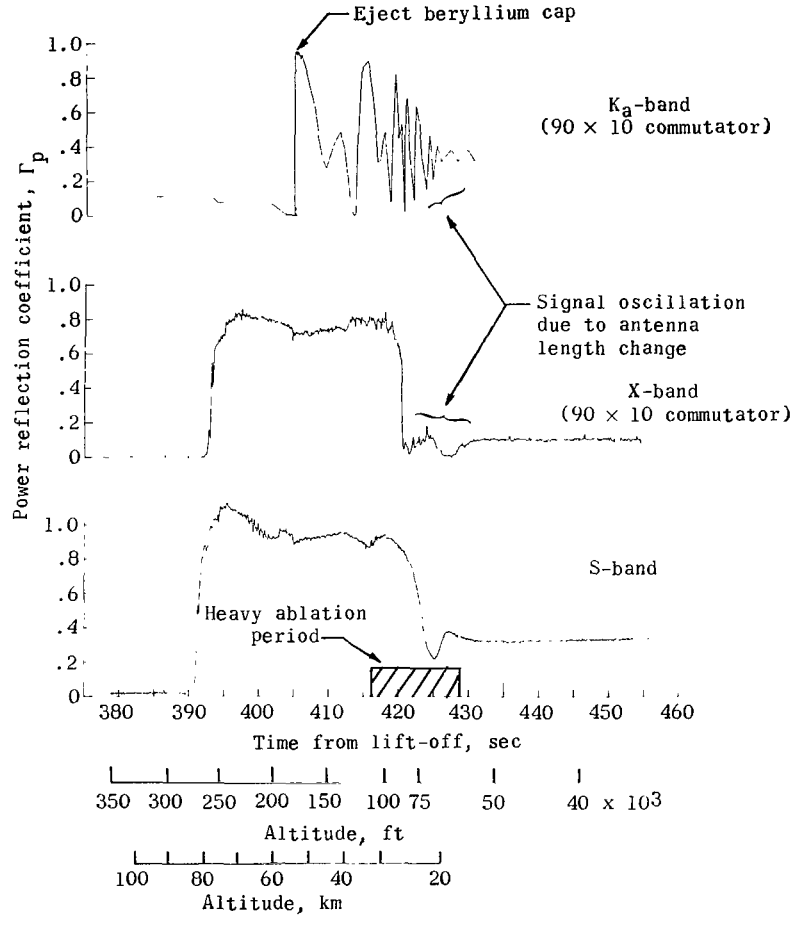

(a) Station 1 (x/D = 0.15). K_a-band is relative to maximum level during flight; figure 19 gives levels relative to the short-circuited aperture.

Figure 27.- Measured reflection coefficient magnitudes relative to short circuit at aperture with beryllium cap on.

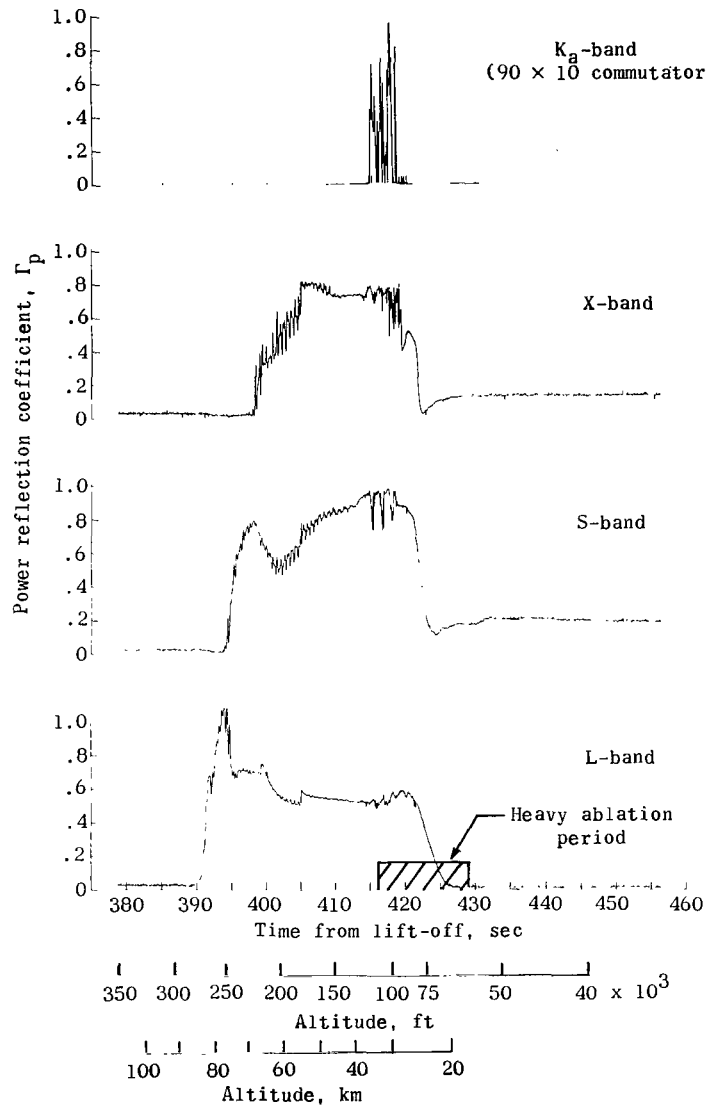

(b) Station 2 (x/D = 0.76).

Figure 27.- Continued.

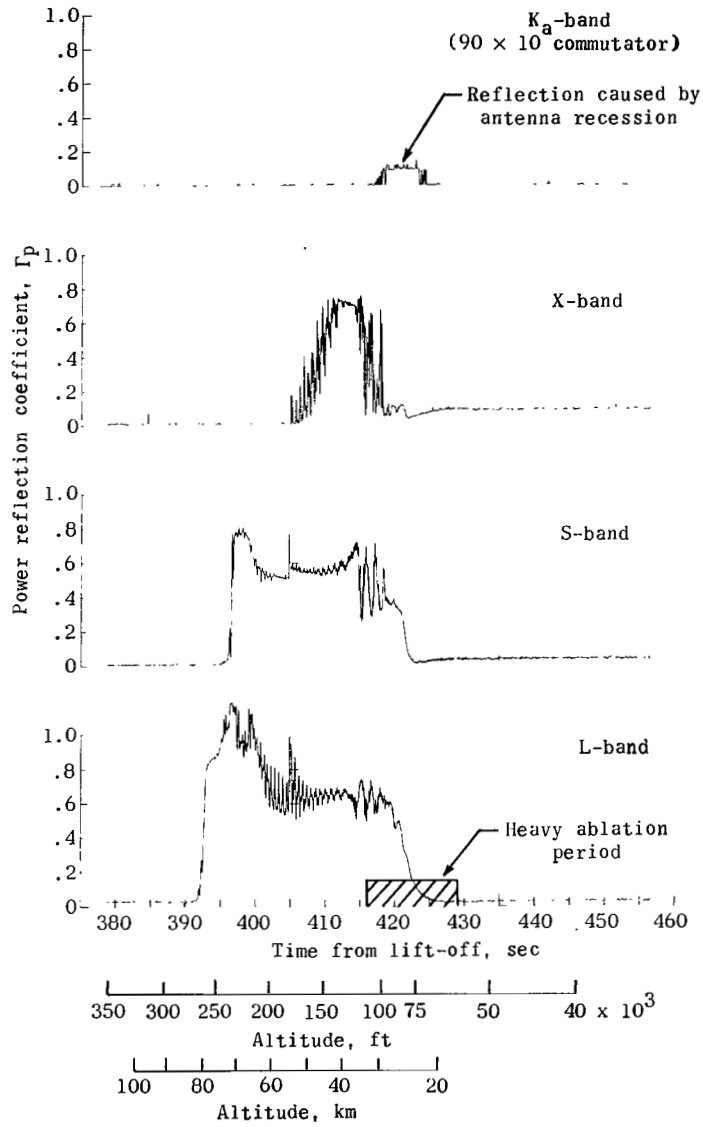

(c) Station 3 (x/D = 2.30).

Figure 27.- Continued.

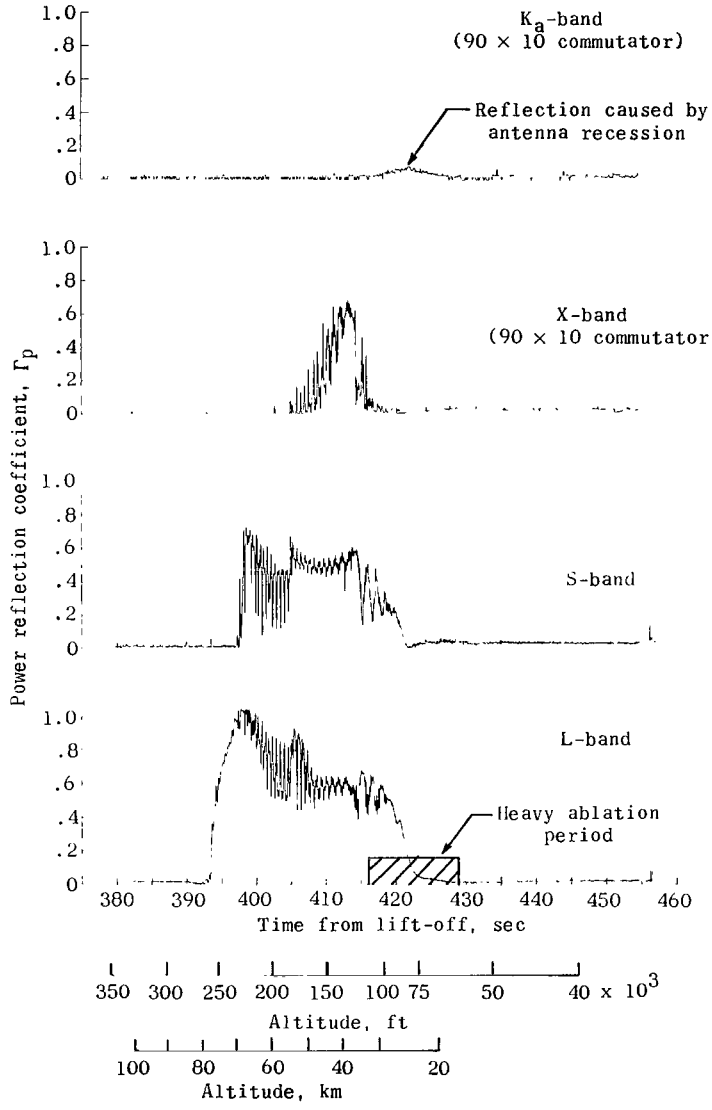

(d) Station 4 (x/D = 3.48).

Figure 27.- Concluded.

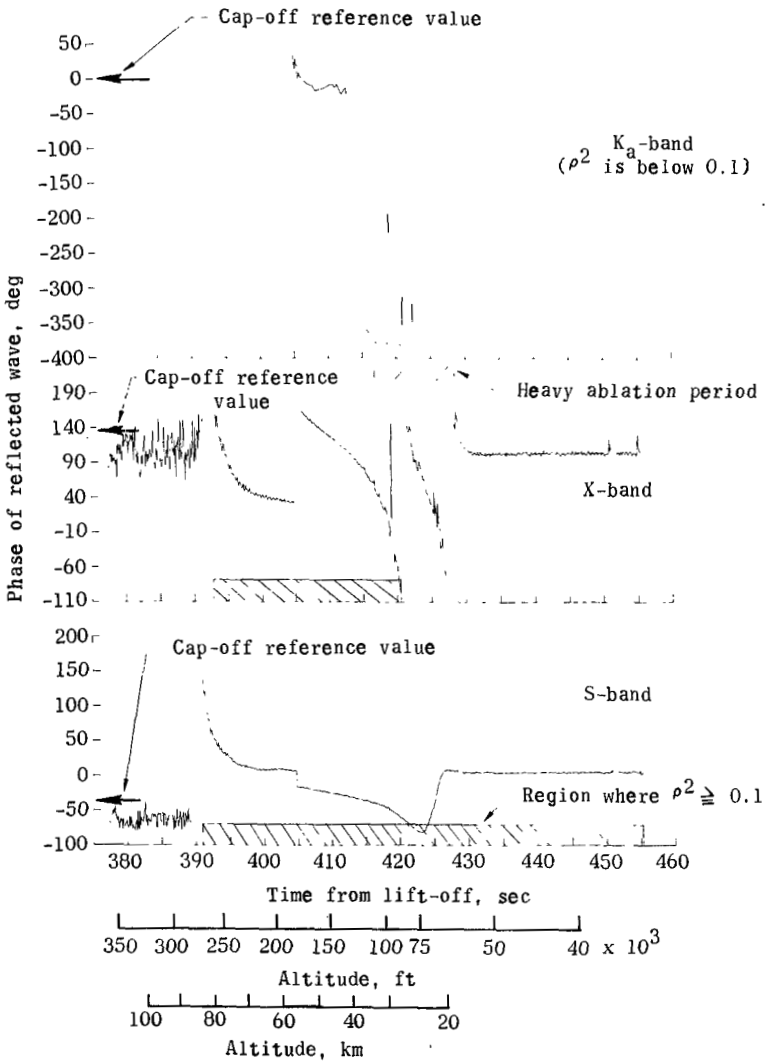

(a) Station 1 (x/D = 0.15).

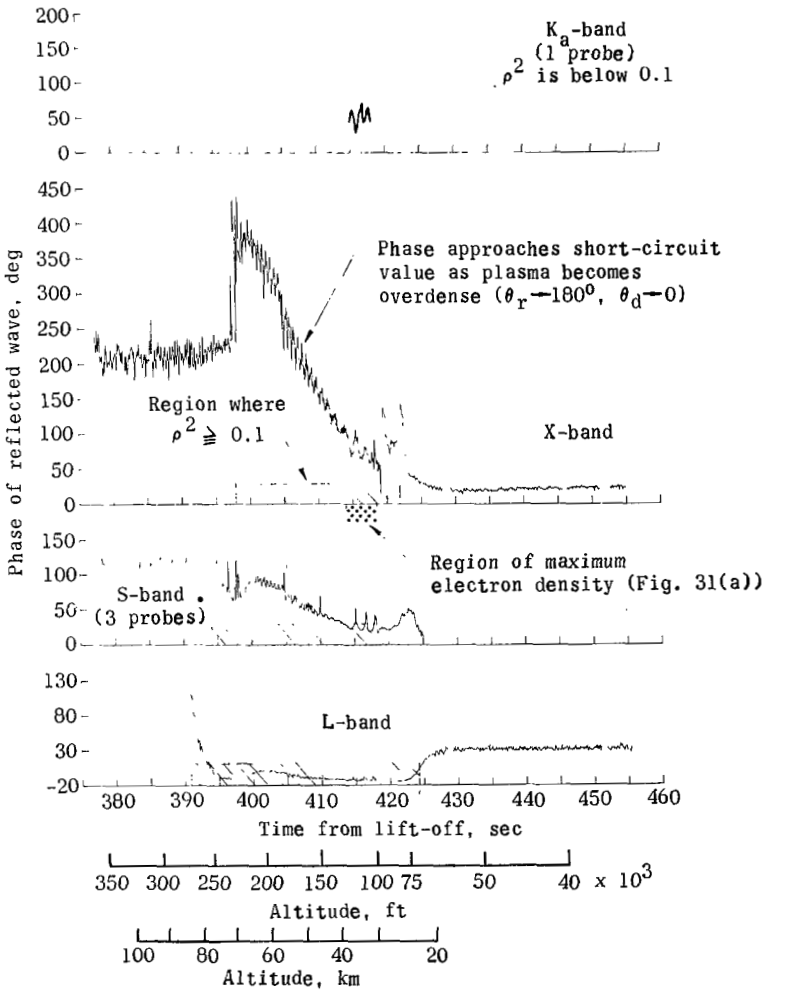

(b) Station 2 (x/D = 0.76).

Figure 28.- Measured phase coefficients relative to the short-circuited aperture with beryllium cap on.

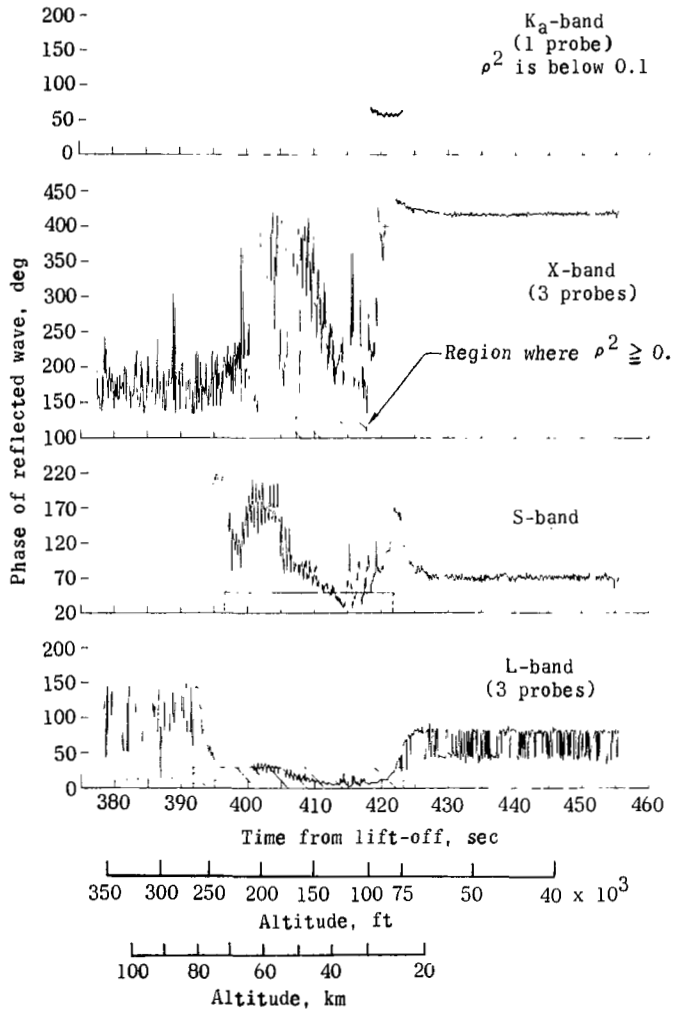

(c) Station 3 (x/D = 2.30).

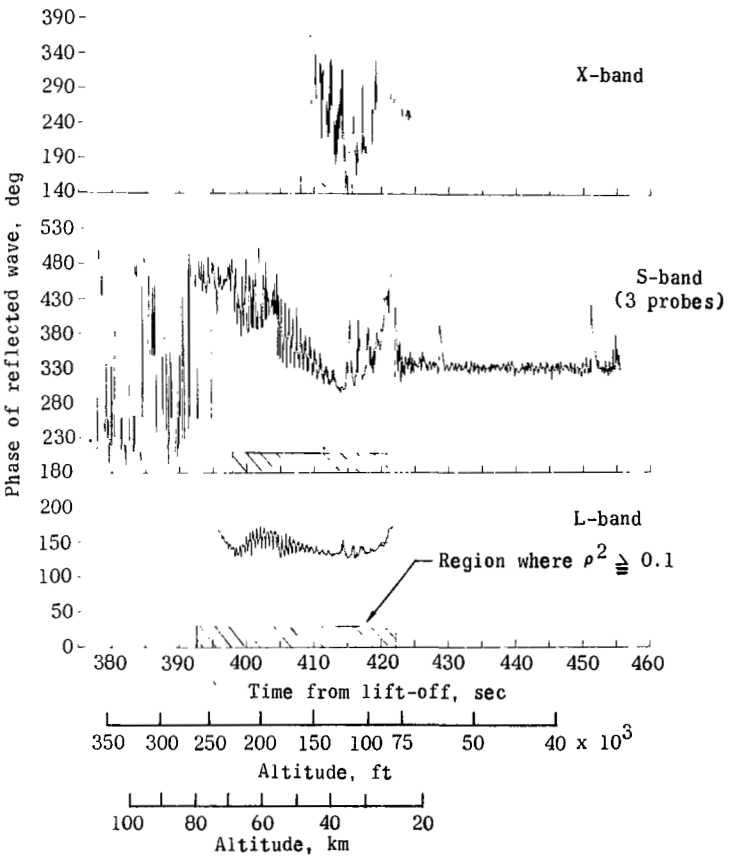

(d) Station 4 (x/D = 3.48).

Figure 28.- Concluded.

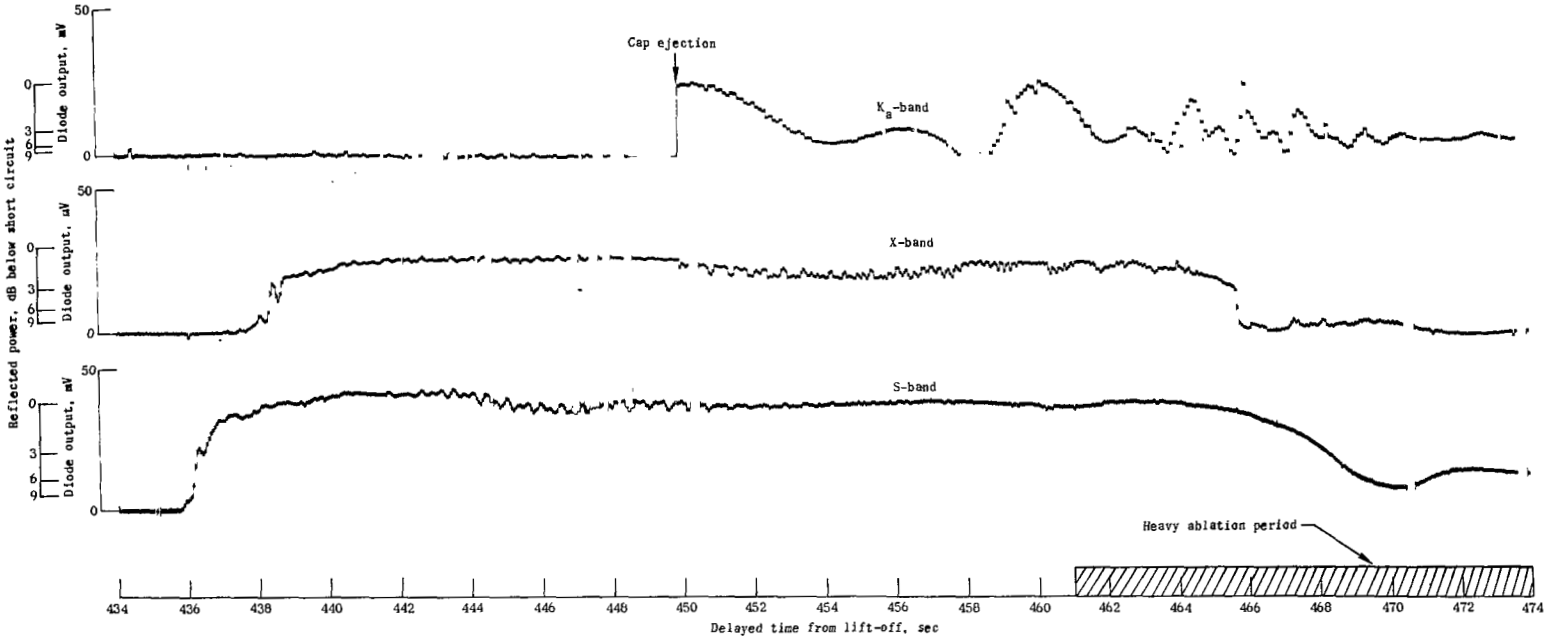

(a) Station 1 (x/D = 0.15).

Figure 29.- Reflectometer levels from reflected power detectors. All data are from the 45 × 20 commutator except K_a-band data.

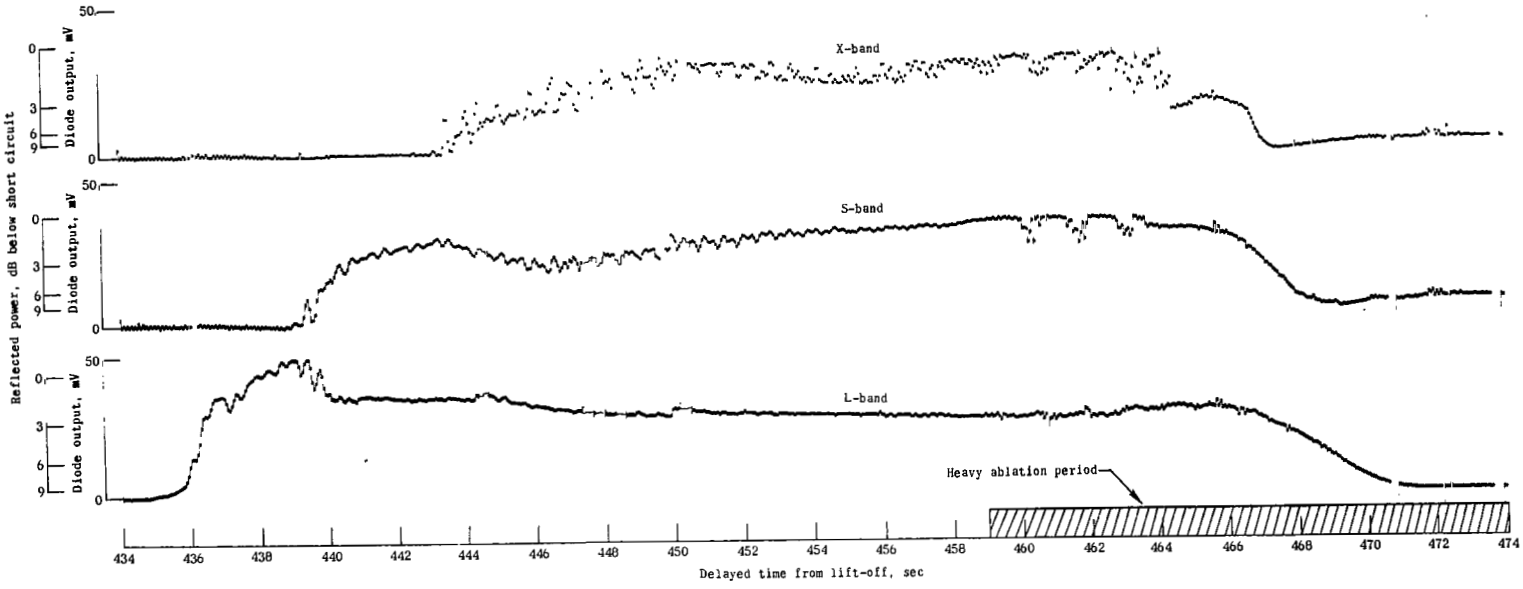

(b) Station 2 (x/D = 0.76).

Figure 29.- Continued.

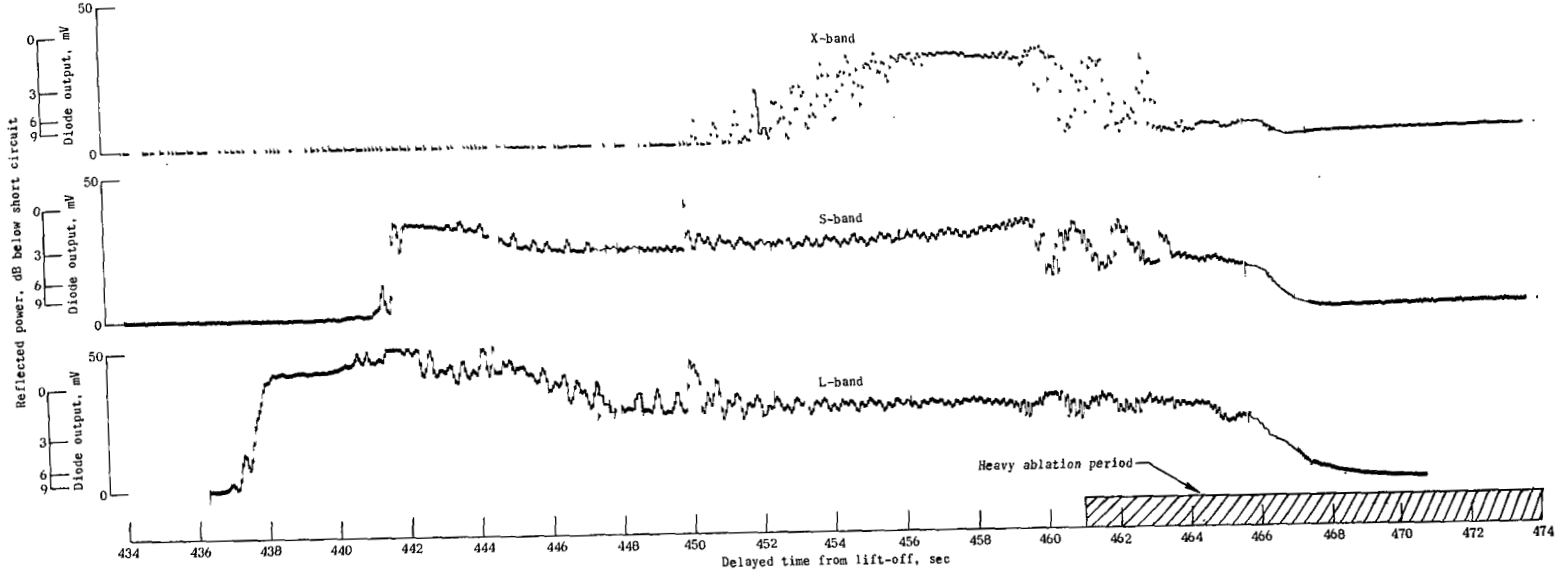

(c) Station 3 (x/D = 2.30).

Figure 29.- Continued.

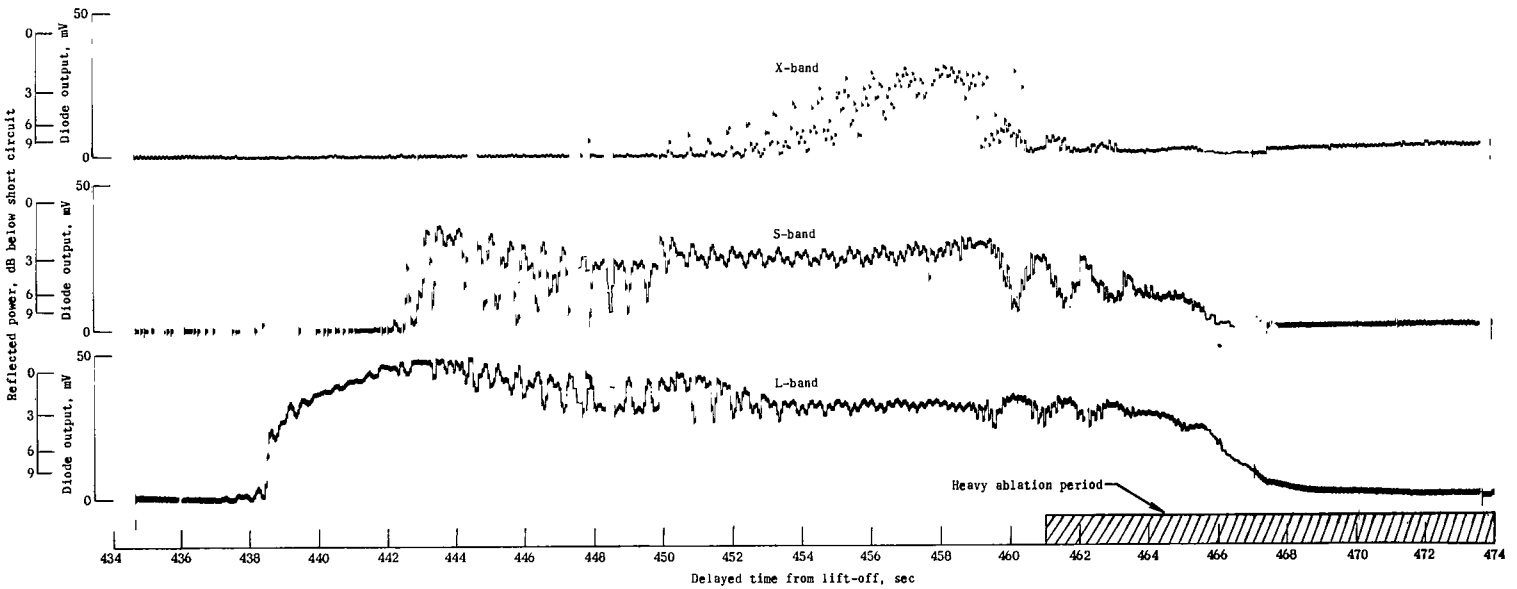

(d) Station 4 (x/D = 3.48).

Figure 29.- Concluded.

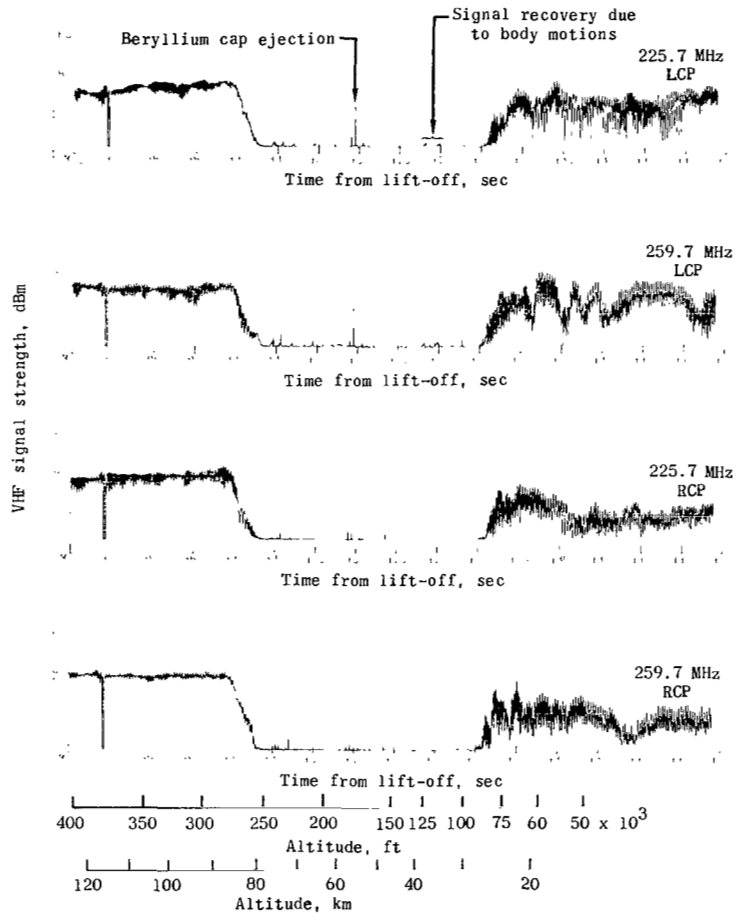

Figure 30.- VHF signal strength at USNS Range Recoverer. Left- and right-hand circular polarization (LCP and RCP).

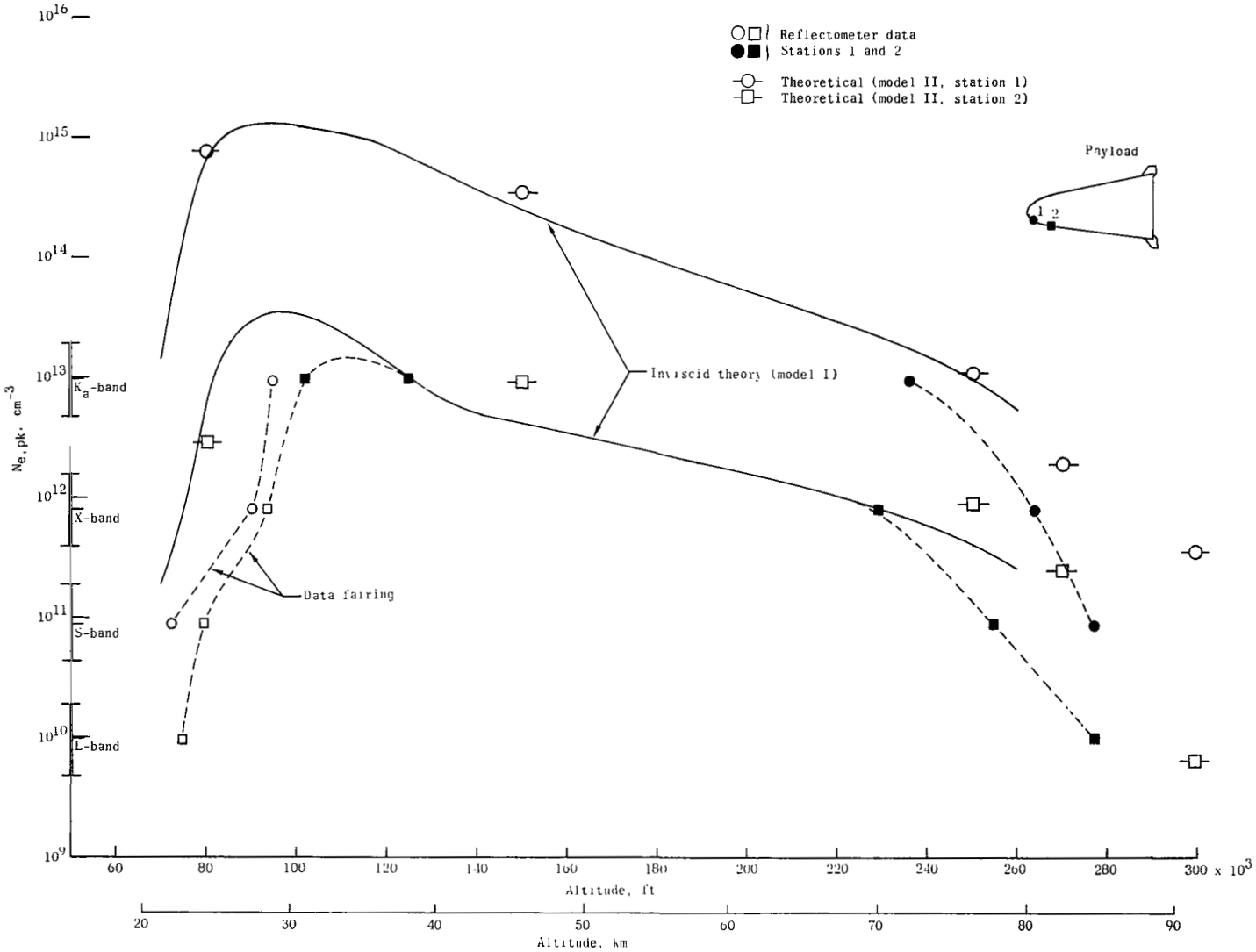

(a) Stations 1 and 2.

Figure 31.- Measured and calculated electron density. Open symbols data subject to errors (see text).

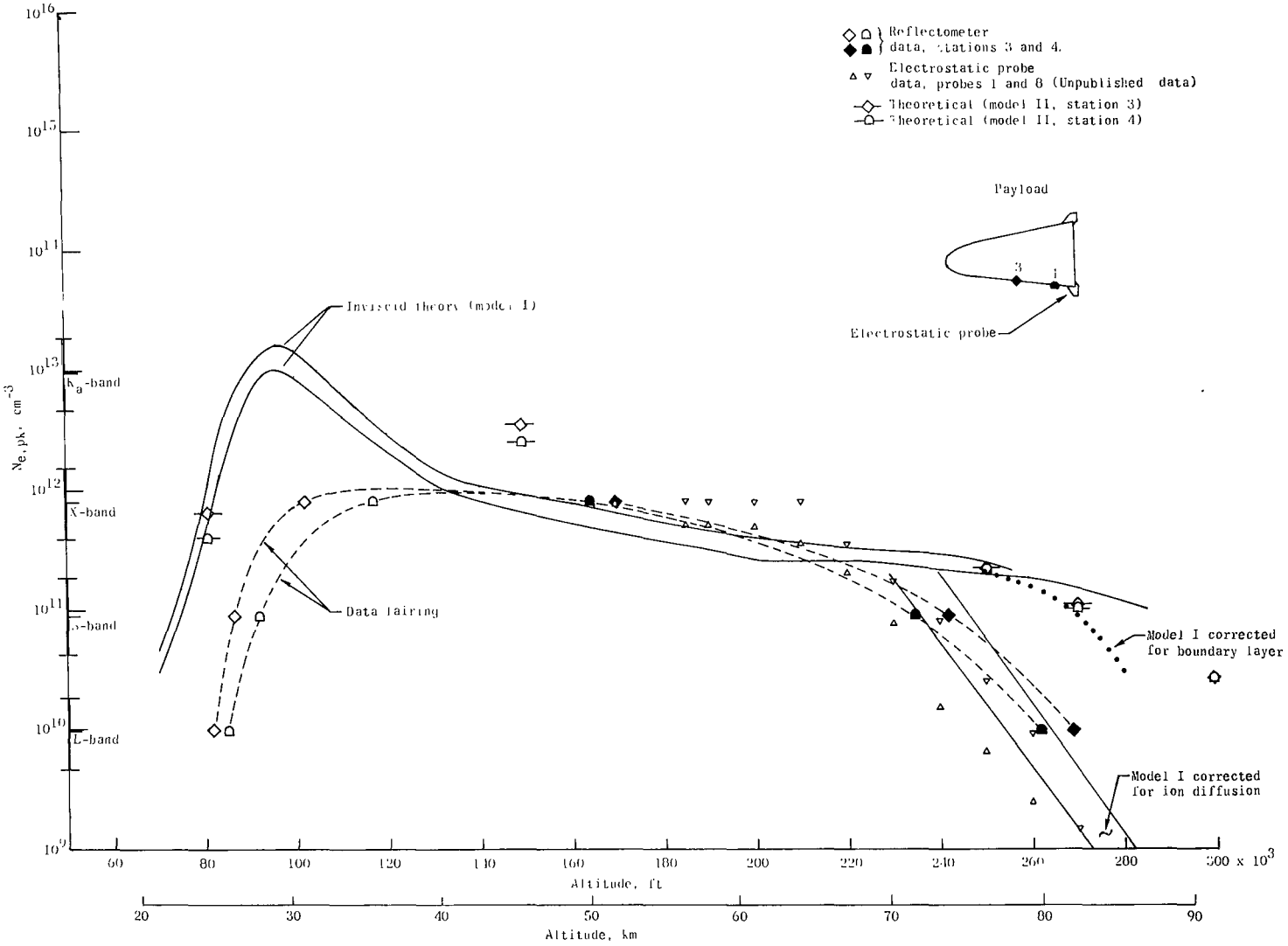

(b) Stations 3 and 4. (Unpublished data were obtained from L. W. Jones, Jr., and A. E. Cross of Langley Research Center.)

Figure 31.- Concluded.

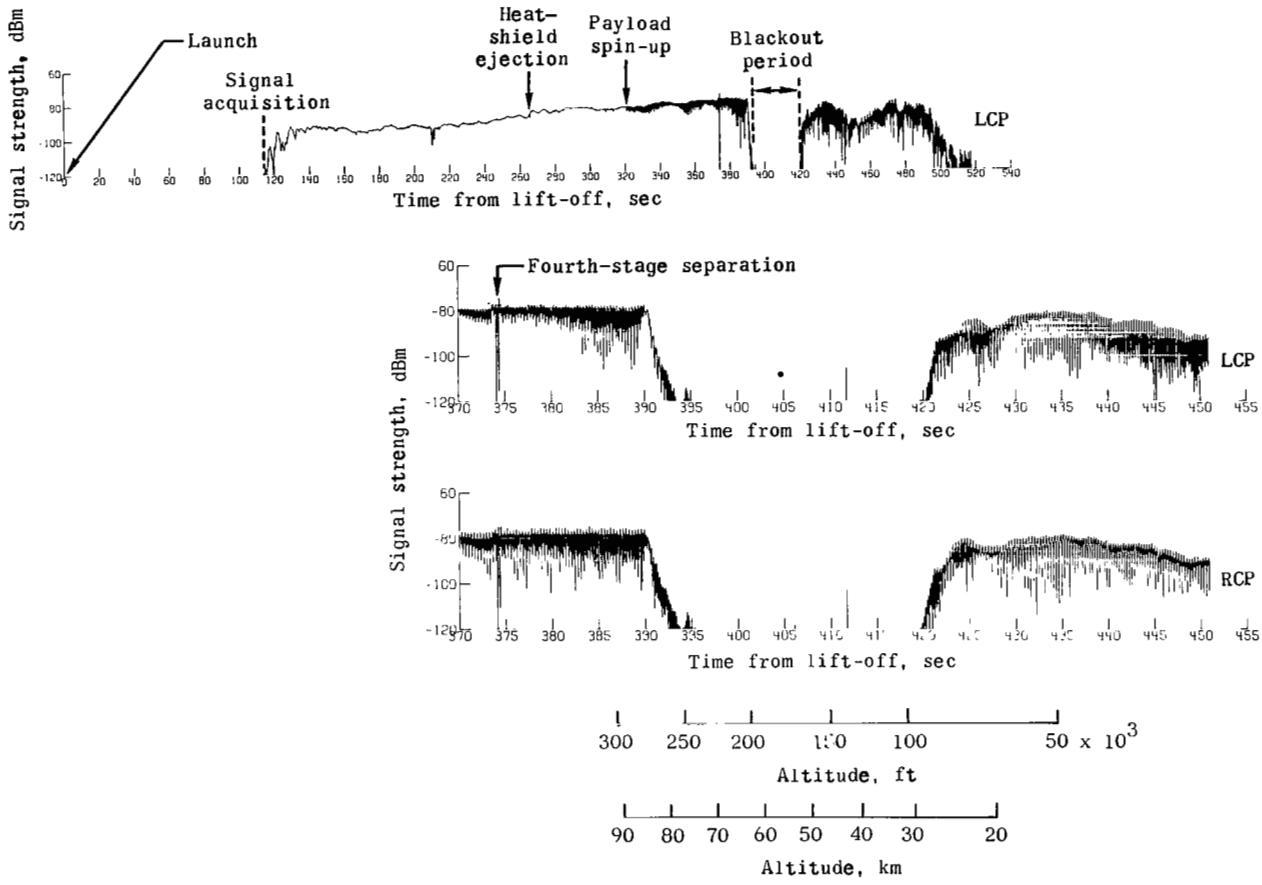

(a) RAM C-II 225.7 MHz ring antenna at x/D = 3.76.

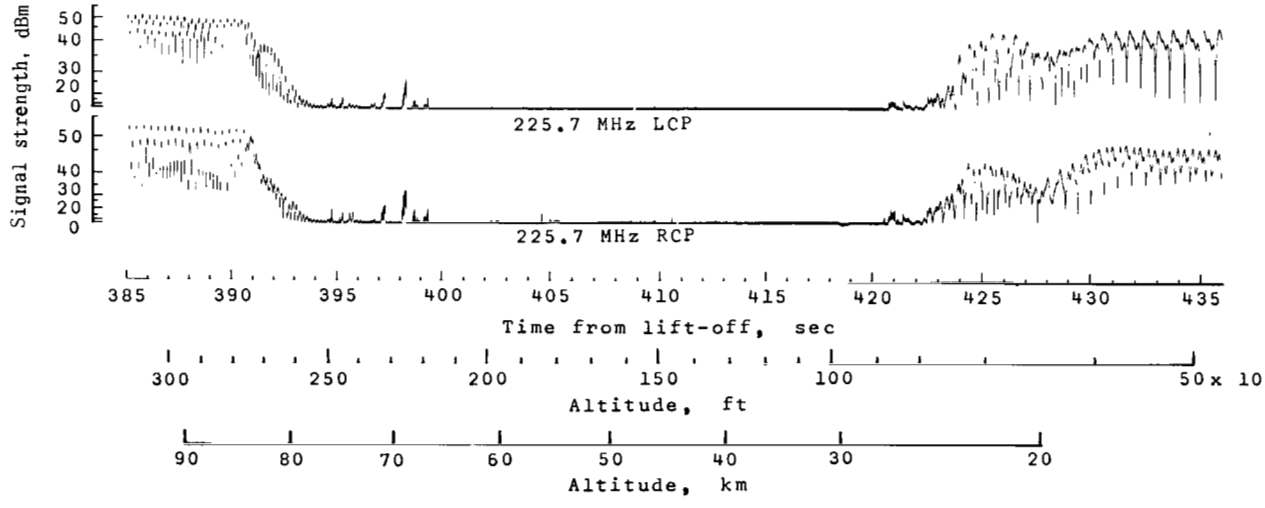

(b) RAM C-I 225.7 MHz ring antenna at x/D = 3.42.

Figure 32.- Bermuda signal-strength measurements (VHF).

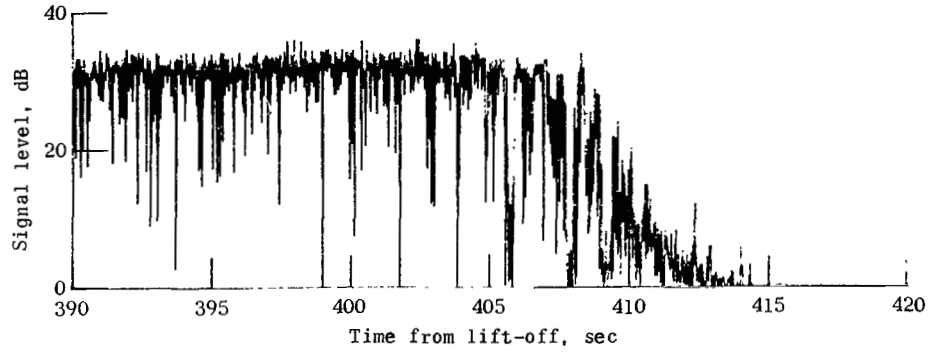

(a) RAM C-II.

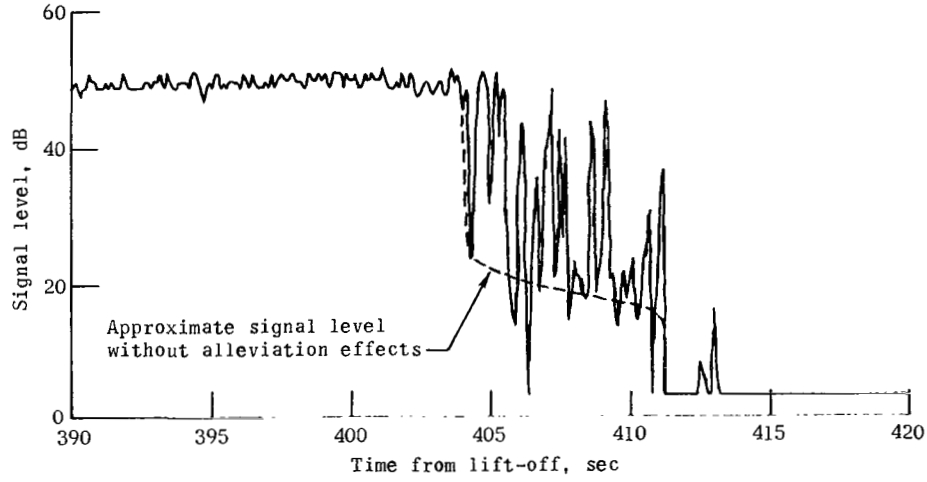

(b) RAM C-I. These data have been peak detected over 200 msec and have been corrected for range variations.

Figure 33.- RAM C-I and C-II X-band signal-strength measurements (horizontal polarization).

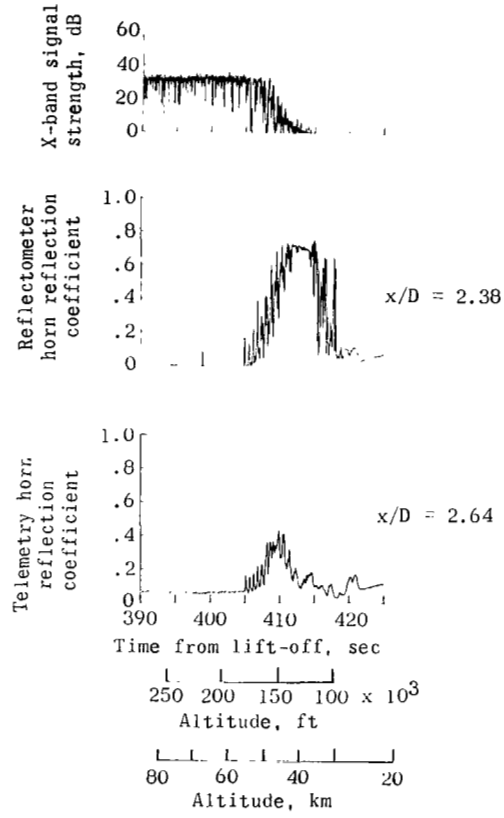

Figure 34.- RAM C-II X-band reflectometer horn and telemetry horn reflection-coefficient and signal-strength records (horizontal polarization).

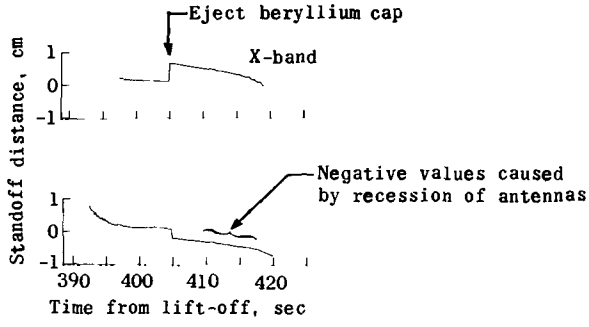

(a) Station 1 (x/D = 0.15).

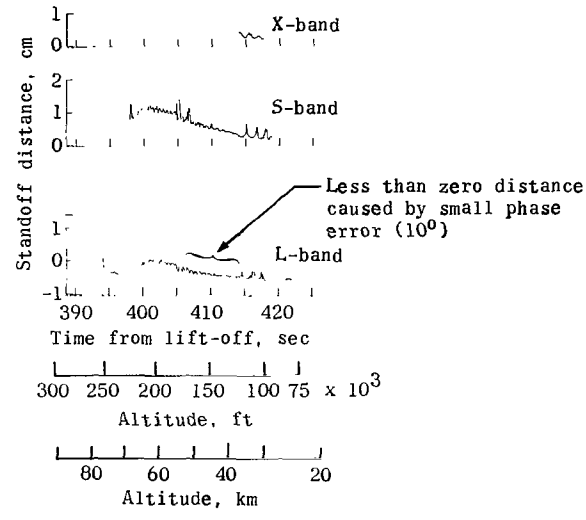

(b) Station 2 (x/D = 0.76).

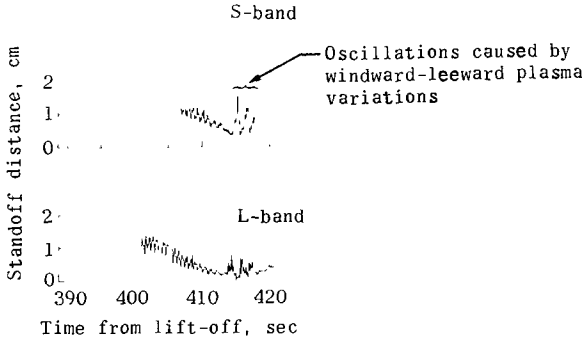

(c) Station 3 (x/D = 2.30).

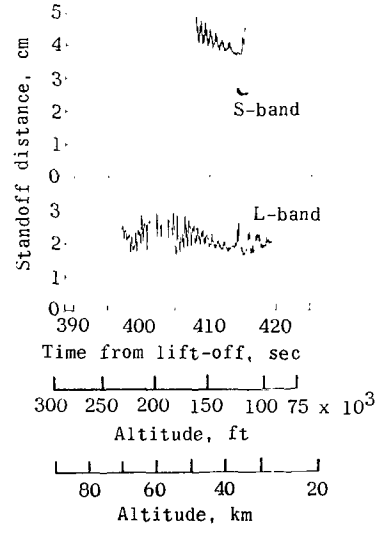

(d) Station 4 (x/D = 3.48).

Figure 35.- Reflectometer-determined critical density standoff distances.

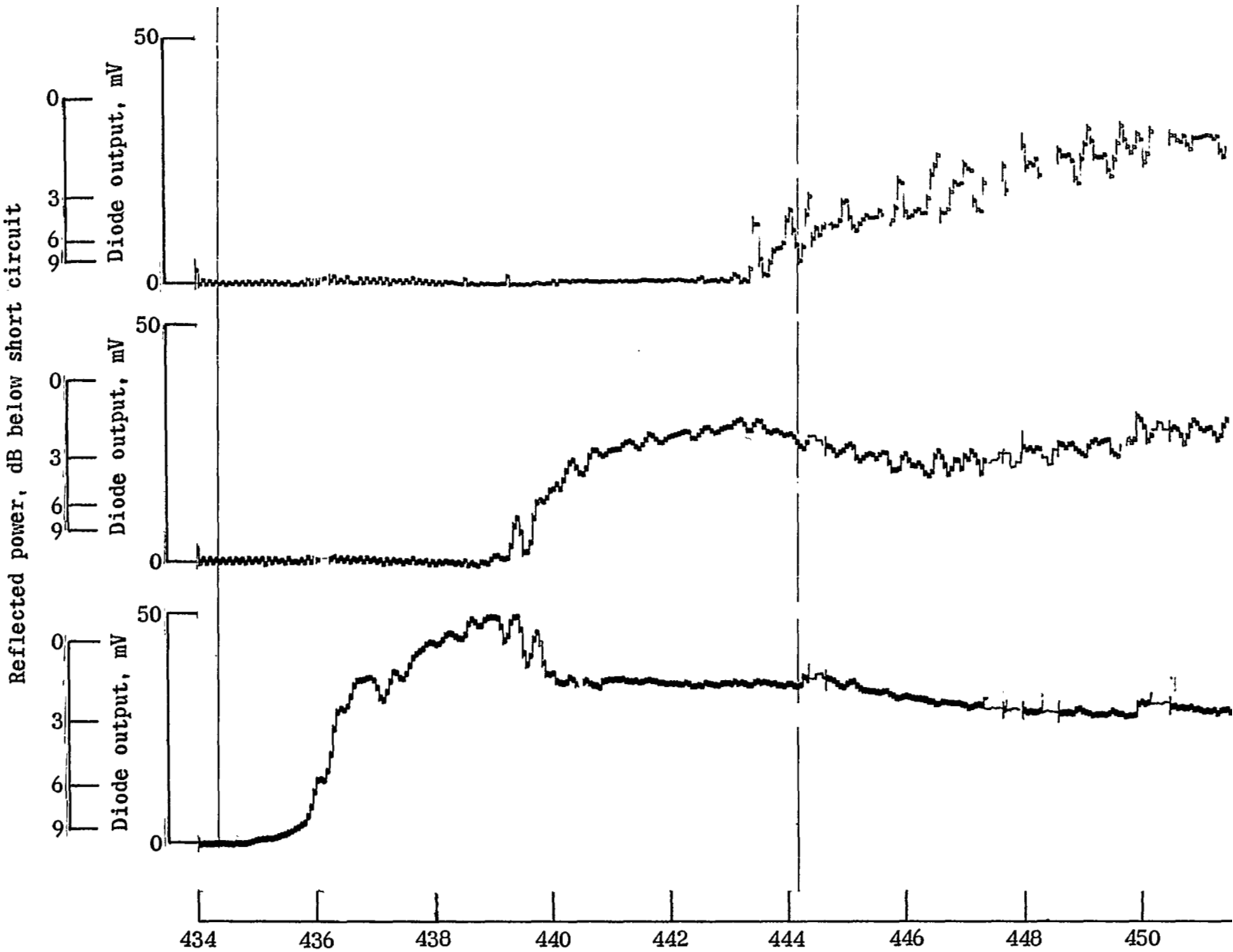

(b) Stati

Figure

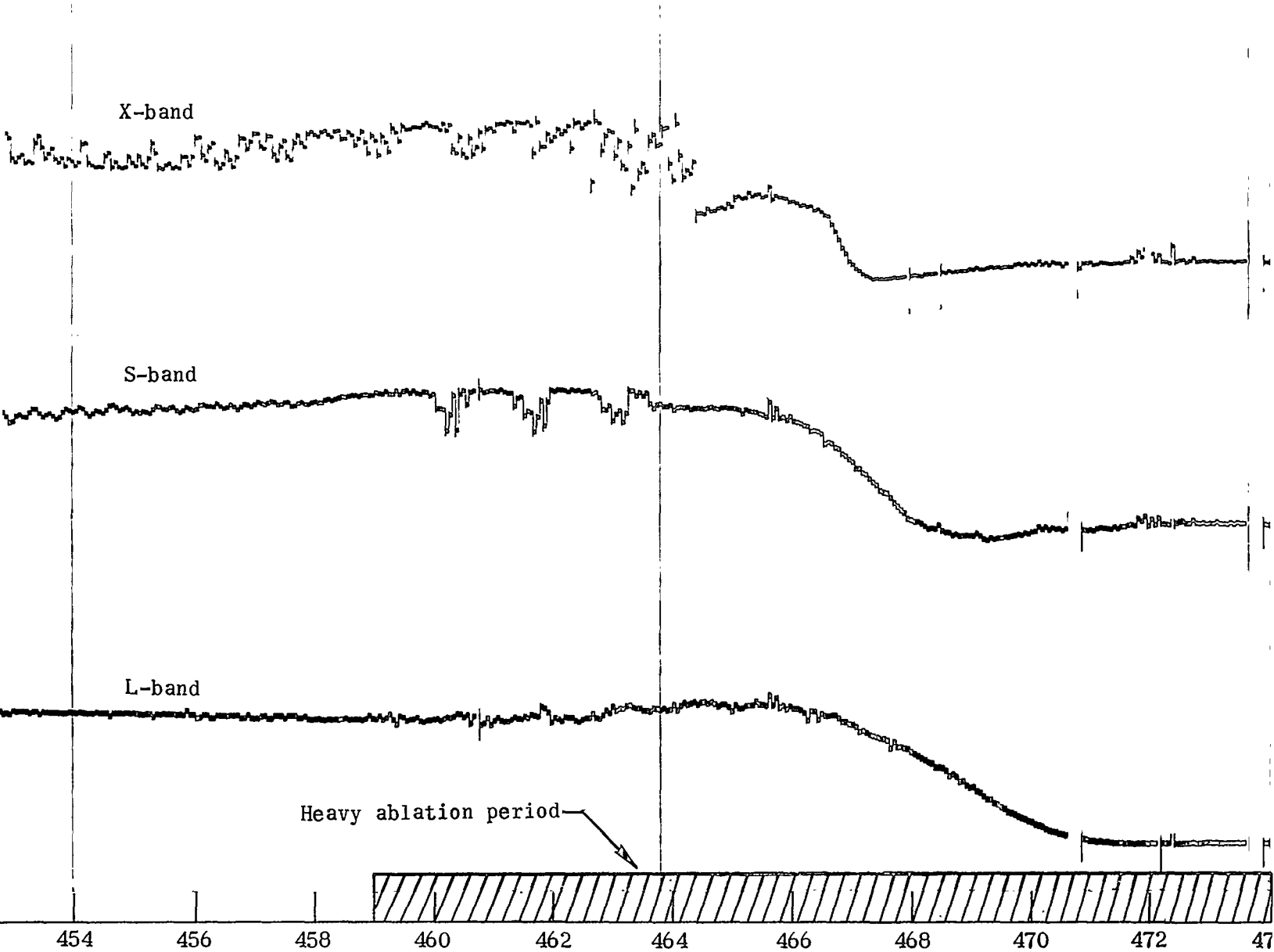

me from lift-off, sec

x/D = 0.76).

Continued.

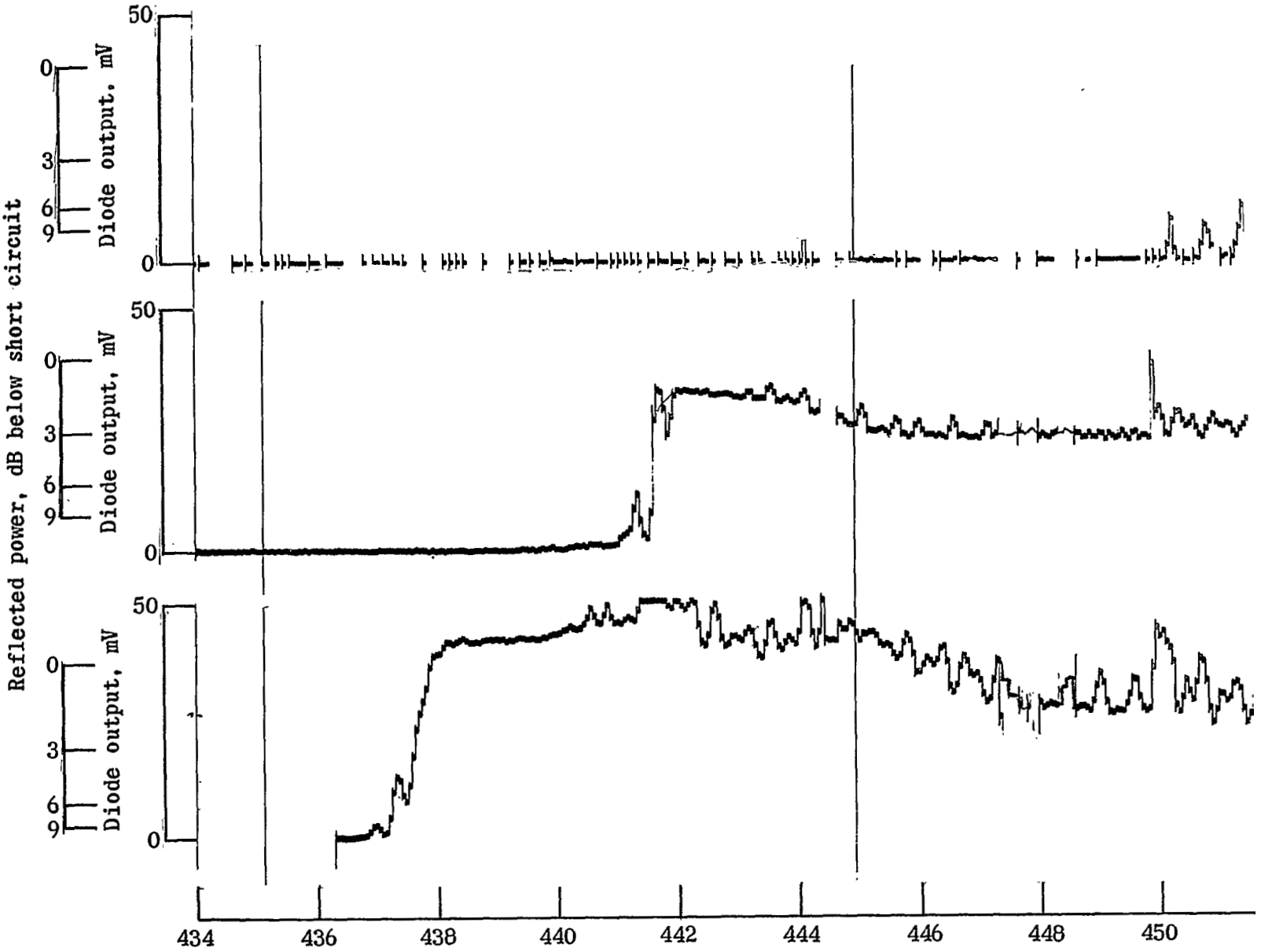

(c) Stati

Figure

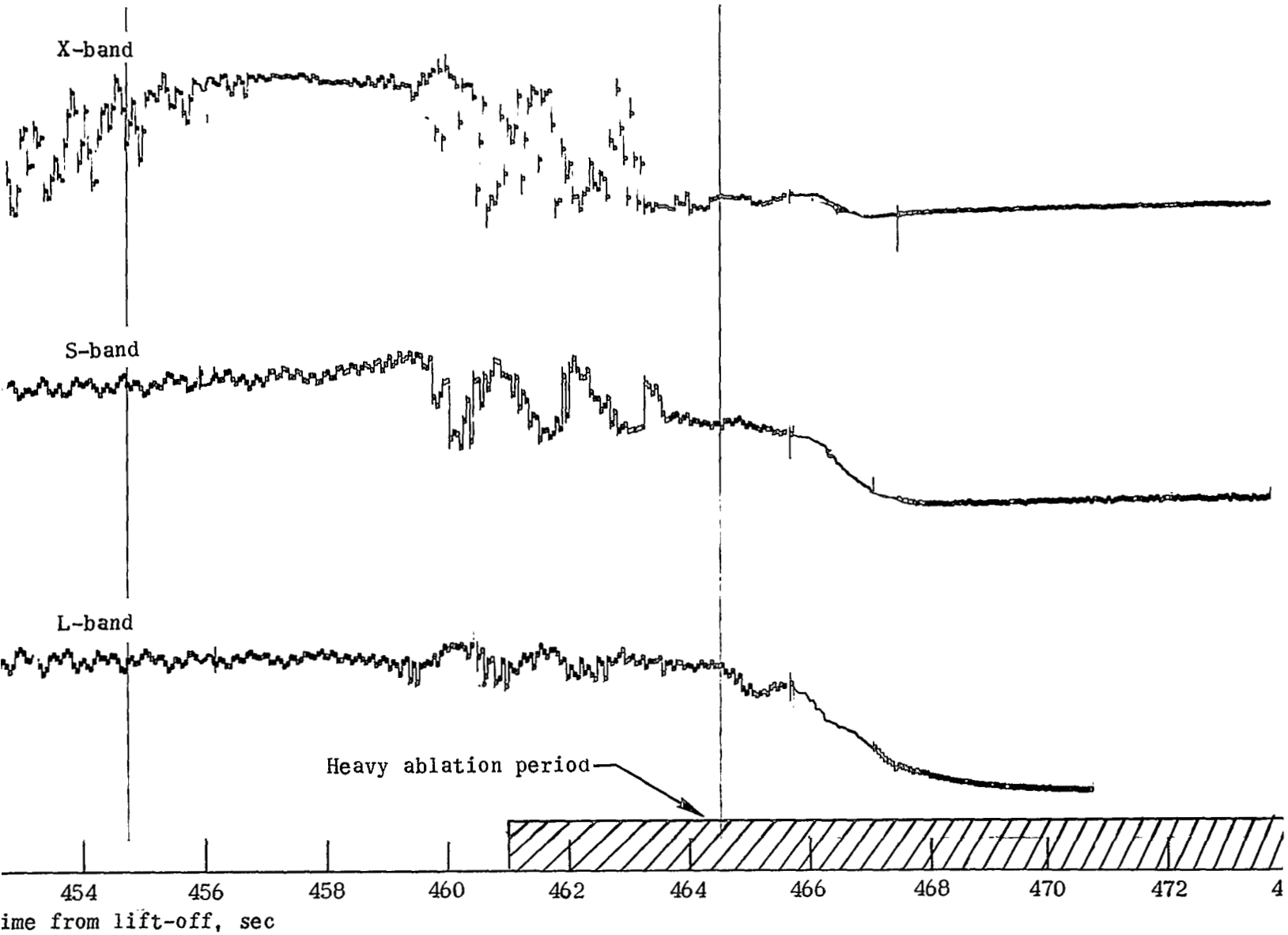

(x/D = 2.30).

Continued.

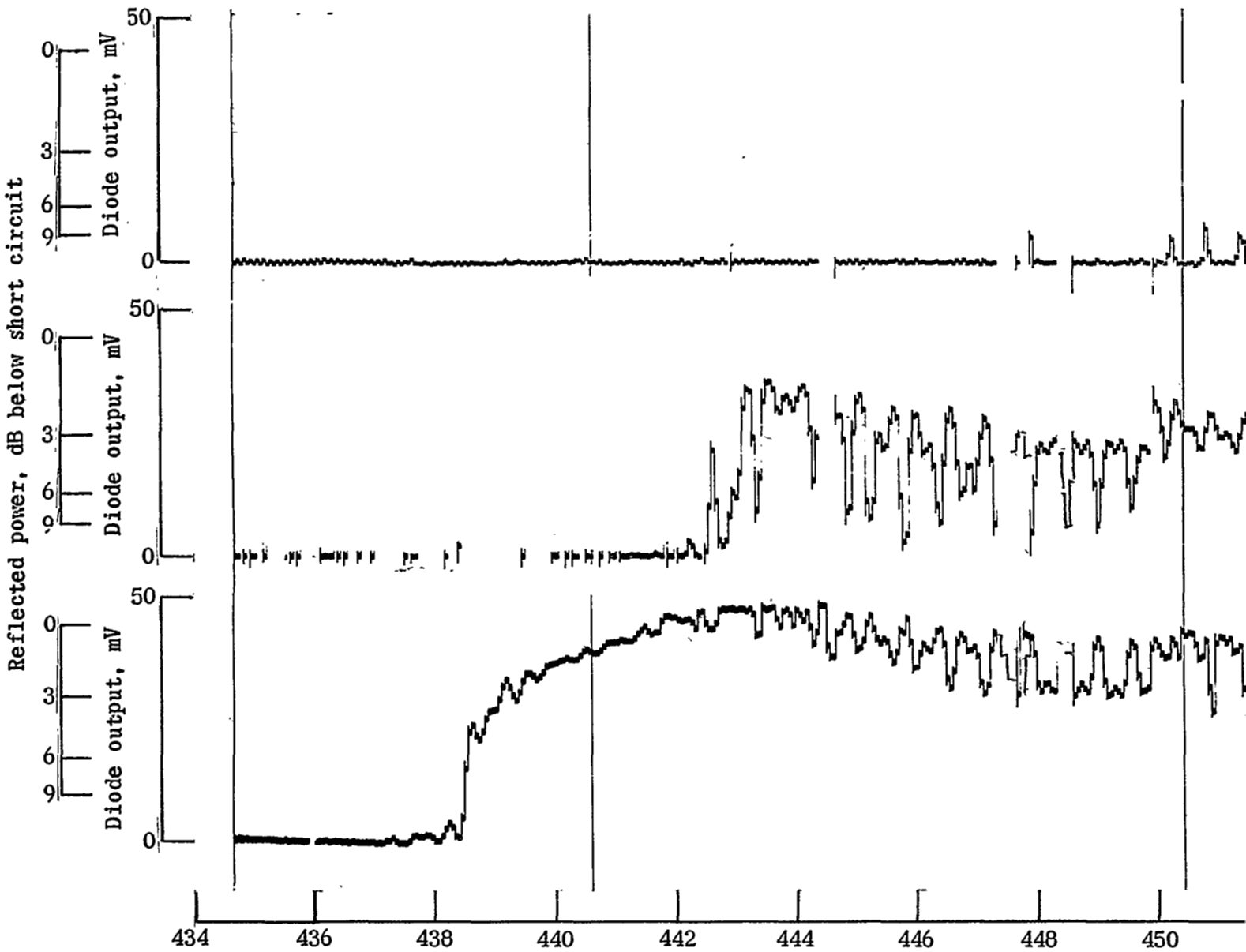
Reflected power, dB below short circuit
0
3
6
9
Diode output, mV
50
0
434
436
438
440
442
444
446
448
450
Del

(d) Sta

Figur

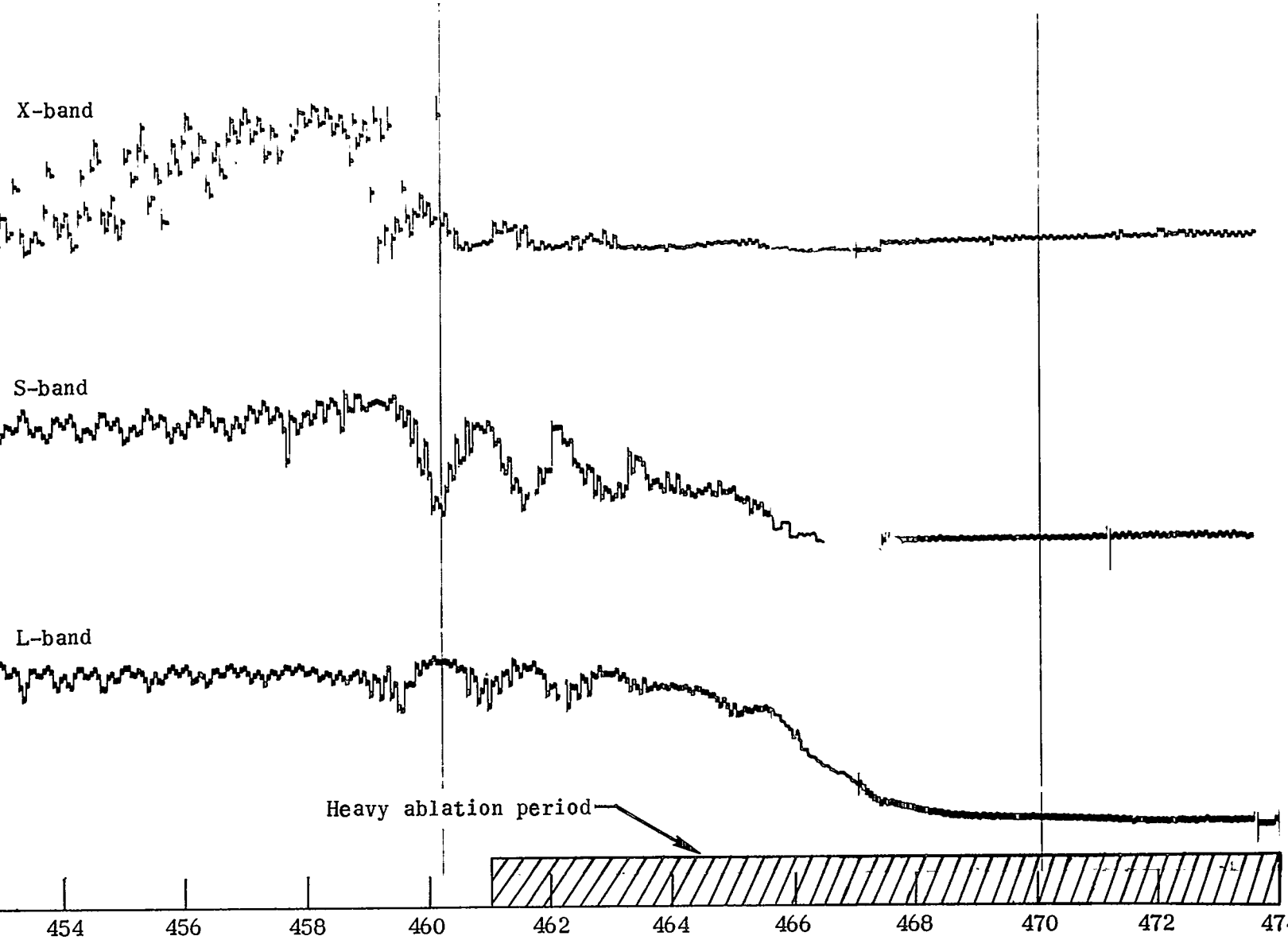

me from lift-off, sec

x/D = 3.48).

Concluded.

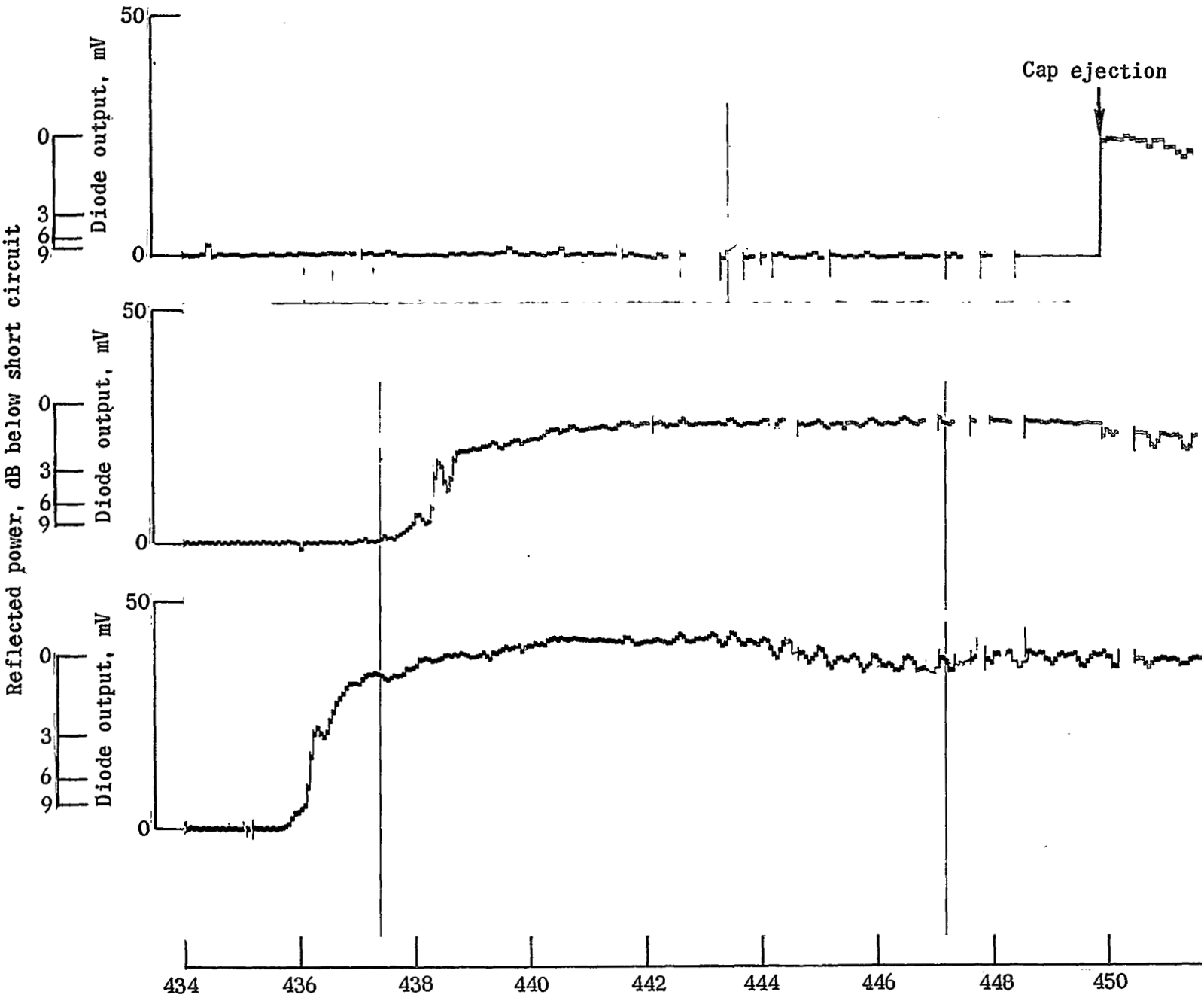

(a) Static

Figure 29.- Reflectometer levels from reflected power detec

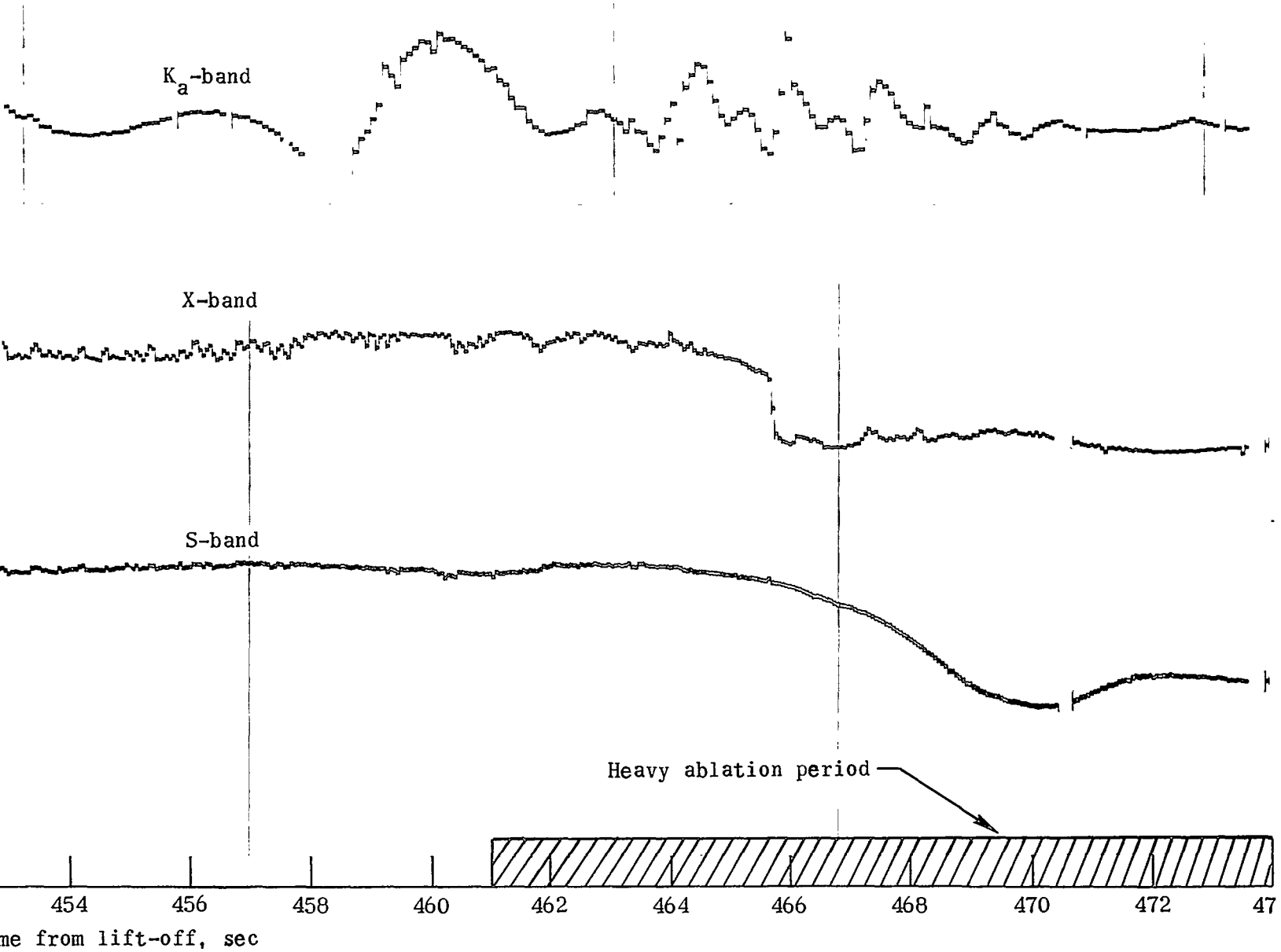

x/D = 0.15).

All data are from the 45 × 20 commutator except K_a-band data.